Progress in Quantum Electronics 38 (2014) 237–313

Progress in Quantum Electronics

www.elsevier.com/locate/pquantelec

Review

# Self-assembled InAs/InP quantum dots and quantum dashes: Material structures and devices

Mohammed Zahed Mustafa Khan, Tien Khee Ng, Boon S. Ooi*

*Photonics Laboratory, Computer, Electrical, and Mathematical Sciences and Engineering (CEMSE) Division, King Abdullah University of Science and Technology (KAUST), Thuwal 23955-6900, Saudi Arabia*

Available online 20 November 2014

**Abstract**

The advances in lasers, electronic and photonic integrated circuits (EPIC), optical interconnects as well as the modulation techniques allow the present day society to embrace the convenience of broadband, high speed internet and mobile network connectivity. However, the steep increase in energy demand and bandwidth requirement calls for further innovation in ultra-compact EPIC technologies. In the optical domain, advancement in the laser technologies beyond the current quantum well (Qwell) based laser technologies are already taking place and presenting very promising results. Homogeneously grown quantum dot (Qdot) lasers and optical amplifiers, can serve in the future energy saving information and communication technologies (ICT) as the work-horse for transmitting and amplifying information through optical fiber. The encouraging results in the zero-dimensional (0D) structures emitting at 980 nm, in the form of vertical cavity surface emitting laser (VCSEL), are already operational at low threshold current density and capable of 40 Gbps error-free transmission at 108 fJ/bit. Subsequent achievements for lasers and amplifiers operating in the O-, C-, L-, U-bands, and beyond will eventually lay the foundation for green ICT. On the hand, the inhomogeneously grown quasi 0D quantum dash (Qdash) lasers are brilliant solutions for potential broadband connectivity in server farms or access network. A single broadband Qdash laser operating in the stimulated emission mode can replace tens of discrete narrow-band lasers in dense wavelength division multiplexing (DWDM) transmission thereby further saving energy, cost and footprint. We herein reviewed the1 progress of both Qdots and Qdash devices, based on the InAs/InGaAlAs/InP and InAs/InGaAsP/InP material systems, from the angles of growth and device performance. In particular, we discussed the progress in lasers, semiconductor optical amplifiers (SOA), mode locked lasers, and superluminescent diodes, which are the building blocks of EPIC and ICT. Alternatively, these optical sources are potential candidates for other multi-disciplinary field applications.


*Keywords:* Quantum dots; Quantum dash; Laser diode; Superluminescent diode; Mode locked laser; Broad gain

*Corresponding author.
*E-mail address:* boon.ooi@kaust.edu.sa (B.S. Ooi).

http://dx.doi.org/10.1016/j.pquantelec.2014.11.001
0079-6727/

## Contents

## 1. Introduction

Demand for high performance active optical elements in the form of semiconductor lasers, light-emitting diodes, mode-locked lasers, and semiconductor optical amplifiers (SOA), modulators, etc. are significantly rising because of the current demand for large bandwidths in the 1.55 μm C-band optical communication window to meet the requirements for the exponentially growing internet and mobile connectivity market or ICTs. The intervention of optical fiber technology and related active optical elements in the short-reach communications, such as intra-rack and inter/intra-chip optical interconnects, due to the struggling electrical interconnects to satisfy the requirements of bandwidth, packing density, cost, and power consumption, demand further investigations into achieving high quality semiconductor material and devices. The realization of ultra-compact and high performance optical components such as semiconductor lasers, mode locked lasers, SOA, detectors, etc. will play a pivotal role towards the advancement of EPIC technologies and ICT.

Quantum confined nanostructure based active-regions in the form of Qwells and self-assembled Qdots have played a pivotal role in the achievement of efficient semiconductor devices, thanks to the high quality epitaxial material growth on GaAs substrate emitting at ~1.3 μm. Exceptional performances from these semiconductor devices based on InAs/GaAs dots has already been achieved and commercialized [1,2]. However, the inability of the GaAs based material system to reach the long haul optical communication window of 1.55 μm and beyond resulting in the dominance of Qwell based devices grown on InP substrates to take the center stage. Already in the market and serving the optical fiber technology 1.55 μm Qwell devices has shown substantial improvement in device characteristics compared to the double heterostructure counterparts. Recently, much attention has been directed to achieve InAs Qdots at long-wavelengths on InP substrate with the aim of further improving the 1.55 μm device performances. However the small lattice mismatch and the resulting complex strain distribution resulted in the formation of a new class of self-assembled Qdash nanostructures instead of Qdots. These are elongated dot-like nanostructures emitting between ~1.5 and ~2.0 μm wavelength range and possess interesting mixed characteristics in between Qwell and Qdots [3]. Epitaxial growth of InAs Qdots which require alteration to the growth kinetics in order to avoid Qdash formation has been addressed by various research groups in recent years by employing conventional and miscut (100) InP, and (311) InP substrates, along with various innovations in growth. InAs Qdots and Qdashes on both InGaAsP and InGaAlAs material systems have been developed with respectable device performances. However, the significant reduction of size and shape dispersion (large inhomogeneous broadening) of these nanostructures due to self-assemble growth procedure still pose a challenge in achieving high quality epitaxial material and hence device performance. Currently, the size dispersion, characterized in terms of photoluminescence (PL) linewidth (full-width-at-half-maximum, FWHM), are ~20 meV at 10 K for Qdots [4] and ~50 meV at room temperature for Qdashes [5–7]. These values indicate further improvement in material quality to be competitive with the matured InAs/GaAs Qdots on GaAs substrate technology [1,2].

Alternately, by exploiting the inherent inhomogeneous nature and ultra-broad gain profile of InAs/InP Qdots and Qdashes, highly attractive broadband optical components could be achieved. This would enable broadband SOAs, electro-absorption modulator, photo detector to be implemented as an integral part of the DWDM technologies. An ultrabroad gain profile of $>300$ nm from Qdash active elements, as well as lasing and amplified spontaneous emission (ASE) bandwidths crossing more than 50 nm and 700 nm, respectively, from lasers and superluminescent diodes (SLD) are two examples of the recent significant developments in this field of study [5,8,9]. Besides, broadband nature of the InAs/InP Qdot and Qdash laser diodes has been exploited to generate ultra-short femto-second pulses of 158 fs at 2.21 THz from passive mode-locked laser scheme [10,11] which could find important applications in high speed optical time-domain multiplexer (OTDM), wavelength division multiplexed (WDM) communications, and optical clocking to replace electronic clocking in high-speed electronic circuits, such as a microprocessor.

Furthermore, the wavelength tuning capability of InAs/InP Qdot and Qdash devices reaching 2 μm and beyond in tandem with their broad gain profile has a potential impact on various multi-disciplinary fields. For instance, in medical diagnostics, a broadband semiconductor optical source would enable a compact, high axial resolution, low cost, optical coherent tomography (OCT) system for tissue and bio-molecule imaging, particularly in dentistry and bone-related disease diagnostics [12–15]. In addition, a compact 2 μm laser source would be a promising candidate for highly precise surgical application for both soft and hard tissues such as precise tissue ablation, ophthalmic surgery and dentistry, neurosurgery, spinal surgery, etc. where currently solid state lasers dominate [16]. In spectroscopy methods such as absorption, transmission, luminescent, etc., for material and molecular characterizations, a compact long wavelength broadband light source can be employed. These optical sources also has the potential to offer compact hand-held chemical sensor capable of in-situ multicomponent analysis (simultaneous sensing of $CH_4$, CO, $CO_2$, $H_2S$, HCl, $NH_3$, $C_2H_4$, $C_2H_2$, $C_2H_6$, $C_6H_6$, etc.) as well as integrated real-time near-infrared Lidar (LIght Detection And Ranging) system for monitoring environmental health, and managing emission of greenhouse gases and hazardous chemicals. Many high precision optical metrology systems require light sources emitting broad spectrum of wavelength in the near infrared regime. These include optical time-domain reflectometry (OTDR) for optical fiber fault measurements, and DWDM component characterizations, optical instrumentation, etc., and fiber gyroscopes. Deployment of ultra-broadband optical sources in OTDR would greatly improve the system sensitivity and resolution. In material processing, a compact, high power, near infrared wavelength ($\sim 2$ μm) lasers would allow direct processing of plastics which are transparent in the visible wavelength range via laser cutting, welding, and marking [16]. Besides, long wavelength optical source based OCT systems are finding niche applications in the field of dimensional metrology, material research, non-destructive testing (NDT), for imaging ceramics, studying on the penetration depths in various polymer materials as well as on birefringence imaging of different crystalline polymer structures, are already gaining popularity [17], and could further benefit by achieving larger penetration depth offered by ultra-broadband optical sources.

In a nutshell, the chronological progress of the performance of InAs/InP Qdot and Qdash lasers and mode-locked lasers are plotted in Figs. 1 and 2, respectively. In particular, we show the achievements of edge-emitting semiconductor lasers in these figures and omitted VCSELs in our review; henceforth, we discuss only the edge-emitting lasers. The significant improvement of

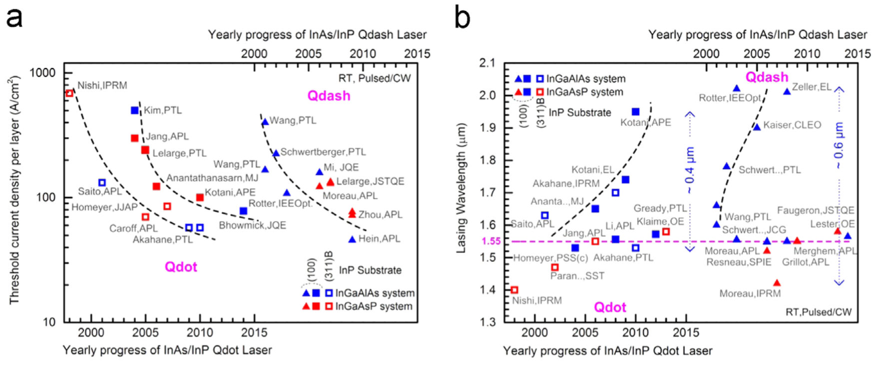


Fig. 1. Chronological progress in the (a) reduction of the threshold current density per layer, and (b) room temperature lasing wavelength tunablity of InAs/InP Qdot (squares) and Qdash (triangles) semiconductor lasers. The dash lines are guide to the eyes showing improvement trend. The data points are collected from the references.

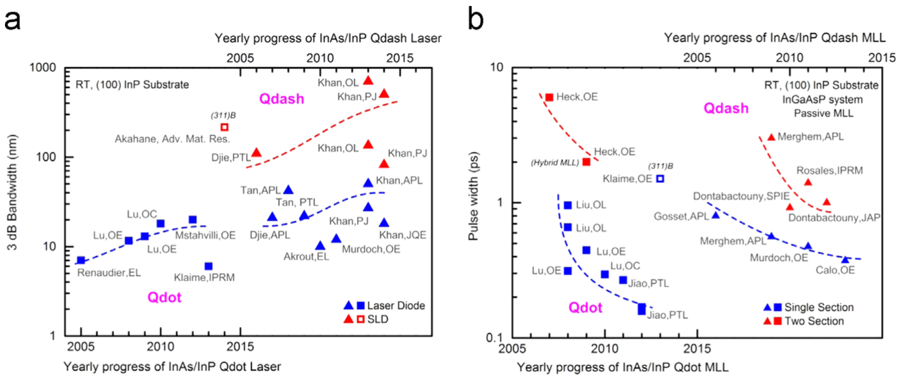


Fig. 2. Chronological progress in (a) achieving ultrabroad emission bandwidth, and (b) reduction in pulse width of InAs/InP Qdot (squares) and Qdash (triangles) lasers and mode-locked lasers, respectively, at room temperature. The dash lines are guide to the eyes showing improvement trend. The data points are collected from the references.

the threshold current density per Qdots/Qdashes layer of InAs/InP lasers, as illustrated in Fig. 1(a), is indicative of a key step towards highly efficient semiconductor lasers. Although the best values of ~57 A/cm$^2$ (Qdots) and ~45 A/cm$^2$ (Qdashes) per layer are far inferior to the InAs/GaAs Qdots material system (17 A/cm$^2$), the recent solutions to address the complex growth kinetics of dots/dash on InP substrate are expected to rapidly reduce the threshold current density. The tuning capability of the ground state (GS) lasing wavelength of InAs/InP Qdot and Qdash lasers at room temperature is depicted in Fig. 1(b), with a tuning range of ~0.4 μm and ~0.6 μm, respectively, covering the entire C–L–U optical communication bands, and room temperature lasing beyond 2 μm wavelength. On the other hand, tapping on the broad gain profile of inhomogeneous InAs/InP Qdots and Qdashes active region, broadband laser diodes and SLDs have been demonstrated, and summarized in chronological order in Fig. 2(a). The output power in the range of few hundreds of mW from laser diodes and tens of mW from SLDs has been reported. The broadband nature of lasers was the key feature to generate ultra-short femto-second pulses based on the passive mode-locked scheme with reported values progressively reaching few hundred fs range with time, as illustrated in Fig. 2(b). A pulse repetition rate as high as 356 GHz and even reaching terahertz (via external means), and pulse width as low as 158 fs has been achieved on InAs/InP Qdot/Qdash material platform, thus showing the potential of this platform for future optical communications and cross-disciplinary applications.

In this review, we examine the existing self-assembled growth of InAs Qdot and Qdash based nanostructures on InP platform for eventual operation in the C–L–U band and towards 2 μm. The tremendous progress and achievement in this area resulted in an astounding amount of literature. This review took the liberty to divide the work based on Qdots (Sections 2, and 3), and Qdashes (Sections 4, and 5) on InP substrate. While Sections 2 and 4 focus on the achievements in the epitaxial material growth, Sections 3 and 5 summarize the respective device implementation and system level performances, mostly concentrating on the edge-emitting lasers, SOA, mode locked lasers and SLDs. The InAs/InGaAlAs and InAs/InGaAsP based active elements discussed in this review are based on (100) and (311)B InP substrates, though it is noted that for III-V-silicon integration for integrated optical telecommunication chip had seen efforts in the growth of Qdots on other unique platforms such as Ge and SiGe/Si based substrates [18,19], as well as other Qdots based on ternary, and Qwell based quintenary material system, i.e. InAsSb and InGaAsNSb, respectively [20].

## 2. InAs Qdots grown on InP

The Stranski-Krastanov (SK) [21] growth of InAs Qdots on InP substrate has been a subject of intensive research. One of the main technology hurdles for growing high quality InAs Qdots has been the inclination of elongated wire-like nanostructures formation along the [0–11] crystal directions known as Qdashes. The formation of Qdashes on InP substrate has been attributed to the small lattice mismatch of 3.2% between InAs and InP and the possible complex growth kinetics, growth conditions, buffer layer surface morphology and composition [22,23]. In addition, another major problem in the growth of InAs Qdots on InP substrate is the relatively large Qdots inhomogeneity compared to the InAs/GaAs Qdots system. In the existing literature, various epitaxy growth techniques have been explored by various groups in three key growing systems *viz.* molecular beam epitaxy (MBE), metal-organic chemical vapor deposition (MOCVD), and chemical beam epitaxy (CBE). Here we reviewed the achievements in the material growth process of InAs Qdots on InP for two dominant material systems: (i) InAs/InGaAlAs and (ii) InAs/InGaAsP structures.

### 2.1. InAs/InGaAlAs Material System

The InAs/InGaAlAs system is usually preferred due to its large band offset between the InAs dots and the InGaAlAs barrier and elimination of As/P source exchange during the growth process. It also gives liberty in design of the barriers avoiding complicated quaternary InGaAsP alloys by simply adjusting the relative ratio of Ga and Al keeping a constant In flux and avoiding the switching of group V elements during growth [24]. However, MBE growth of InAs on InGaAlAs buffer layer utilizing (100) InP substrate resulted in elongated nanostructures along the [0–11] direction as shown in Fig. 3(a) which has been attributed to the significant influence of the effects of phase separation caused by the different growth behavior of In, Al, and Ga atoms [5,25,26]. On the other hand, growth of InAs on high Miller index (311)B InP substrate resulted in high density round shaped Qdots. This was reported by Saito et al. [27] and is shown in Fig. 3(b). The Qdots and Qdashes aerial density are $9\times10^{10}\,cm^{-2}$ and $2\times10^{10}\,cm^{-2}$,

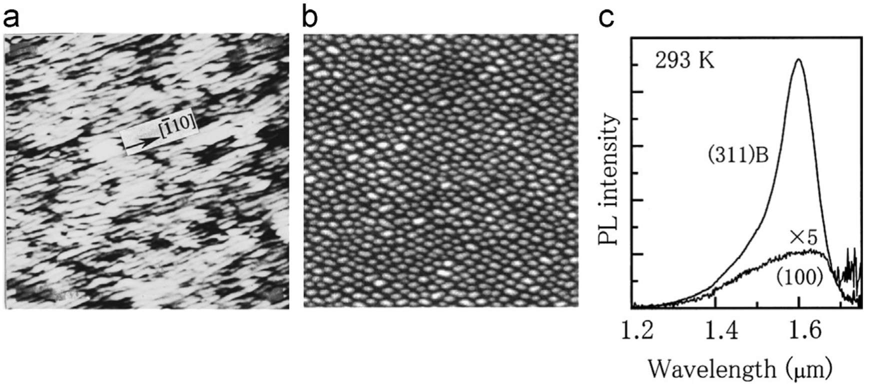


Fig. 3. Atomic force microscopy (AFM) images of InAs Qdots on InGaAlAs buffer on (a) (100) InP and (b) (311)B InP substrate. (b) Room temperature photoluminescence from InAs Qdots on (100) InP and (311)B substrates. Taken from [27,28].

respectively which is advantageous in achieving large optical gain. It was postulated that Al content in the buffer layer caused the formation of smaller size and higher density InAs Qdots. Moreover, the PL intensity from the single stack InAs Qdot, shown in Fig. 3(c), after capping with InGaAlAs, showed stronger emission from homogeneous Qdots with narrow PL linewidth of 51 meV centered around 1.55 μm. On the other hand, a broad PL emission and comparatively low intensity was observed from the highly inhomogeneous Qdash nanostructures. This is undesirable as it degrades the laser performance. However, our group exploited this feature of Qdashes in realization of novel devices which is discussed in Section 5. In the following, we reviewed the systematic progress in the growth of high quality, large density InAs Qdots on different InP substrate orientations.

#### *2.1.1. Qdots on (311)B InP substrate*

The formation of InAs Qdots on (311)B InP substrate was initially reported by Nötzel et al. [29] using MOCVD growth technique. Utilizing a thin (3–5 nm) strained InGaAs layer on 100 nm thick AlInAs buffer layer, a 0D microstructure was observed. This growth on high Miller index semiconductor surfaces opened the door for growing InAs Qdots on InP substrate for long wavelength near infra-red device applications.

Following this work, Alghoraibi et al. [30] investigated the formation of Qdots on the high-index (311)B InP substrate *via* MBE growth technique. A decrease (increase) in the Qdot diameter (density) is observed for Al-rich surface lattice matched buffer layers ($Al_{0.48}In_{0.52}As$, $Al_{0.29}Ga_{0.19}In_{0.52}As$, and $In_{0.53}Ga_{0.47}As$). Moreover, a continuous increase in Qdot density with the amount of InAs deposition is reported on AlInAs buffer layer, reaching a value as high as $1.3 \times 10^{11}$ cm$^{-2}$ with small Qdots (∼20 nm), as shown in the AFM image of Fig. 4(a). The evolution of Qdot density and size, illustrated in Fig. 4(b), was attributed to the interacting stress fields induced by the Qdot within the substrate. On the other hand, a drastic Qdot size reduction (2.2 nm mean height) and sharp density increase ($1.2 \times 10^{11}$ cm$^{-2}$) were observed when the As flux [measured in terms of beam equivalent pressure, (BEP)] was reduced during the Qdots formation (Fig. 4(c)). These results were similar to that reported by Caroff et al. using InAs/InGaAsP material system [31], and discussed in Section 2.2.2. The authors postulated that the increase in the InAs (311) B surface energy at low As pressure, which favored Qdots nucleation, has led to high density of small dots.

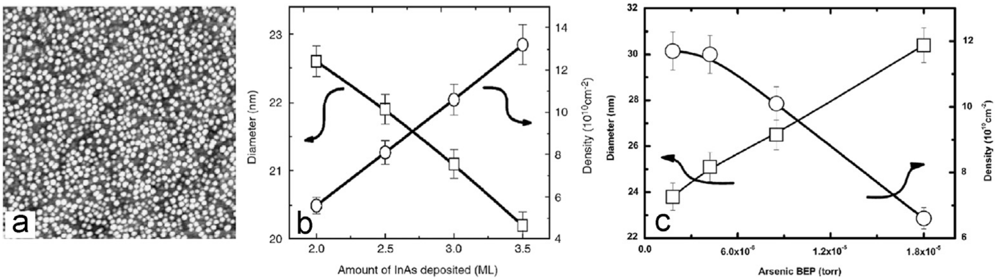


Fig. 4. (a) AFM images ($1 \times 1\ \mu m^2$) of InAs Qdots grown on AlInAs alloy lattice matched to InP, after InAs deposition at 3.5 ML nominal thickness. (b) Qdots diameter and density versus amount of InAs deposited and (c) arsenic beam equivalent pressure (BEP) during the Qdots formation. Adapted from [30].

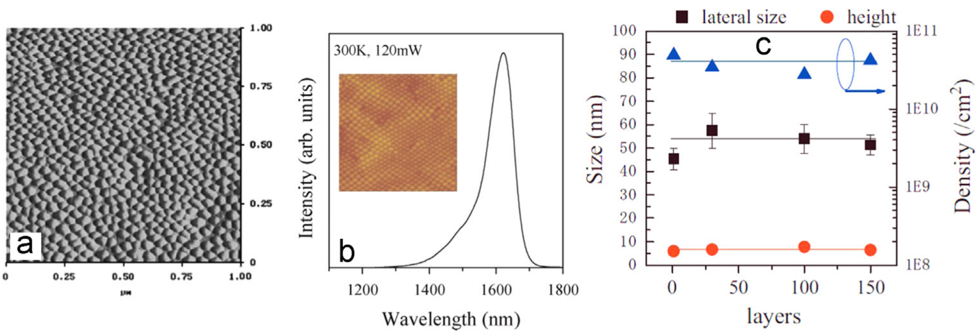


Fig. 5. (a) AFM images ($1 \times 1\ \mu m^2$) of a single layer InAs Qdots grown on 10 nm thick $In_{0.47}Ga_{0.11}Al_{0.42}As$ spacer layer on (311)B InP substrate. (b) PL spectrum of a 300 layer stack of InAs Qdots measured at room temperature. (c) Stacking layer dependence of size and density of Qdots. The inset in (b) is a $1 \times 1\ \mu m^2$ AFM image of the 300th layer of InAs Qdots stack. Courtesy of [32,34].

Stacking of Qdot layers for increasing the material gain is a standard process employed in quantum-confined nanostructure based active region device designs. However, the tensile strain generated by the InAs Qdots is not compensated as the capping layer is normally lattice matched to the substrate material. This issue has been successfully addressed by Akahane et al. using MBE growth technique who proposed and demonstrated a strain-compensation scheme [32]. The approach was based on adjusting the composition of the InGaAlAs spacer layers to have a smaller lattice constant than that of the InP substrate in order to achieve strain compensation after the growth of one cycle of Qdots and the spacer layer. Fig. 5(a) shows the AFM image of a single layer of InAs Qdots on (311)B InP substrate with an average diameter, fluctuation, and density of 51.2 nm, 13.4% and $7.84 \times 10^{10}\ cm^{-2}$, respectively. The corresponding figures of merits for an equivalent 20 stack Qdots are 54 nm, 10.1% and $7.36\ cm^{-2}$, respectively. These impressive results have been attributed to the quaternary spacer layer which allowed continuous change of its lattice constant by controlling the composition, and the Al in the spacer layer which played the key role by preventing the segregation of In in InGaAlAs [33]. In a recent demonstration, successful growth of 300 stack Qdots (shown in Fig. 5(b) and (c)) with room temperature PL emission at $\sim 1.55\ \mu m$, GS linewidth of 30 meV, and a total Qdot density of $> 1.9 \times 10^{13}\ cm^{-2}$ showed the effectiveness of this technique [34]. Later, laser device with a 30-stack InAs/InP Qdots active region is also demonstrated [35] and has been discussed in Section 3.1.1.

Nevertheless, epitaxial growth of InAs Qdots on the (311)B InP substrate suffers from device processing problems like mirror cleaving, anisotropic etching, etc. Therefore, growth of Qdots on conventional (100) InP substrate is required and has been addressed by various research group concurrently which is reviewed below.

### 2.1.2. Qdots on (100) InP substrate

MBE growth of InAs Qdashes instead of Qdots on InGaAlAs buffer layers has been explored to elucidate their growth kinetics and provide key insights for eventual realization of InAs Qdots on (100) InP substrate. For instance, the role of buffer layer surface morphology and alloy contents was examined in Ref. [22] as they affect the formation of the nanostructures; growth of high density InAs nanostructures resembling like elongated Qdots [36]; sparsely populated InAs nano-islands [37] on InGaAs, InAlAs, and InP buffer layers on (100) InP [23]. In this respect, Stinz et al. [38] suggested the utilization of vicinal (100) InP substrates for the growth of InAs Qdots. From the MBE growth of InAs Qdots on lattice matched InGaAlAs barriers and utilizing vicinal (100) InP substrate, it was found that the Qdot formation is favored when the step edges run perpendicular to the direction of Qdashes *i.e.* tilted towards (111)B direction while the other direction (111)A showed no change when compared to the exact (100) direction. They postulated that this shape transition to Qdots occurred because of the local strain field occurring at the steps. The PL emission on capped structures at room temperature was in the wavelength range from 1.5–2.1 μm. Similar observation of Qdot formation on (311)B InP substrate by MBE was reported in Ref. [30]. The room temperature PL emission up to 2.1 μm and PL linewidth ~70 meV was reported. Furthermore, growth of InAs Qdots was also noticed under MOCVD growth on lattice matched InGaAlAs buffer layer on 2° misoriented (100) InP substrate towards the nearest ⟨011⟩ direction [39]. It was found that when increasing the Al content in the buffer layer, on top of which Qdots were grown, the PL emission wavelength was blue shifted in conjunction with the growth of smaller Qdot size and higher Qdot density.

Instead of using vicinal InP substrate, Li et al. [40] proposed and assisted growth technique for the MBE growth of InAs Qdots on exact (100) InP. Through the introduction of a lattice-matched thin (~5 nm) InGaAlAs underlying layer on AlInAs buffer layer, a high quality InAs Qdots with high uniformity has been demonstrated by exploiting the strong dependence of the nanostructure morphology on the characteristics of the underlying alloy. For InAs deposited directly on InAlAs buffer layer, Qdashes elongated along [−110] are formed with an average ~25 nm width and $3.5\times10^9\ cm^{-2}$ density while employing the assisted growth technique, round Qdots with ~45 nm in size and $2.5\times10^9\ cm^{-2}$ in density were observed.

In another study, Kim et al. utilized thin underlying GaAs [36] and InGaAs [41] layer as a means to control the optical and structural properties of InAs Qdots grown on latticed matched InGaAlAs matrix on (100) InP substrate. Increasing the GaAs layer thickness from 0.8 nm to 1.6 nm blue shifted the PL emission wavelength and resulted in reduced PL intensity. This was attributed to the decrease in the Qdot size and high GaAs potential barrier, and reduction in Qdots density, respectively. In addition, uniform Qdots size was obtained with GaAs underlying layer compared to the Qdots directly grown on InGaAlAs matrix, as reflected by the PL linewidth of 70 meV in the former case and 80 meV in the latter case. Using the $In_{0.32}Ga_{0.68}As$ underlying layer, a similar uniform Qdots were observed with an average lateral size and height of 42 nm and 3 nm, respectively, and PL linewidth 64 meV centered at ~1.55 μm. The improvement in Qdots size uniformity was ascribed to the different growth front, growth behavior of group III elements at the interface between Qdots and barrier, and the modulation in the strain field. Surprisingly, growth of nanostructures directly on AlInAs lattice matched matrix layer without any underlying layer showed

Qdots formation with slight elongation along [1–10] direction, as seen in Fig. 6(a), consistent with the results reported by Brault et al. [23], while the elongation significantly reduced on InAlGaAs matrix layer (see Fig. 6(b)). However, this observation is in contrast to the work reported by Li et al. [40] who reported dash formation on AlInAs buffer layer with similar amount of InAs deposition (~5 ML). Thus, this disparity cannot be attributed to the different amounts of InAs deposition as reported by Stintz et al. [38] who observed: (i) Qdash formation at low InAs coverage above the critical thickness, and (ii) transformation into Qdots on increasing InAs coverage. This shows that the resulting nanostructures are highly sensitive to the properties of the surface and the growth conditions. The InAs Qdots on $In_{0.32}Ga_{0.68}As$ were observed to be larger in size as depicted in Fig. 6(c).

Instead of changing the buffer layer alloy or composition for the growth of InAs Qdots on (100) InP substrate, Kim et al. [25] explored the alteration in the growth of InAs Qdots. They presented an alternate growth method, *i.e.* AGQD where 1 ML thick InAs layer and 1 ML thick InAlGaAs layer were alternately deposited. Single stack sample was grown by MBE on InGaAlAs buffer layer. The average lateral size and height of AGQDs were ~40 nm and ~10 nm, respectively, and aspect ratio (height/width) ~0.25; while the corresponding values of the conventionally grown reference InAs Qdots (CQD) were ~26 nm and ~2.5 nm, and aspect ratio ~0.1. They attributed the formation of Qdots to the initial accumulated strain arising from the large lattice mismatch between the InAs layer and the InAs/GaAs layer. In addition, they also ascribed to the strong influence of locally directional migration of In, Al, and Ga adatoms during the deposition of the thin InGaAlAs layer on the Qdots nucleation sites due to the surface

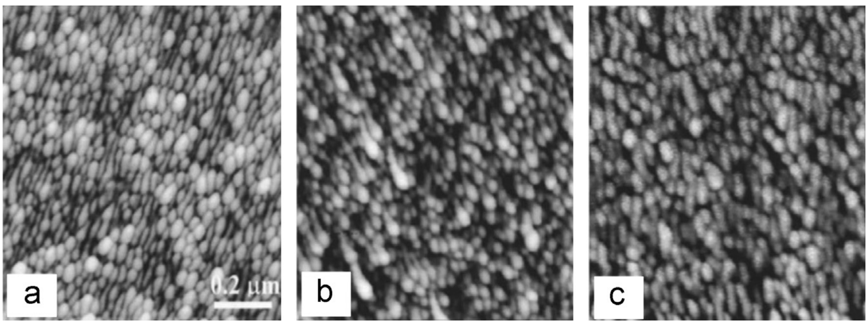


Fig. 6. AFM images ($1 \times 1\ \mu m^2$) of 5.6 ML InAs Qdots grown on: (a) AlInAs, (b) InAlGaAs, and (c) 11.5 nm thick $In_{0.32}Ga_{0.68}As$ on InAlGaAs. Taken from [41].

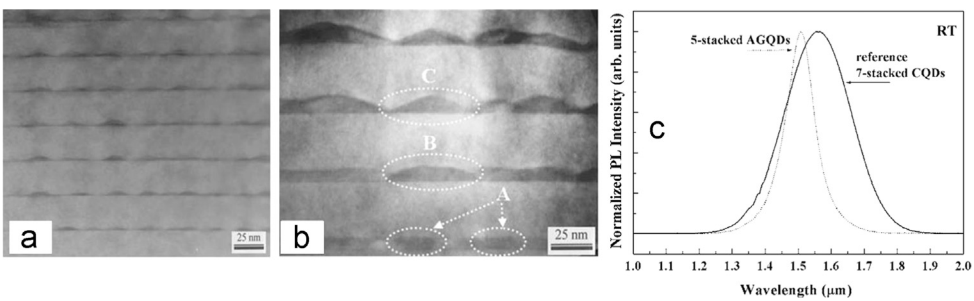


Fig. 7. TEM micrographs of: (a) seven stack CQDs and (b) five stack AGQDs. (c) Room temperature PL spectra of the two samples. Collected from [42].

chemical potential. The observation of well-defined GS at 1.485 μm and excited state (ES) at 1.4 μm were reported at room temperature in Ref. [25]. In addition, they also compared a multi-stack grown InAs Qdots based on AGQD (5-stack) and the CQD (7-stack). The corresponding aspect ratio obtained were ~0.22 and ~0.1 [42] and is shown in the transmission electron micrograph (TEM) of Fig. 7(a) and (b). The room temperature PL linewidth and emission wavelength from the CQD and AGQDs, as depicted in Fig. 7(c), were 85 meV at 1.55 μm, and 35 meV at 1.5 μm, respectively, with the latter one among one of the best inhomogeneous broadening value obtained at room temperature on InAs/InP Qdots. The optical stability [43] and the effects of group III elements on the growth kinetics of AGQDs were also investigated *via* utilization of 1 ML InAs and GaAs layers instead of InGaAlAs layer during the growth of InAs Qdots on (100) InP substrate [44].

Recently, in an attempt to realize InAs Qdots on (100) InP using MBE, Gilfert et al. [45] found that the arsenic species had a dramatic effect on the formation of nanostructures on InGaAlAs buffer layer. The $As_4$ supply during InAs deposition resulted in Qdash formation on InGaAlAs whereas $As_2$ supply produced round-shaped Qdots structures with density $2.0\times10^{10}$ cm$^{-2}$, as shown in Fig. 8(a)–(c). The transformation in nanostructure growth was attributed to different incorporation mechanisms of arsenic species. Eliminating the process of cracking $As_4$ into two $As_2$ molecules at the surface by direct supply of $As_2$ severely lowered the anisotropic migration of indium adatoms along the [0–11] direction due to the stable As-terminated atomic steps along this direction under $As_2$ flux. Under optimized growth conditions of 6 ML InAs deposition and 15 V/III ratio, an increased surface density of $4.0\times10^{10}$ cm$^{-2}$ and a PL linewidth of 23 meV at ~1.59 μm was reported, which is the record low PL linewidth value at 10 K. The results are illustrated in Fig. 8(d). Similar InAs Qdots formation using $As_2$ species on InAlAs buffer layer on (100) InP was also reported by Fafard et al. [46] more than a decade ago.

### 2.2. InAs/InGaAsP Material System

This material system has smaller lattice mismatch which resulted in relatively large Qdots besides suffering from issues related to As/P exchange during InAs growth on InP/InGaAsP buffer layer [47], which inevitably contributes to Qdots with emission wavelength beyond 1.6 μm. For instance, Yoon et al. [47] found that the areal density, size distribution, and shape of

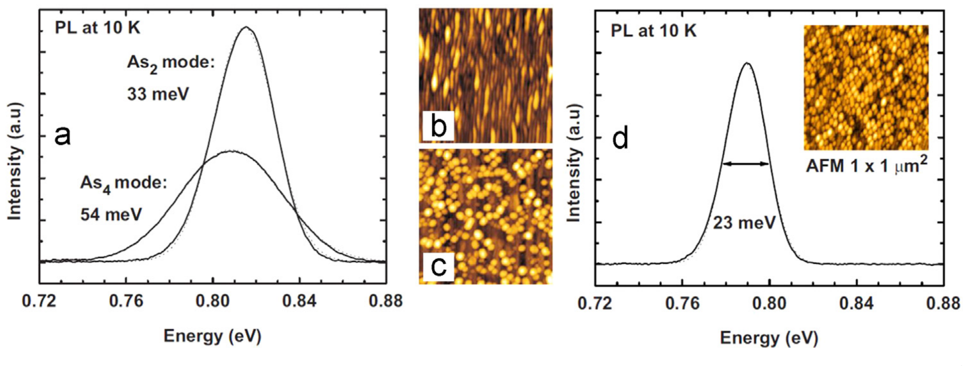


Fig. 8. (a) PL spectra measured at 10 K under non-optimized growth conditions and the AFM images ($1\times1$ μm$^2$) of samples grown using (b) $As_4$ and (c) $As_2$ fluxes. (d) PL spectrum at 10 K and AFM image (inset) of the optimized $As_2$ sample with 6 ML InAs and a V/III ratio of 15. In (a) and (d) the solid lines are experimental data and the dashed lines indicate the Gaussian fits. Taken from [45].

MOCVD grown InAs self-assembled Qdots changed significantly with temperature and V/III ratio with maximum reported density $4.5 \times 10^{10}$ cm$^{-2}$. Michon et al. showed that decreasing the trimethyl-indium (TMI) flow rate [48] *i.e.* InAs growth rate or InP capping layer growth rate [49] decreased the dot density while maintaining PL peak at 1.58 µm, reaching value as low as $9 \times 10^{7}$ cm$^{-2}$. These findings were ascribed to the As/P exchange reaction at the surface which played an important role in the growth kinetics of InAs Qdots on (100) InP substrates. In brief, the P atoms on the InP/InGaAsP surface buffer layer are easily exchanged by As atoms and deteriorate the interface quality when the surface is exposed to an As-bearing ambient. In the growth of InAs Qdots the strain field around the Qdots may make the As/P exchange reaction even more complicated, significantly altering the kinetic processes of Qdot formation which are functions of the MOCVD, CBE, and MBE growth conditions. In the following, we discussed the InAs Qdot growth on InGaAsP/InP material platform by separating the review into the two substrate orientations.

### 2.2.1. Qdots on (100) InP substrate

Using (100) InP vicinal substrates with 2° misorientation towards (110), Nötzel et al. [50] reported a comprehensive study of different MOCVD growth conditions to obtain InAs/InP Qdots. Increasing the Qdot growth temperature increased the dot size with diameter and height of more than ~100 nm, and ~15 nm, respectively, thus achieving PL emission beyond 1.6 µm; while at reduced growth temperature, the corresponding Qdot size significantly reduced to ~4 nm and ~50 nm. This was primarily attributed to the suppression of As/P exchange during low temperature growth which also helped in increasing the Qdots density considerably to around $10^{10}$ cm$^{-2}$ [51]. In addition, an ultra-thin (~2 ML) GaAs interlayer sandwiched between the InGaAsP buffer layer and the InAs Qdots layer was also proposed to control the emission wavelength of the Qdots. The average Qdot height reduced from 6 nm to 3.1 nm, and the peak PL emission wavelength blue shifted from longer than 1.6 µm to 1.58 µm, measured on the sample grown with and without the GaAs interlayer, respectively. This was ascribed to the effective suppression of As/P exchange during InAs Qdots growth by the GaAs layer, and also to the consumption of surface-segregated In on the InGaAsP layer, leading to reduction of the

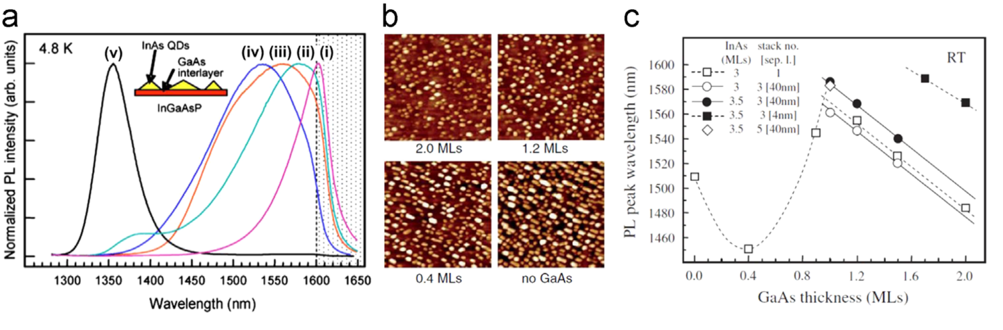


Fig. 9. (a) Normalized PL spectra at 4.8 K of the 3 ML InAs single Qdot layer grown: (i) without, and (ii) with 2 ML GaAs interlayer. (iii)–(v) PL spectra of Qdots with 2 ML GaAs interlayer and 45 s flushing time grown at TBA flow rates of (iii) 6.1, (iv) 2.0, and (v) 1.0 sccm. The shaded area in (a) is above the detection limit at 1.6 µm. (b) AFM images ($1 \times 1$ µm$^2$) of 3 ML InAs single stack Qdots with different GaAs interlayer thickness. (c) PL emission wavelength at room temperature as a function of GaAs interlayer thickness of single and vertically stacked InAs Qdot layers formed using various amount of InAs, InGaAsP separation layer thicknesses, and number of Qdots stacks. The inset of (a) shows a single InAs Qdots structure with GaAs interlayer on InGaAsP buffer layer. Reproduced from [50,52,54].

Qdots size. An additional flushing step of trimethyl–gallium (TMG) under tertiarybutyl-arsine (TBA) after the interlayer growth was also employed to ensure the presence of pure TMI as group III source for Qdots growth. This gas switching sequence was done to minimize the composition inhomogeneities in the Qdot layer. Similar reduction in the Qdot size was also observed on reducing the V/III ratio which effectively controls the As/P surface exchange reaction [52] as illustrated in Fig. 9(a). It was also indicated that the thickness of the GaAs interlayers can be used as a parameter to tune the emission wavelength of the InAs Qdots, as shown in Fig. 9(b) and (c). The reduction in the GaAs interlayer thickness from 2 ML to 1.2 ML red shifted the PL emission wavelength of a single stack sample with improved PL efficiency. The resultant Qdots height increased from 4.5 nm to 5.6 nm, respectively, a direct result of continuous reduction of As/P exchange and consumption of surface-segregated In with GaAs layer thickness. Qdashes elongated along [0–11] were shown to emerge for GaAs layer smaller than 1 ML, as depicted in Fig. 9(b), due to low group V flow, which changed the properties of the InGaAsP surface to cause anisotropic surface diffusion along [0–11] leading to Qdash formation for sub-monolayer GaAs coverage. In fact, the GaAs interlayer assisted growth method was also shown to successfully reproduce identical Qdots stacks with thick separation layers, as summarized in Fig. 9(c) [53]. With increasing InAs deposition and GaAs layer thickness, the tuning of PL emission wavelength of the multi-stacked InAs/InGaAsP Qdots was possible.

Rather than tuning the emission wavelength of Qdots *via* changing the buffer layer surface growth kinetics, Jang et al. [55] utilized Qdots material composition instead. In(Ga)As/InGaAsP Qdots were grown on exact (100) InP substrate using MOCVD technique. By controlling the composition of In(Ga)As Qdots material, PL emission in the range of 1.35 to 1.65 μm was achieved. The Qdots size increased while the height decreased with the increase in the relative concentration of TMG to TMI during the Qdot growth. In addition, Qdot density as high as $1.13 \times 10^{11}$ cm$^{-2}$ was obtained with higher concentration of group III alkyl supply. A 5-stack In(Ga)As/InGaAsP Qdot sample showed a PL emission and linewidth of 1.5 μm and 63 meV, respectively, at room temperature [56]. In another study, Michon et al. [57] showed that additional P flux during the MOCVD growth of InAs Qdots on InP buffer layer also allowed tuning of Qdots emission around 1.55 μm. It was shown that increasing the $PH_3/AsH_3$ ratio from 0 to 50 blue shifted the PL peak wavelength from $\sim$1.88 μm to $\sim$1.38 μm with a reduced PL linewidth, enlightened by the kinetic effects due to additional P flow and energetic effects due to the reduction in the lattice mismatch between Qdots material and (100) InP substrate.

Growth of InAs Qdots on exact (100) InP by means of CBE was introduced by Poole et al. [58], via depositing a thin 2–5 ML of InAs on a buffer layer followed by a growth interruption under As overpressure to avoid surface degradation, similar to the work reported by Fafard et al. on MOCVD grown InAs/InP Qdots [24]. A clear transformation from a two dimensional (2D) Qwell state to one dimensional Qdash state elongated along [0–11] direction, and eventually to 0D islands was observed as a function of growth interrupt time. The Qdashes were 20–25 nm wide and 40–130 nm long while the Qdots were 25–40 nm wide. A red shift in the PL emission with decreased PL linewidth indicated a continual increase in Qdot height and uniformity with growth interruption time. Moreover, a high overpressure of As flux during growth interruption favored Qdot growth while a very low As overpressure resulted in the formation of 2D InAs Qwell layer [58]. Alteration to the growth rate of the Qdot capping layer was also examined via PL measurements, as shown in Fig. 10(a), and found that higher growth rate reduced the As/P exchange at the Qdots surface and preserve the Qdot size and shape (indicative of red shift in the PL emission), thus able to control the Qdot emission wavelength. This was required since the

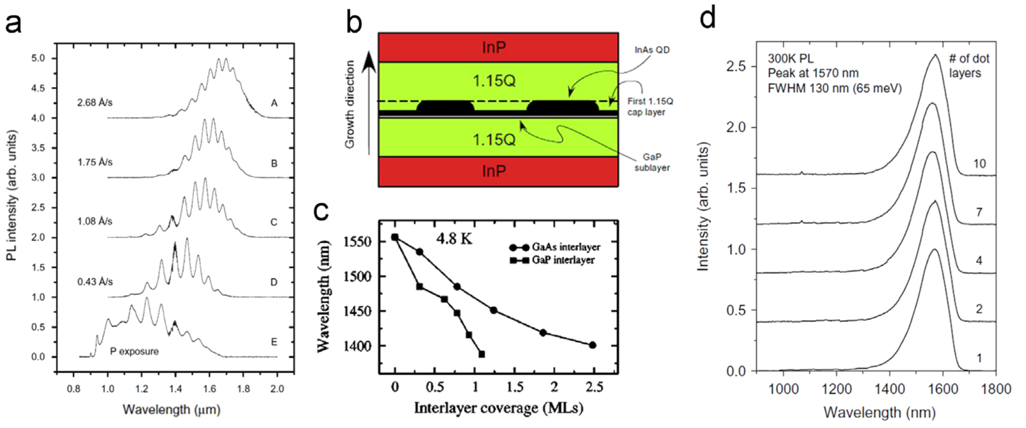


Fig. 10. (a) Normalized PL spectra of InAs/InP Qdots as a function of growth rate of InP capping layer at 4 K. (b) A single double capped layer structure with underneath GaP layer. (c) Tuning capability obtained from the PL emission wavelength at 4.8 K, of a single InAs/InP Qdot layer on a GaP and GaAs interlayer, as a function of intelayer coverages. (d) Normalized PL spectra of InAs/InP Qdots as a function of number of stacking layers at 300 K, and utilizing double capping technique with GaP underlayer. Adapted from [65,69,70].

buried dots tend to become shorter compared to the surface dots due to exposure to P flux during capping [59] which caused the InP adatoms (formed at the top layer of InAs) to migrate towards the region in between the Qdots due to the strain mismatch. This process was further improved by a double capping procedure [60], introduced by Ledentsov et al. [61] and Gutierrez et al. [62] on InAs/GaAs and InAs/InP Qdots, respectively, shown in Fig. 10(b). In this modified approach the region between the Qdots was first partially filled with a thin InP capping layer followed by a growth interruption under P overpressure where the As/P exchange was exploited to trim the taller Qdots which are not buried under thin capping layer compared to shorter Qdots. Later, a thick second capping layer was deposited. This significantly helped in controlling the Qdots height uniformity, and their emission energies.

Different ultra-thin interlayers were also utilized to tune the emission wavelength of InAs/InP Qdots grown by CBE system [63] on (100) InP substrate miscut 2° towards (110), similar to the MOCVD grown InAs/InP Qdots discussed above. As depicted in Fig. 10(c), both GaAs [64] and GaP interlayers blue shifted the emission wavelength due to suppressed As/P exchange and consumption of surface segregated In. The PL linewidths with increasing interlayer thickness remained within 45–55 meV at 4.8 K and the PL efficiencies were comparable. Smaller coverage of GaP was required to obtain the same wavelength blue shift compared to the GaAs coverage which was attributed to better effectiveness of GaP in suppressing the As/P exchange, as the GaP bond strength is stronger in the InGaAsP material system compared to GaAs [65].

High density InAs/InGaAsP Qdots active region are highly desirable in realizing optoelectronic devices for photonic integrated circuits. This motivated the research community to continue growing Qdots on (311)B InP substrates [66] instead of (100) InP substrate for device demonstrations. Balancing the built-in strain caused by Qdots became crucial in a multi-stack structure, since the generated strain field in the subsequent capping layers causes variation in its composition leading to preferential Qdot growth from layer to layer. This in turn encourages the Qdot size to grow resulting in degradation of Qdot uniformity, as observed in the InAs/GaAs material system [67]. Combining the double capping procedure and employing a GaP interlayer, Poole et al. [68] was able to stack 1 to10 layers of InAs/InGaAsP Qdots without any change in PL peak wavelength or PL linewidth, as shown in Fig. 10(d). Furthermore, tuning the emission wavelengths of the Qdots was also demonstrated by means of InAs deposition rate and the first capping layer thickness. A red shift in the PL peak wavelength was observed on increasing the thickness of first cap or decreasing the InAs deposition rate which was ascribed to the change in the Qdots height as a consequence of As/P exchange process [68].

MBE growth of InAs/InGaAsP Qdots was carried out by Li et al. [71] and Elias et al. [72] on exact and vicinal (100) InP substrates, respectively. Without assistance of any additional growth techniques which is normally required in MOCVD and CBE growth of InAs/InGaAsP Qdots, a $10^{10}\ cm^{-2}$ areal density of Qdot is reported with room temperature PL emission wavelength and linewidth of 1.55 μm and 108 meV, respectively. The Qdots were slightly elongated along the [01–1] direction with mean diameter and height of 76 nm and 2.9 nm, respectively, similar to the InAs/InAlGaAs Qdots grown in MBE by Kim et al. [41], discussed in Section 2.1.2. By adjusting the thickness of the InAs layer and the growth temperature, wavelength tuning of the Qdots was achieved [73]. It was observed that increasing the InAs layer thickness beyond 3 ML transforms the Qdot-like structures to Qdashes elongated along [0–11] direction with red shifting of the PL emission wavelength. This was attributed to the In migration on the surface of InGaAsP along [100] direction. A value of 3.5 ML was suggested to be the critical thickness for the formation of Qdots.

Recently, Jo et al. [74] explored utilization of Qdot-in-a-well (DoWELL) structure to improve the laser device performance. InAs Qdots were sandwiched between 1.35 μm InGaAsP Qwell and further embedded in 1.15 μm barrier layer on (100) InP substrate. GaAs interlayer was utilized to maintain the Qdot wavelength tuning for a seven stack structure. The Qdot density in DoWELL structures were found to be slightly lower ($\sim 2\times10^{10}\ cm^{-2}$) than that of Qdots on InGaAsP buffer layer without GaAs interlayer ($\sim 2.6\times10^{10}\ cm^{-2}$). This was believed to be due to alteration in the migration characteristics of In atoms on GaAs surface during the In and As precursor supply. The PL linewidth and efficiency of DoWELL structures substantially decreased (from 92 meV to 68 meV) and was attributed to a combined effect of enhanced carrier capturing [74]. This is a well-established technique utilized in InAs Qdots on GaAs substrate system for device performance improvement [2].

The thrust to increase the InAs Qdot density on (100) InP substrate rather than relying on (311)B InP substrate which is incompatible with the standard laser fabrication process, led to the exploration of misoriented substrates. These substrates helped in modifying the In diffusion length arising from the atomic steps thus resulting in more isotropic nanostructure formation, as discussed initially in this section. Elias et al. [72] employed a growth interruption step after InAs deposition on 1.18 μm InGaAsP buffer layer for 30 s under As overpressure, and compared the nanostructure formation on the nominal (N), and 2° off-cut towards (111)A and (111)B, (100) InP substrates forming surface steps namely; A steps and B steps which will be used henceforth. At high As flow rate, larger ($\sim$50 nm diameter) and lower density ($\sim 2\times10^{10}\ cm^{-2}$) Qdots were formed independent of the substrate orientation. However, at low As flow rate, smaller and higher density Qdots were formed on vicinal (100) InP miscut towards (111)B while the other two substrates showed Qdash formation, as shown in Fig. 11. This was attributed to the lower step energy of InAs A steps (along [1–10]) than B steps (along [110]) and thus of the shorter diffusion length of In in the [110] direction. Furthermore, the effect of growth temperature did not significantly change the Qdot structural and optical characteristics which indicated that the effective diffusion length of the adatoms on the surface is limited by the presence of steps. An improvement in the Qdot density from $7\times10^{10}\ cm^{-2}$ to $9\times10^{10}\ cm^{-2}$ and a weak decrease in average dot height (from 2 to 1 nm) and diameter (from 35 nm to 26 nm) were observed on

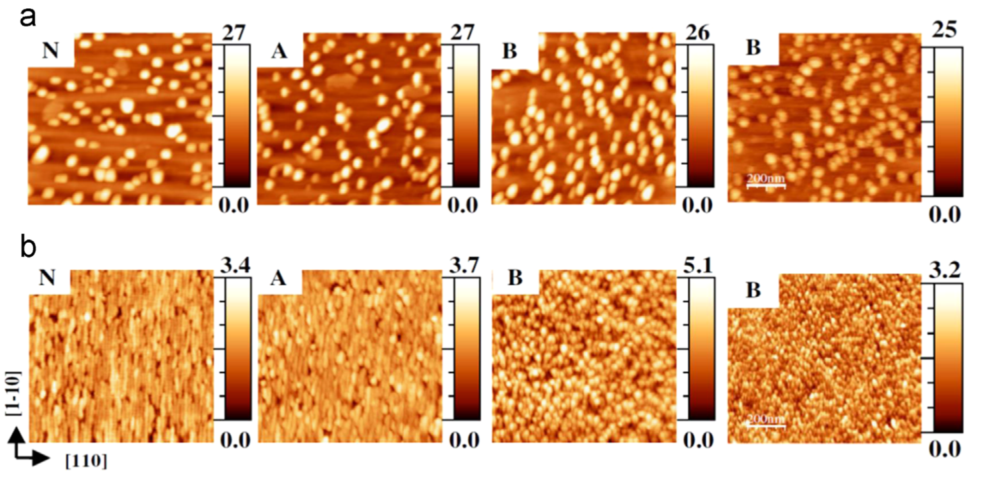


Fig. 11. AFM images ($1 \times 1\ \mu m^2$) of InAs/InP nanostructures deposited on nominal N, A, and B surfaces under two different As fluxes at (a) 6 and (b) 0.3 sccm. The first three columns from the left were grown at 480 °C while the last column was grown at 400 °C. The height contrast scale is in nm. Courtesy of [75].

decreasing the growth temperature [75]. In brief, an aerial InAs/InGaAsP Qdot density on exact (100) InP substrate was measured in the range of $\sim 2 \times 10^{10}$–$4 \times 10^{10}\ cm^{-2}$ and up to $9 \times 10^{10}\ cm^{-2}$ from vicinal substrates [72].

### 2.2.2. *Qdots on (311)B InP substrate*

Growth of InAs Qdots on the high index (311)B InP substrate permitted the reproducible formation of dense and small size Qdots when compared to Qdots grown on the nominal (100) InP substrate, under same growth conditions. This was demonstrated by Frechengues et al. [59] on InAs/InGaAsP material system grown by MBE. A dot density of $5 \times 10^{9}\ cm^{-2}$ was reported on (100) InP with highly inhomogeneous large size Qdots (70 nm diameter and 16 nm height) whereas $5 \times 10^{10}\ cm^{-2}$ density was obtained on the (311)B InP with uniform small dots (35 nm diameter, and 8 nm height), as shown in Fig. 12 (a) and (b). Furthermore, tunability of the Qdot emission wavelength was obtained by annealing the InAs Qdots under P overpressure before the InGaAsP capping layer growth, and the substrate temperature. By this modification of the As/P flux sequence a wavelength tunability of $>250$ meV was obtained at high substrate temperature around 1.55 μm and is illustrated in Fig. 12(c).

Dispersive size Qdots are highly undesirable as they deteriorate a laser performance if used in active region. This issue was addressed by Paranthoen et al. [76] on (311)B InP substrate by demonstrating reduced PL linewidth via double capping technique, discussed earlier in this review [60], on the MBE grown InAs/InGaAsP Qdots also. It was shown that the two step capping separated by a growth interruption under P flux decreased the inhomogeneity of Qdots with density and mean dot diameter (height) of $5 \times 10^{10}\ cm^{-2}$ and 30 (8) nm, respectively. The room temperature PL linewidth drastically reduced from 120 meV to 50 meV at $\sim 1.55$ μm using this modified technique. Moreover, a similar red shift in the PL emission wavelength was observed on increasing the thickness of the first InP cap, as seen in the CBE grown InAs/InGaAsP Qdots, and was attributed to the As/P exchange procedure [77]. In continuation to this work, Caroff et al. looked into the effect of first InGaAsP capping layer thickness (see Fig. 13(a)), different growth interrupts overpressure types *viz.*

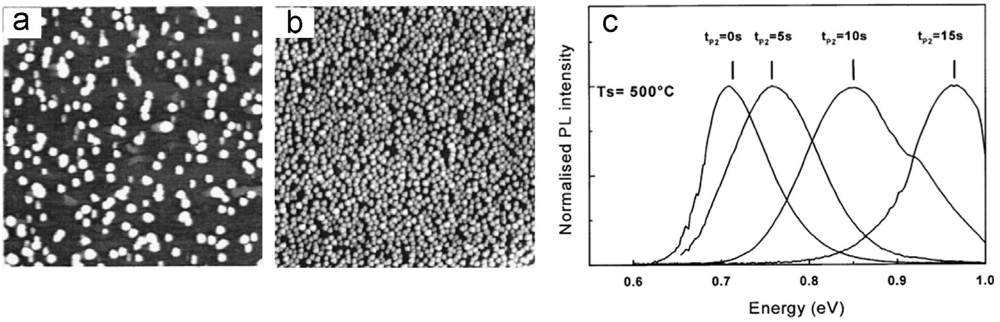


Fig. 12. AFM images ($2 \times 2\ \mu m^2$) of the uncapped InAs Qdots on (a) (100) InP and (b) (311)B InP substrate. (c) PL spectra of the InAs Qdots on (311)B InP substrate after a growth interruption under P overpressure for various times at the substrate temperature of 500 °C. Taken from [80].

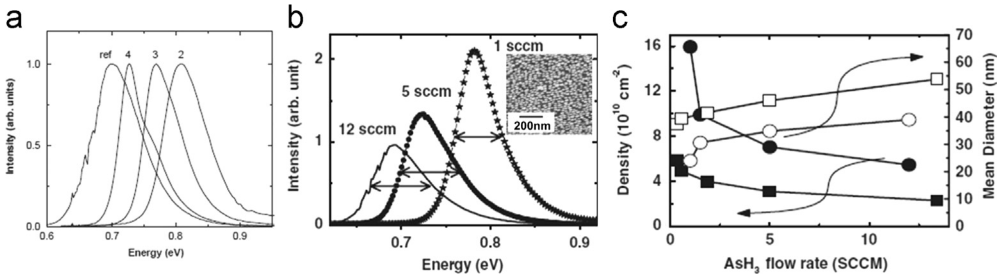


Fig. 13. Room temperature PL spectra of (a) double capped samples with first InGaAsP (Q1.18) cap layer thicknesses of 4, 3 and 2 nm and a growth interrupt under a combined $As_2$ and $P_2$ overpressure during 120 s. (b) Single capped InAs/InGaAsP Qdot samples with different As flow rates during the growth interruption of 30 s after InAs deposition. (c) Changes in Qdots density (filled symbols) and mean diameter (empty symbols) versus As flow rate during the growth interruption of 30 s after InAs deposition on InGaAs (square symbols) and InGaAsP (circle symbols) buffer layers. The inset of (b) is an AFM images of the uncapped InAs/InGaAsP Qdots at an As flow rate of 1.0 sccm. Taken from [31,78].

As, P and As and P, and the growth interrupt duration, on the Qdots emission [78]. A red shift (blue shift) in PL peak wavelength was observed on decreasing (increasing) the first cap thickness under As (P or As and P) which was discussed in terms of the compressive (tensile) stress experienced by InGaAsP first capping layer due to InAs (P-rich) surface as a result of alteration in the As/P exchange process. Qdots with GS emission tuning capability from $\sim 1.3\ \mu m$ to $\sim 1.8\ \mu m$ was possible. In another study Ulloa et al. [79] showed that the height of the Qdots correspond to the thickness of the first cap layer up to 3.5 nm which indicated the double capping procedure's effectiveness in controlling the Qdots height.

With already noteworthy accomplishment in InAs/InP Qdots density reaching $\sim 5.5 \times 10^{10}$ cm$^{-2}$ on (311)B InP substrate, Caroff et al. [31] further explored the possibility of attaining values beyond $10^{11}$ cm$^{-2}$ as this value was already achieved in InAs/InAlGaAs Qdots system on (311)B substrate (see Section 2.1.1). By reducing the As flux during InAs Qdots formation, it was shown that the Qdot density dramatically increased up to $1.6 \times 10^{11}$ cm$^{-2}$ and the room temperature PL linewidth decreased from 70 meV at 12 sccm As flux to 50 meV at 1.0 sccm, as depicted in Fig. 13(b) [81]. Furthermore, the Qdots height (diameter) decreased from 7.7 (19.5) nm to 4.8 (12) nm, thus, blue shifting the PL peak wavelength from $\sim 1.79\ \mu m$ to

~1.58 μm. This trend of the effect of As overpressure was found to be independent of the buffer layer nature as shown in Fig. 13 (c), and hence was related to increase in the strained InAs (311) B surface energy on decreasing As overpressure which in turn increased the instability of the growth front and favored Qdots nucleation leading to large Qdots density.

Stacking of InAs/InGaAsP Qdots on (311)B InP utilizing double cap technique was also proven by Bertru et al. as highly efficient in maintaining the Qdot uniformity with a spacer layer thickness around 40 nm [82]. The room temperature PL emission at 1.55 μm with linewidth of 62 meV were maintained for a single stack and six stacks of Qdots, attributed to the reduced mean strain accumulated which drastically reducing the PL energy shift.

### *2.3. Post-growth tuning of InAs/InP Qdots*

Instead of achieving tunability of self-assembled Qdot dimensions and composition in order to control the emission wavelength and uniformity during the growth process, post growth bandgap engineering was also carried out to blue shift the InAs/InP Qdots emission towards 1.55 μm regime. Different tuning process such as rapid thermal annealing (RTA), impurity-free vacancy disordering (IFVD), laser-induced intermixing (LII), grown-in-defects (GID) mitigated intermixing, and ion-implantation-induced disordering (IID) have been proposed. Girard et al. [83] performed a simple RTA on InAs/(100)-InP Qdots grown by CBE method, and reported a blue shift of up to 120 meV (reference as-grown sample PL emission at ~1.55 μm) at 650–800 °C for 210 s on both conventional single capped sample and samples with double capping procedure. Chia et al. [84] investigated the post-growth group-V intermixing of MOCVD growth InAs/(100)-InP Qdots via IFVD with $SiO_2$ and $SiN_x$ capping and LII with 1.064 μm CW laser source. A substantial improvement in the PL peak intensity and linewidth was observed with energy blue shift as large as 350 meV from the reference sample emission at 1.65 μm, as shown in Fig. 14(a). A maximum differential energy shift between the two capped samples at 850 °C was 90 meV. From LII process a differential energy shift of >250 meV was demonstrated. In another study, Wang et al. [85] reported post growth bandgap tuning of InAs/InP Qdots in InGaAlAs Qwell laser structure via $SiO_2$ and $Si_xN_y$ capping. The IFVD process resulted in larger bandgap blue shift from the latter cap compared to former one with a differential shift of 92 nm after annealing at 800 °C for 30 s. This was related to the dominant In diffusion with respect to other group-III atoms.

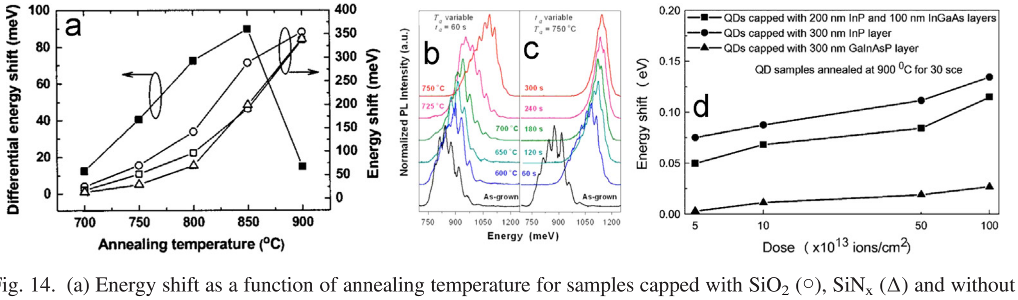


Fig. 14. (a) Energy shift as a function of annealing temperature for samples capped with $SiO_2$ (○), $SiN_x$ (Δ) and without dielectric cap (□). Also shown is the differential energy shift (■) for samples capped with $SiO_2$ and $SiN_x$. PL spectra from as-grown and annealed GID samples (b) as a function of annealing temperature $T_a$ for an annealing time $t_a$=60 s and (c) as a function of $t_a$ for $T_a$=750 °C. (d) The implantation-induced energy shifts of the quantum dots capped with InP, InP and InGaAs, and InGaAsP layers and annealed at 900 °C for 30 s. The implantation dose is varied from $5\times10^{13}$ to $1\times10^{15}$ ions/cm$^2$. Collected from [84,86,87].

The GID induced intermixing by introduction of point defects into the epitaxial layers during growth at reduced temperatures was demonstrated by Dion et al. [86]. Energy shifts of 270 meV (~1.5 μm to ~1.1 μm) from the CBE grown InAs/(100)-InP Qdots sample with low temperature grown InP (LT-InP) layer was reported after annealing at 750 °C for 300 s and is illustrated in Fig. 14(b) and (c). This was attributed to the presence of a non-equilibrium concentration of point defects in the LT-InP which was confirmed by the progressive etching of this layer which led to the gradual quenching of the PL shift. The effect of the influence of post-growth phosphorus implantation [88,89] and proton-implantation [87] followed by RTA was carried out on the CBE and MOCVD grown InAs/(100)-InP Qdots with InP capping layer and with thin GaAs interlayer capped with InGaAs or InGaAsP capping layer. A large P implantation induced blue shift of up to 325 meV (~1.48 μm reference sample) was observed by Dion et al. [88]. On the other hand, Barik et al. [87] reported high proton implantation-induced energy blue shift due to strong group V interdiffusion, and the least blue shift from the Qdots capped with InGaAsP layer due to weak group V and group III interdiffusion. In addition, higher dose decreased the PL linewidth of the samples due to homogenization of Qdots as a result of interdiffusion which is shown in Fig. 14(d).

### 2.4. Towards >2.0 μm wavelength emission

From the discussion in Sections 2.1 and 2.2 it is clear that most of reported work was interested in blue shifting the InAs/InP Qdots luminescence emission at 1.55 μm in the C–band telecommunication window for optical communications because of their inherent long wavelength emission beyond 1.55 μm due to the reduced lattice mismatch between InAs Qodts and InP substrate. Attempts to push the InAs/InP Qdots emission wavelength other way around and extending beyond ~1.8 μm has recently attracted attention owing to the various cross-disciplinary field applications of such devices in spectroscopy and sensing [90] as discussed in Section 1. In this respect, alteration of various growth parameters that resulted in the red shifting of InAs/InP Qdots emission; for instance, increasing the thickness of the InAs deposition or the growth interruption time before capping the dots or the thickness of the first capping layer in the double capping procedure, etc. could be exploited to attain the desired wavelength. However,

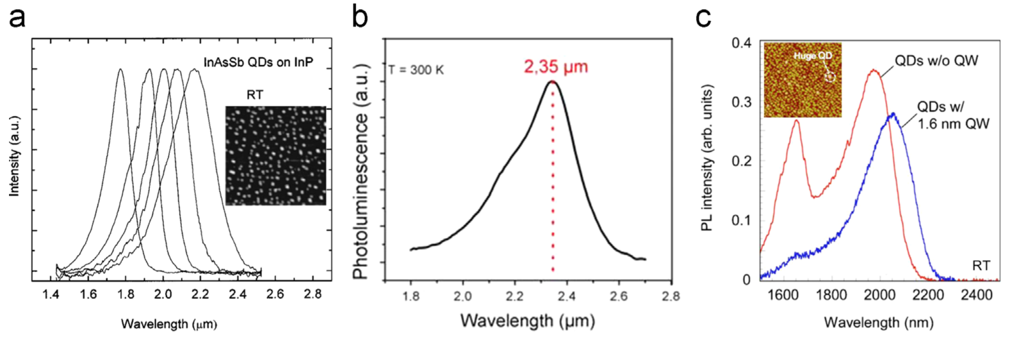


Fig. 15. (a) Normalized room temperature PL spectra of InAs(Sb) Qdots and almost pure InSb Qdots (emission at 2.2 μm) self-assembled on InGaAs/(100) InP. (b) Room temperature PL spectrum of self-assembled InAsSb nanostructures on InGaAs lattice-matched to (100) InP. (c) Room temperature PL spectra of InAs Qdots directly grown on 20 nm InGaAs and on 1.6 nm InAs QW. The inset of (a) and (c) are the AFM images of $0.75 \times 0.75\ \mu m^2$ and $1.25 \times 1.25\ \mu m^2$ size InAsSb Qdots self-assembled on InGaAs/(100) InP and the extremely dense InAs Qdots on Qwell with a huge QD indicated, respectively. Reproduced from [93–95].

the maximum room temperature PL emission wavelength reported from these nanostructures is about ~1.8 μm. To further increase the emission wavelength, Zhukov et al. [91] proposed and demonstrated utilization of InGaAs matrix layer on (100) InP substrate for the growth of InAs Qdots. 77 K PL studies as a function of InAs ML deposition on $In_{0.53}Ga_{0.47}As$/InP showed a wavelength tunability from ~1.7 μm to a maximum of ~1.95 μm. Another alternative to extend the emission wavelength was to incorporate Sb during the growth of InAs Qdots on InP substrate [92,93]. Qui et al. [93] reported this possibility by growing InAsSb Qdots on (100) InP substrate using MOCVD. A dot density as high as $4\times10^{10}$ cm$^{-2}$ was obtained via self-assembled growth by alternating group III and group V precursors, and almost pure InSb dots were formed on $In_{0.53}Ga_{0.47}As$/InP substrate with room temperature PL emission at 1.7–2.2 μm, as depicted in Fig. 15(a). In another study, Dore et al. [94] also reported a room temperature PL emission at 2.35 μm from InAs(Sb) Qdots embedded in InGaAs alloy lattice matched to (100) InP. In this case, after the deposition of InAs, a growth interrupt under Sb flux was carried out before capping with the InGaAs layer. The result is plotted in Fig. 15(b).

Recently, Kotani et al. [95] reported an emission wavelength of 2.06 μm from optimized growth conditions of InAs Qdots by capping with 5 nm lattice matched InGaAs layers before the thick InGaAsP buffer layer deposition on vicinal (100) InP substrate using MOCVD growth method. The red shift in the emission wavelength due to the InGaAs layer was attributed to a larger In adatom surface migration length on InGaAs. In addition, by compressively straining InGaAs layer, a red shift in the PL emission was observed reaching 2.16 μm. Successively, growth of InAs Qdots on top of 1.6 nm InAs Qwell (dot-on-well) was also proposed and demonstrated which resulted in an increase of dot density and with room temperature PL emission at 2.05 μm, as shown in Fig. 15(c). All these efforts shows the potential of InAs/InP Qdots material system in achieving emission beyond 2 μm, and thus open up routes for further extending the emission wavelength via InAs(Sb)/InP Qdots material system with already demonstrated CW semiconductor laser diode operation from this material system with lasing near 2 μm [96,97].

## 3. InAs/InP Qdots Devices

In this section, the achievements of InAs/InP Qdots as the gain region in various semiconductor devices is reviewed. The section begins with the discussion on the accomplishment of narrow band Fabry-Perot (FP) edge-emitting semiconductor lasers performance. These lasers are based on optimized InAs/InP Qdots active region discussed in Section 2. Later, the inherent inhomogeneous broadening from multi-stack InAs/InP Qdots active region which usually results in a broadband gain profile and hence electroluminescence, was exploited to realize broadband semiconductor components such as SOAs and SLDs. In addition, this characteristic also results in broadening of multimode lasing spectra under stimulated emission with increasing current injection due to many Qdots taking part in capturing the carriers. This formed the basis of realizing semiconductor broadband lasers, mode-locked lasers, multi-wavelength and tunable lasers, which are summarized later in this section.

### *3.1. InAs/InP Qdots lasers*

The first InA/InP Qdots laser was reported at 77 K by Ustinov et al. [98,99] in InGaAs matrix layer lasing at ~1.9 μm, and subsequent room temperature operation [100]. Later, extensive research in Qdots growth was conducted to achieve high quality InAs Qdots on InP substrate.

The active region design developments were carried out on both high index (311)B InP, and exact or vicinal (100) InP substrates. In the following, we review the perfromance achievements in InAs/InP Qdot lasers on these substrates concentrating on (i) InAs/InGaAlAs and (ii) InAs/InGaAsP material systems.

### 3.1.1. Lasers on (311)B InP substrate

*3.1.1.1. InAs/InGaAsP material system.* The first 77 K [100] and room temperature [103] demonstration of long wavelength lasing at ~1.4 μm was reported by Nishi et al. using a 7 stack InAs/InGaAsP Qdots active region on (311)B InP substrate grown by MBE. The lasing action was originated from the Qdots ES with threshold current densities ($J_{th}$) 0.54 kA/cm$^2$ and 4.8 kA/cm$^2$, respectively. The device was based on separate confinement heterostructure (SCH) design with Qdot density $2 \times 10^{10}$ cm$^{-2}$. Later, with the improvements in the growth techniques to blue shift the Qdot emission and increase the density and uniformity which improves the laser performance, in particular, the threshold current density, different reports started to appear; from demonstration of optically pumped InAs/InP Qdots laser at 1.52 μm [77,104] to eventual electrically injected high-gain and low-threshold InAs/InP Qdots laser by Caroff et al. [101]. The latter results are summarized in Fig. 16(a) and (b). By using the double capping technique with a growth interruption under As overpressure, Caroff et al. achieved a Qdot density of $1.1 \times 10^{11}$ cm$^{-2}$ and PL linewidth of 50 meV centered at 1.59 μm from the laser active region. The threshold current density and transparency current density were 190 A/cm$^2$ (63 A/cm$^2$ per layer) and 68 A/cm$^2$ (23 A/cm$^2$ per layer), respectively, with GS and ES lasing wavelength at 1.59 μm and 1.53 μm, respectively. These are the best threshold current density values reported in this material system with high ground-state modal gain of 7 cm$^{-1}$ per dot layer.

Shortly after this demonstration, employing high quality InAs/InGaAsP Qdots, Homeyer et al. [105] reported a record GS modal gain of 8 cm$^{-1}$ per Qdot layer and best internal quantum efficiency of 62% from their multi-stack laser devices while maintaining a low threshold current density of 85 A/cm$^2$ per Qdot layer. The GS and ES lasing were observed at 1.54 μm and 1.5 μm, respectively. The significant improvement in the growth of the material quality was

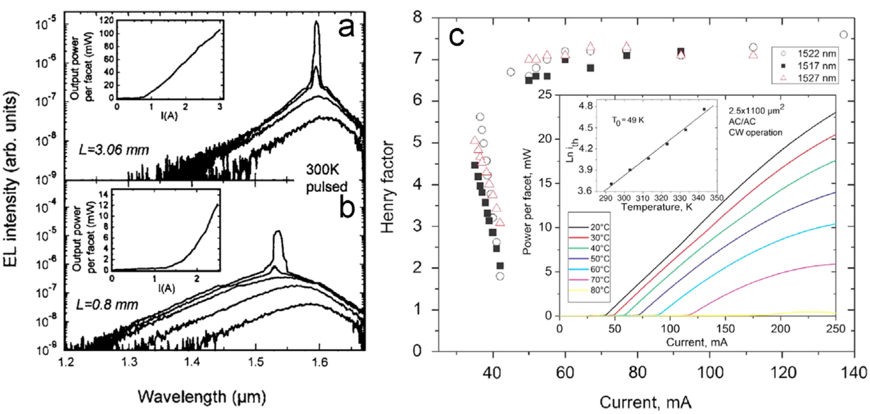


Fig. 16. Room temperature electroluminescence spectra under pulsed operation for several current densities for a laser cavity length of (a) 3.06 mm (65, 160, 208, and 220 A/cm$^2$), (b) 0.8 mm (65, 375, 1010, 1405, and 1800 A/cm$^2$). Insets are corresponding *L–I* characteristics per facet. (c) Linewidth enhancement factor(LEF) below and above threshold of a 1100 μm long InAs/InP (311)B InAs/InGaAsP Qdots laser. Inset shows the corresponding *L–I* characteristics with as-cleaved facets for temperature from 20 to 80 °C in CW regime and characteristic temperature. Taken from [101,102].

substantiated by: (i) lasing wavelength at 1.52 μm, originated from a single Qdot active layer on (311)B InP substrate under pulsed current injection [66], (ii) highest reported modal gain of 13 cm$^{-1}$ from a single stack InAs/InP Qdot laser [7,66], (iii) the largest dot density of $1.3 \times 10^{11}$ cm$^{-2}$ and (iv) low internal loss of 6 cm$^{-1}$ from Qdot lasers on (311)B InP [106]. However, the temperature stability of the InAs/InGaAsP Qdots lasers were comparatively poor compared to their InAs/InGaAlAs Qdots laser counterparts, due to the low conduction band offset arising from the mere 25–50 K characteristics temperature $T_0$ [101]. In general, the output power from the laser devices was reasonable, ranging from few tens (ridge-waveguide laser) to hundreds of mWs (broad area laser).

Dynamic performance of Qdots lasers on this material system and on (311)B InP substrate was reported by Martinez et al. [102] employing a single mode ridge-waveguide laser structure. GS lasing at 1.52 μm and *L–I* characteristics visible up to 75 °C with a CW current injection of >200 mA was observed, as depicted in Fig. 16(c). Moreover, measurement of linewidth enhancement factor (LEF) revealed a value of ~1.8 below threshold before increasing to ~6.8 above threshold. This was attributed to the band filling of higher energy levels in the wetting layer (see Fig. 16(c)). A maximum relaxation frequency and small signal bandwidth of 3.8 GHz and 4.8 GHz, respectively, were also deduced. In general, the lasers static and dynamic performances suggest further improvement of Qdot grown in the material system and on (311)B InP substrate.

*3.1.1.2. InAs/InGaAlAs Material system.* Saito et al. [27] first demonstrated the ground state lasing InAs/InGaAlAs Qdots laser on (311) B InP substrate at a wavelength of 1.63 μm, and threshold current density of 660 A/cm$^2$ (132 A/cm$^2$ per layer) from as-cleaved facets, and 380 A/cm$^2$ (76 A/cm$^2$ per layer) from high reflection coated facets, plotted in Fig. 17(a). The extracted internal loss was 3.6 cm$^{-1}$ which to the best of our knowledge the lowest reported value on any InAs/InP Qdots material system. However, after this work, the InAs/InGaAlAs Qdot material system on (311) B InP saw a huge gap since most of the research concentrated on the InAs/InGaAsP material system. It was after six years that Alghoraibi et al. [109] and Akahane et al. [35,110] re-visited this material system on 311(B) InP and reported low temperate

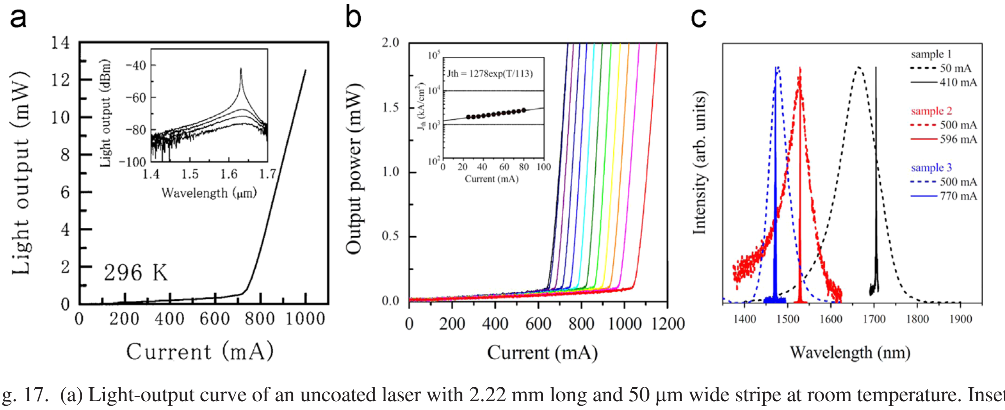


Fig. 17. (a) Light-output curve of an uncoated laser with 2.22 mm long and 50 μm wide stripe at room temperature. Inset is its electroluminescence at 200, 400, 600, and 850 mA. (b) Temperature dependent (25–80 °C) *L–I* characteristics of InAs/InGaAlAs/(311)B-InP laser comprising 30 InAs Qdots stacks in pulsed mode. Inset shows the relationship between threshold current density and temperature. (c) Electroluminescence and lasing spectra of 30 stacks InAs/InGaAlAs Qdots laser (sample 1, 2, and 3) below (dotted line) and above (solid line) threshold current value and showing the wavelength tuning capability. Adapted from [27,107,108].

and room temperature lasing, respectively, from multi-stack Qdots lasers. A negative characteristics temperature was measured at low temperature (100–130 K) by Alghoraibi et al. which was related to a delayed carrier thermalization within Qdot ensembles. By exploiting the Al atoms in the spacer layers and employing the strain compensation technique, Akahane et al. demonstrated room temperature lasing from a 30 stack InAs/InGaAlAs Qdots laser with GS lasing at 1.58 μm and threshold current density 2.7 kA/cm$^2$ (90 A/cm$^2$ per layer) from $10 \times 600$ μm$^2$ device, as shown in Fig. 17(b). In addition, by varying the amount of InAs deposition, composition and thickness of the spacer layers, the lasing emission was successfully tuned from 1.47 to 1.7 μm [107] which is illustrated in Fig. 17(c). Subsequently, with improvement in the material growth quality, Akahane et al. was able to reduce the threshold current density of the 30 stacked Qdots laser to 1.72 kA/cm$^2$ (57.4 A/cm$^2$ per layer) with extremely high temperature stability. The corresponding laser characteristics temperature $T_0$ was 114 K (20–75 °C) and further improved to 148 K (25–80 °C) from the 20-stack InAs/InP Qdots laser [108]. The threshold current density and $T_0$ values are found to be the best values ever reported on any InAs/InP Qdots system. However, high internal loss values of ~26 cm$^{-1}$ were extracted that was attributed to the imperfect coupling of the optical mode to the multi-stack Qdot gain media.

### *3.1.2. Lasers on (100) InP substrate*

*3.1.2.1. InAs/InGaAlAs material system.* Growth of Qdots on (100) InP substrate was challenging utilizing the InAs/InGaAlAs material system since the conditions always favored Qdash growth instead of Qdots. Consequently, utilizing an assisted growth techniques of a thin GaAs underlying layer before the growth of InAs Qdots on InGaAlAs matrix, Kim et al. demonstrated lasing up to 260 K [111], and later at room temperature [112], for the first time on a 7-stack Qdot (100) InP laser structure. The achieved threshold current density, Qdot density and lasing wavelength were 2.8 kA/cm$^2$ (400 A/cm$^2$ per layer), $6.0 \times 10^{10}$ cm$^{-2}$ and 1.5 μm, respectively. Later, the same groups reported room temperature lasing from 7-stacked shape-engineered AGQD Qdots active region with reduced threshold current density of 1.55 kA/cm$^2$ (220 A/cm$^2$ per layer) [42]. Furthermore, the AGQD laser performance was shown to be better than CQD laser performance which was attributed to the increase in the overlap integral between

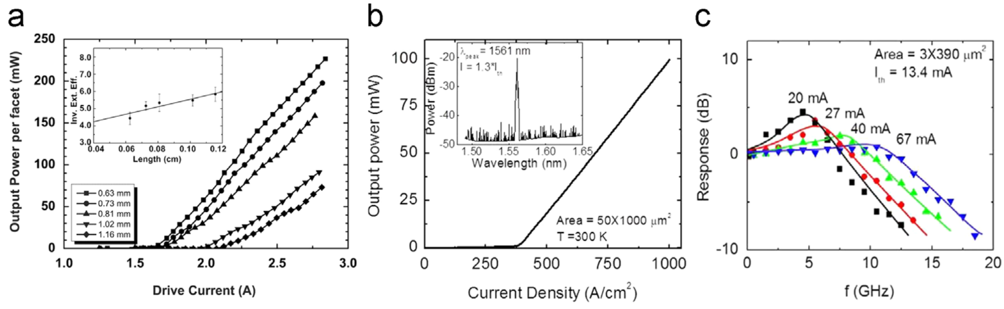


Fig. 18. (a) Plot of the light output power versus drive current of a broad area InAs/InGaAlAs/(100)-InP quantum dot laser at different cavity lengths. The inset depicts the reciprocal external efficiency versus the cavity length providing internal absorption and efficiency. (b) Measured light-current characteristics of a broad area tunnel injection quantum dot laser. Inset shows the lasing spectrum at $I = 1.3I_{th}$. (c) Measured small signal modulation response of ridge waveguide tunnel injection quantum dot laser. The solid curves are calculated modulation responses. The −3 dB modulation bandwidth measured for $I = 67$ mA is 14.4 GHz. Courtesy of [114,115].

the electron and hole wave-functions due to two times increase in the aspect ratio (height/width) of the AGQD compared to CQD [113]. More details of the AGQD and CQD Qdot growth was discussed in Section 2.1.2.

Recently, Gilfert et al. [114] reported a high gain and room temperature operation of InAs/InGaAlAs Qdots laser on (100) InP by growing in $As_2$ environment using MBE. A low internal loss of 4 $cm^{-1}$ and high gain of 15 $cm^{-1}$ per layer were reported, with lasing wavelength at 1.56 μm and threshold current density 1.95 kA/$cm^2$ (325 A/$cm^2$ per layer). The results are plotted in Fig. 18(a). Furthermore, by increasing the material growth quality and reducing the number of Qdots layers, Sichkovskyi et al. [4] reported a record high modal gain of 15.5 $cm^{-1}$ per layer and an extremely small PL linewidth of 25 meV at 10 K for their InAs/InP Qdots. The laser also showed high wavelength stability of 0.078 nm/K measured above room temperature. The dynamic characteristics of this laser was studied by Gready *et al.* [116] who reported small signal modulation bandwidth of 5 GHz and large signal modulation capability of 15 Gbps with 4 dB on/off ratio utilizing pseudo random bit sequence (PRBS). This very different response between the small signal and large signal modulations was attributed to the complex and highly nonlinear carrier dynamics of the InAs/InGaAlAs Qdots gain medium. Later, by further optimization of the Qdots gain section [117] a small signal modulation and the large signal modulation bandwidth were pushed to $>9$ GHz and 22 Gbps, respectively.

In a very recent demonstration, modulation p-doping and tunneling scheme was applied in the design of InAs/InGaAlAs multi-stack Qdots laser on (100) InP by Bhowmick et al. [115] and the device performance characteristics are plotted in Fig. 18(b) and (c). A low threshold current density of 390 kA/$cm^2$ (78 A/$cm^2$ per layer), a high characteristic temperature $T_0$ of 100 K (45–75 °C), near zero below threshold LEF and high modal gain of 14.5 $cm^{-1}$ per layer was reported, shown in Fig. 18(b). In addition, a small signal modulation bandwidth of 14.4 GHz was measured from the laser device which is the best value reported on any InAs/InP Qdot material system.

*3.1.2.2. InAs/InGaAsP Material system.* The FP semiconductor lasers investigated with InAs/InGaAsP Qdots on (100) InP were mostly based on CBE or MOCVD growth techniques until recently, growth using MBE system has also attracted attention. The first demonstration of the electrically injected InAs/InGaAsP/(100)-InP Qdots laser at low temperature (77 K) was reported on CBE system [118] followed by room temperature operation in both pulsed [119] and CW [120,121] operations. A pulsed threshold current density of 3.56 kA/$cm^2$ (713 A/$cm^2$ per layer) was reported by Allen et al. [119] who employed Qdots height trimming procedure with growth interruptions under As and As and P overpressures during the epitaxial growth of the active region. It was shown that higher barrier energy and Qdots densities ($1.5 \times 10^{10}$ $cm^{-2}$ versus $6.0 \times 10^{11}$ $cm^{-2}$) led to a significant improvement in laser threshold current and slope efficiency. Lelarge et al. [121], on the other hand, utilized a hybrid growth technique with MBE grown active region in conjunction with MOCVD grown p-doped cladding and contact layers. With this device growth configuration they demonstrated a CW threshold current density of 1.4 kA/$cm^2$ (240 A/$cm^2$ per layer) and 0.1 W/A slope efficiency from a buried ridge-waveguide laser, shown in Fig. 19(a). Lasing action was observed even from the 200 μm cavity showing a record high modal gain of 64 $cm^{-1}$ (10.7 $cm^{-1}$ per layer), and GS and ES lasing at ~1.5 μm and ~1.46 μm, respectively. As depicted in Fig. 19(b), an internal quantum efficiency and an internal loss of 0.37 W/A and 7 $cm^{-1}$, respectively, were extracted.

A gradual improvement in the laser performance was observed with the first demonstration of room temperature operation from InAs/InGaAsP Qdots lasers on MOCVD [50,54,122] and

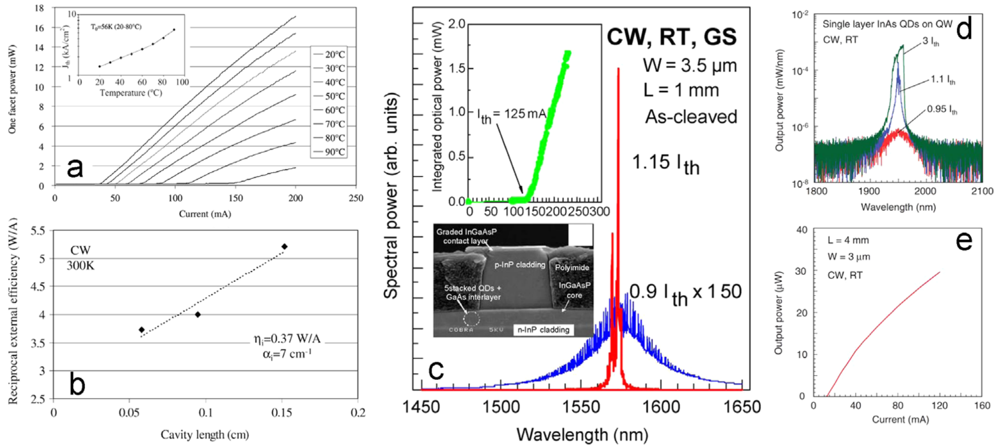


Fig. 19. (a) Output power versus injection current of a 2.5 × 1040 μm$^2$ buried ridge-waveguide InAs/InGaAsP/(100)-InP Qdot laser measured under CW operation in the temperature range of 20–90 °C. Inset shows the threshold current density versus temperature. (b) Reciprocal external differential efficiency of buried ridge-waveguide laser lasers versus cavity length measured under CW room temperature operation. (c) Amplified spontaneous emission and lasing spectra (CW, room temperature, Qdot GS) together with the *L–I* characteristics (upper inset) of the InAs/InGaAsP/(100)-InP Qdots laser shown in the scanning electron microscopy image (lower inset) (c) Amplified spontaneous emission and lasing spectra and (d) light output versus injection current curve of a single-layer InAs/InP Qdot-on-well laser emitting near 2.0 μm. Reproduced from [121,128,129].

MBE [71] system, by Notzel et al. and Li et al., respectively. The MOCVD growth laser showed a GS lasing wavelength at ~1.57 μm with comparatively reduced threshold current density of 615 A/cm$^2$ (123 A/cm$^2$ per layer). The extracted transparency current density and internal loss reached as low as 30 A/cm$^2$ (6 A/cm$^2$ per layer) and 4.2 cm$^{-1}$ which are among the best values reported values on (100) InP substrate and in this material system. The results are summarized in in Fig. 19(c). Benefiting from the optimized MOCVD growth process, including reduced As flow rate during Qdots growth and utilization of GaAs interlayer, the Qdots uniformity and emission in a multi-stack structure was maintained due to suppression of As/P exchange. On the other hand, MBE grown optimized Qdots laser showed a threshold current density of 790 A/cm$^2$ (158 A/cm$^2$ per layer) [71], large temperature stability with $T_0$ of 69 K (20–70 °C) [123], high wavelength stability of 0.08 nm/K (80–310 K) [124], and lasing around ~1.55 μm to ~1.65 μm. A small LEF of ~1.4–1.6 above threshold and < 1 below threshold, was measured recently by Jiao et al. [125] which is half the value reported by Lelarge et al. (~2.2 below threshold) [121], and the Qdots exhibited better uniformity with PL linewidth 63 meV at room temperature. Laser devices at low temperature [56] and room temperature [55,126] lasing from InGaAs Qdots on InGaAsP/(100)-InP were also reported with high Qdot density reaching value 1.1 × 10$^{11}$ cm$^{-2}$ and with notable performances.

Qdot lasers based on InAs/InGaAsP DoWELL [74] and InAs/InAs dot-on-well [127] active region design were also demonstrated after observation of their superior quality at material level which has been discussed in Section 2.2.1. As expected, the laser devices employing these structures showed improved performance attributed to the efficient carrier capturing process. Employing dot-on-well structure Kotani et al. [127] reported GS lasing at 1.74 μm from a single Qdot stack with threshold current density 2.75 kA/cm$^2$ and improved slope efficiency compared to a 5-stack Qdot laser structure. Furthermore, using an optimized growth conditions of the waveguide core and claddings and with minimum defect density, longest ever reported GS lasing wavelength of 1.95 μm from a single stack InAs/InP Qdot-on-well laser was demonstrated with an extremely low threshold current density of 100 A/cm$^2$ [128] which is plotted in Fig. 19(d) and (e). In general, the performance of InAs/InP Qdot lasers showed tremendous improvement in the past decade and is expected to be comparable to the performance of the InAs/GaAs Qdots lasers very soon. which have already achieved a threshold current density of 17 A/cm$^2$ [2].

### *3.1.3. Multiwavelength lasers*

Application of InAs/InGaAsP/(100)-InP Qdots gain chip in conjunction with the external cavity laser system (ECLS) in Littrow configuration was first reported by Allen et al. [119,130]. In this system, a single lasing mode can be tuned at a special angle of blazed gratings. A broad electroluminescence profile of 175 nm was achieved before lasing from the ridge waveguide laser device and when used in the ELCS, a tuning range as large as 110 nm was demonstrated. Shorter cavity laser diodes showed broader wavelength tunability than longer cavity diodes but at the expense of high threshold current density. The internal loss of the system was estimated to be 20–30 cm$^{-1}$ [131]. In the same year, Ortner et al. [132] showed improved tunability from the InAs/InP Qdots ECLS with a value of 166 nm, illustrated in Fig. 20(a). The key idea was to coat a high reflection layer on one facet and antireflection coating on the other facet. Under pulsed operation, an output power as high as 6 μW was obtained when tuned at 1.571 μm wavelength. The threshold current density was found to increase at the extreme gratings angles which was attributed to the decrease in the Qdots material at extreme short (higher density of states but decrease in the occupational probability at a given current injection), and long (reduced density of states) wavelengths. A high output power up to 24 mW at a tuned wavelength of ~1.594 μm in the ECLS was reported by Chen et al. [133] on the 8 × 1500 μm$^2$ InAs/InGaAsP on (100) InP Qdots laser. A maximum tunable range of 70 nm was obtained with a threshold current density < 1.62 kA/cm$^2$. By utilizing smaller device size, the tuning range was increased to 98 nm but at the expense of higher threshold current density of 3.33 kA/cm$^2$. This is shown in Fig. 20(b) and (c). A more detailed review on the ECLS on InAs/InP Qdots lasers was performed by Li et al. [131].

In the lasing mode, the large gain bandwidth and Qdots gain saturation usually results in broadening of the lasing spectra with increasing current injection. The resulting spectra could be very wide and flat-topped. This feature was exploited to realize multiwavelength laser where the sharp line corresponding to the FP modes represents a channel with spacing determined by the

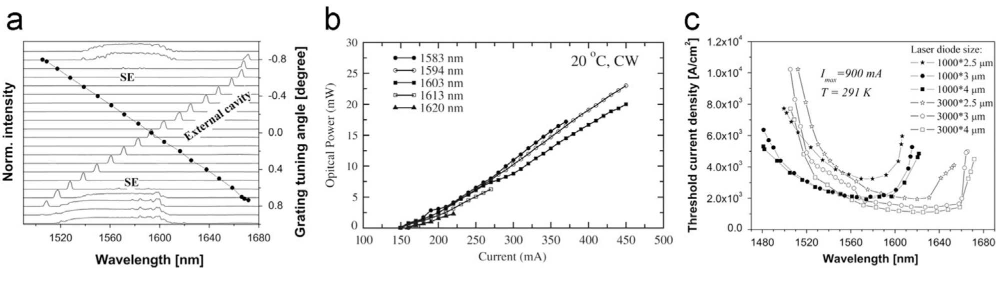


Fig. 20. Spectra of the ECLS displaying the peak linearly tuned (full circles) in wavelength with the angular position of the blazed grating. The InAs/InGaAsP Qdots laser diode size is 4 × 3000 μm$^2$. Note that simultaneous spontaneous emission of the QD ensemble also emerges. (b) *L–I* curves of 8 × 1500 μm$^2$ InAs/InP Qdots laser in ECLS configuration at different operating wavelengths. (c) Threshold current density as a function of laser wavelength for different device lengths and widths as denoted by the different symbols. An upper limit for the injected current has been set to 900 mA to avoid damaging the laser diode. Adapted from [130,132,133].

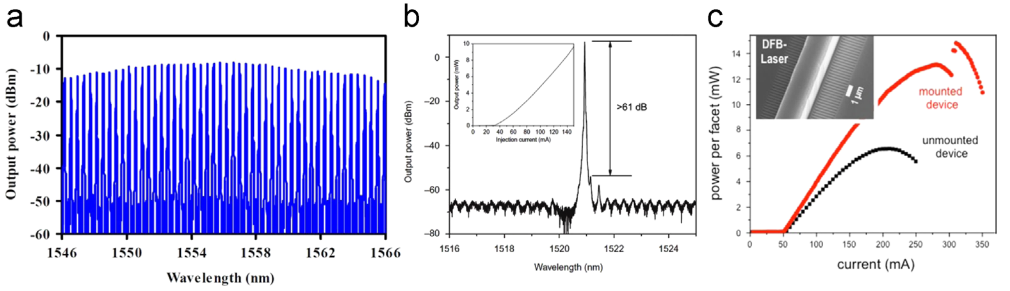


Fig. 21. (a) The optical spectra of over 46 channels InAs/InGaAsP/InP Qdots multiwavelength laser with 50 GHz frequency spacing and within the 3 dB bandwidth at an injection current of 200 mA. (b) Lasing spectrum of single mode InAs/InGaAsP/InP Qdots DFB laser at an injection current of 200 mA and at room temperature. Inset shows the corresponding *L–I* curve of the ridge-waveguide InAs/InP DFB laser operating in CW at room temperature. (c) *L–I* curve of an un-mounted and mounted InAs/InGaAlAs/InP Qdots DFB laser. The inset shows a scanning electron microscopy (SEM) picture of the lateral first order grating before planarization and contact metallization. Taken from [136,138,139].

cavity length. Such devices are highly attractive in optical networks replacing many individual lasers. This concept was first reported by Liu et al. [134] on InAs/InP Qdots material system. By employing a $2 \times 4500\ \mu m^2$ ridge-waveguide InAs/InGaAsP/(100)-InP Qdots laser and in CW operation, 93 uniform channels (centered at 1.642 μm) with channel intensity non-uniformity of 3 dB was reported. The channel spacing was estimated to be 86 pm (9.56 GHz) with $\sim$30 μW output power from each channel. It was suggested that the non-trivial channel spacing alteration due to intracavity waveguide dispersion (alteration in temperature, effective current injection, and vacuum wavelength) of $\pm 0.8$ pm could be corrected by designing the dispersion of ridge-waveguides. In a subsequent study, Liu et al. [135] estimated the linear intracavity waveguide dispersion of $-5.1 \times 10^{-4}\ nm^{-1}$ from a $2 \times 461\ \mu m^2$ ridge-waveguide laser with 24 channels. The channel spacing and maximum signal-to-noise ratio was 0.8 nm (91.6 GHz) and 62 dB, respectively. Very recently, Lu et al. [136] developed a 50 GHz spacing C-band (central wavelength 1.555 μm) multiwavelength laser using a $3 \times 860\ \mu m^2$ ridge-waveguide InAs/InP Qdot active region device with an average output power of 40 mW that matches the International Telecommunication Union (ITU) grid, as shown in Fig. 21(a). The relative intensity noise (RIN) of individual channel which describes the laser's maximum available amplitude range for signal modulation, was measured to be $\sim -118$ dB/Hz [69].

### *3.1.4. Single mode lasers*

Single mode lasers are the opposite extreme to the broad gain multiwavelength lasers, and forms the backbone of the long haul optical communications. The first single mode InAs/InP Qdots laser diode was demonstrated by Kim et al. [137] on InAs/InGaAlAs material system and using distributed-feedback (DFB) configuration. The room temperature lasing emission of $3 \times 1000\ \mu m^2$ ridge-waveguide device was 1.564 μm with side mode suppression ratio (SMSR) of 42 dB at 100 mA CW current injection. However, the output power of the device was low reaching a value of 1 mW at 100 mA and a red shift in the Qdot lasing emission was observed compared to the Qdot lasing wavelength without the gratings. This required tuning of the Qdots emission by reducing the amount of InAs deposition for the Qdot self-assembled formation. On the other hand, Lu et al. [138] reported a InAs/InGaAsP/(100)-InP Qdots DFB laser fabricated using the commercial buried grating process. After the growth of the active region using CBE system, the wafer was removed to pattern the grating region and then the p-contact layers were regrown using MOCVD system. No change in the PL emission was observed before and after grating overgrowth. The fabricated $3\times1000\ \mu m^2$ ridge-waveguide DFB laser demonstrated a lasing threshold of 48 mA with output power up to 19 mW at 200 mA CW operation up to 90 °C. The lasing wavelength was 1.52 μm with SMSR of >61 dB and is depicted in Fig. 21(b). The measured RIN and optical linewidth was around <−154 dB/Hz (10 MHz–10 GHz) and 150 kHz, respectively.

Recently, Reithmaier et al. [139] modified the InAs/InGaAlAs/(100)-InP Qdots layer design by integrating a InGaAsP etch stop layer which allowed fabrication of the lateral gratings after ridge-waveguide processing. An output power of >12 mW in CW operation, lasing at ~1.52 μm with SMSR of 45–50 dB was reported from the $2\times1000\ \mu m^2$ device at room temperature. The results are shown in Fig. 21(c). The optical linewidth in this case was measured to be ~149 kHz, however, due to internal heating, the lasing wavelength shifted with increasing current injection.

### *3.2. InAs/InP Qdots mode-locked lasers*

Mode synchronization in FP lasers could emit very short pulses with the repetition rate determined by the round trip tracing of the cavity. This concept of mode locking in laser devices could be key components in optical clocking, optical communications, etc. Moreover, monolithic passive mode locking device is highly attractive because of its compactness, stability and straightforward fabrication process. In this case, two-section devices are usually employed with one section being forward bias which forms an optical amplifier, and the other is reversed bias which forms a saturable absorber (SA) section and assists in achieving the mode synchronization condition [2]. Since, self-assembled Qdots possess broad gain due to inhomogeneous broadening; the requirement of mode synchronization could be easily fulfilled from the same array of Qdots (some Qdots act as absorbers while others contribute to gain) in a mono-section device known as self-pulsating devices [2]. Here, we reviewed the achievements of mode locking in InAs/InP Qdots laser utilizing both of these configurations.

#### *3.2.1. Two section*

Heck et al. [140] reported the first investigation of mode-locking characteristics from two section InAs/InGaAsP Qdots laser on (100) InP. The long $2\times9000\ \mu m^2$ ridge-waveguide device with 270 μm SA section showed a threshold current of 660–690 mA and demonstrated a clear mode locking characteristics with strong peaks in the radio-frequency (RF) spectrum at a repetition rate of 4.6 GHz (round trip cavity frequency) and peak width of 0.57 MHz at −20 dB, as shown in Fig. 22(a). The pulse duration was measured to be around 6–11 ps. On the other hand, the smaller device ($2\times7000\ \mu m^2$ ridge-waveguide with 350 μm SA section) did not show the signs of model-locking but instead showed Q-switching at three regimes 32.5, 153, and 390 MHz, with increasing injection, as depicted in Fig. 22(b). The pulse duration was 0.6–0.8 ps. A reverse bias of −1 V and −3 V were applied to long and short devices, respectively. Subsequently, the timing jitter was evaluated for the long device with a value 35–39 ps and the effect of longer SA of 540 μm was also investigated [141]. It was found that mode locking was achieved at relatively high values of injection current and higher timing jitter 36–53 ps, with output power, in the regime of stable mode locking, in between 1–4 mW. Moreover, from a $2\times4000\ \mu m^2$ ridge-waveguide with 120 and 240 μm SA, stable passive mode-locking was observed for a smaller regime with pulse repetition rate of 10.5 GHz corresponding to the 95 ps cavity round trip. The RF peak width was in the order to 0.5–2.5 MHz at −20 dB. The effect of

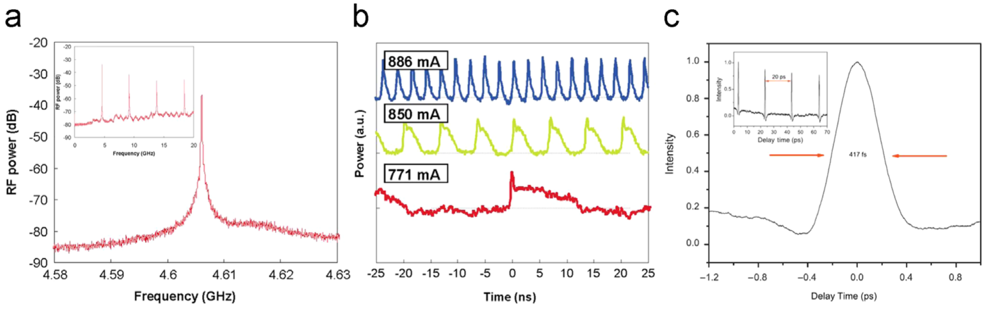


Fig. 22. (a) Detailed view of the spectrum around the first RF peak obtained for a 9 mm device with 3% SA length. Injection current is 900 mA and SA bias voltage is −1 V. Inset shows the RF-spectrum. (a) Oscilloscope traces obtained for different injection currents corresponding to the three different regimes of Q-switching obtained with a 7 mm device with 5% SA length and an SA bias voltage of −3 V. Traces have been offset for clarity, *i.e.* the dotted lines represent the respective 0-levels. (c) Optical intensity autocorrelation trace with second-order autocorrelation measurements. Assuming a Gaussian pulse shape, the real pulse duration of the $2.5 \times 861\ \mu m^2$ InAs/InP Qdots mode-locked laser was estimated at 295 fs when the injection current is 200 mA and at a temperature of 18 °C. Inset shows the optical intensity autocorrelation pulse trains with the periodic time of 2 ps, which corresponds to a repetition rate of 50 GHz. Courtesy from [11,140,144].

simultaneous lasing from ground state and excited state in the short cavity laser on mode locking characteristics was also studied by Heck et al. [141]. It was found that not only mode-locking of both the mode groups was observed but also their pulses were synchronized. A similar mode-locking characteristic was also observed by Tahvili et al. [142] in a dual-wavelength mode-locked laser, which corresponds to lasing emission from the same electronic transition of a $2 \times 4000\ \mu m^2$ two-section device. In addition, employing a long 13 mm device (650 μm long SA), a stable mode locking of 3 GHz was also demonstrated which is the lowest repetition rate reported for a monolithic InAs/InP Qdots laser.

Recently, hybrid mode-locking in two section InAs/InGaAsP/(100)-InP Qdots laser was investigated [142,143]. In this case an electrical modulation, with frequency close to the cavity free-spectral range, is added to a reversely biased SA. Employing a 9000 μm two-section device, it was shown that the timing jitter strongly decreased to 0.5–0.6 ps (10 kHz–300 MHz) and via second order dispersion of single mode fiber, pulse compression down to 2 ps was obtained at 4.6 GHz pulse frequency. In the case of 13 mm device, the timing jitter reduced from 8–16 ps (passive mode-locking) to 0.7–3 ps (hybrid mode-locking).

### *3.2.2. Self-pulsation*

Monosection or single-section mode-locking was first demonstrated by Renaudier et al. [120] on InAs/InP Qdots/Qdash active region laser. Self-pulsation at 45 GHz under CW operation was observed from a 950 μm device which is equivalent to the round trip cavity time. From the mode beating spectra, the pulse width was measured to be 70 kHz at −3 dB, operating at 160 mA. Active mode-locking with an optical clock signal at 45.06 GHz was also reported with a significant decrease in the RF spectral linewidth to 3 KHz (determined by the chosen resolution bandwidth) and extremely low timing jitter of 82 fs. This work was soon followed up with the demonstration of 92 GHz repetition rate with femtosecond pulses from passive-single section CBE grown $2.5 \times 456\ \mu m^2$ InAs/InGaAsP Qdot laser on (100) InP, lasing at ~1.54 μm (C-Band), by Lu et al. [145] and dual-wavelength self-mode locking at 92.5 GHz by Liu et al. [146]. In the former case, the laser showed a threshold current of 17.2 mA under CW operation with output power ~9 mW at 45 mA. Moreover, through autocorrelation measurements, periodic time of the measured pulse train was 10.87 ps (92 GHz) with 312 fs pulse width (after removing the DC components from 442 fs autocorrelation trace and converting to real pulse duration), at 45 mA. This self-pulsation characteristic from Qdot active media was attributed to strong self-phase and cross-phase modulation effects leading to significant enhancement in the four wave mixing (FWM) process between the longitudinal laser modes of the FP laser cavity. Subsequently, an L-band ($\sim$1.59 μm) mono-section InAs/InP Qdots mode-locked laser was reported with a $3 \times 930$ μm$^2$ (with one facet high reflection coated) device exhibiting 46 GHz RF resonance peak with linewidth $<$100 kHz and optical signal-to-noise-ratio $>$20 dB [147]. The measured autocorrelation pulsed width was 629 fs which after conversion to real pulse width was 445 fs. The time bandwidth product of this device was 0.69 which was larger than the transform-limited Gaussian-shaped pulses of 0.44 and was attributed to residual frequency chirp being present in the pulses. With continues improvements in the Qdots active region design, material quality, and fabrication, Lu et al. reported a real pulse duration of 295 fs from $2.5 \times 861$ μm$^2$ laser device at a repetition rate of 50 GHz and lasing around $\sim$1.56 μm with an output power of 40 mW at 200 mA. The results are shown in Fig. 22(c). This is the smallest pulse width value reported on InAs/InP Qdots material system [11,144] without any external means. In addition, achievement of repetition rates as low as 10 GHz and as high as 100 GHz from $2.5 \times 430$ μm$^2$ and $2.5 \times 4300$ μm$^2$ Qdot mode-locked lasers, respectively, highlights the achievements of InAs/InP Qdot active media in mode locking. Very recently, apart from the leading (100)InP based Qdot mode-locked lasers, self-pulsation in InAs/InGaAsP Qdots lasers on (311)B InP substrate was also reported by Klaime et al. [106] with repetition rates around 23 and 39 GHz and pulse width down to 1.5 ps. The $2 \times 1000$ μm$^2$ and $2 \times 2000$ μm$^2$ ridge-waveguide devices exhibited extremely low RF spectral width of 20 kHz indicating very low timing jitter.

Through changing the inherent active length of the FP cavity to external cavities coupled with fiber Bragg gratings (FBG), Lu et al. [11] was able to generate a pulse repetition rate of 437 GHz, thus removing the barrier which limits the realization of very high repetition rates (due to cavity length dependence) mode locking. In this case, eight FBG with equal frequency spacing were utilized to form the external fiber mixed cavity with $2.5 \times 861$ μm$^2$ InAs/InGaAsP/(100)-InP Qdots laser with one fact high reflection coated and other anti-reflection coated. The working principle was based on the reflection of those longitudinal modes which matches the wavelength of FBG, by the external cavity, thus increasing their intensities compared to other longitudinal modes of the laser itself ($-40$ to $-10$ dBm higher and equally spaced). By using an autocorrelator, a pulse train of 2.29 ps duration (810 fs real width) was measured at 437 GHz, with an average output power of 1 mW. This work was further improved by demonstration of 403 GHz pulse repetition rate with a pulse width of 268fs at 110 mA and 563 fs at 112 mA CW current injection from a similar FBG based external cavity configuration and utilizing $3 \times 850$ μm$^2$ Qdot laser device (with free spectral range 50.25 GHz) in the C-band [148]. This is illustrated in Fig. 23(a) and (b) and was attributed to the FWM between the strong light peaks of the optical spectrum (obtained in external cavity configuration) and leading to mode-locking.

The accomplishment of coupled external cavity InAs/InP Qdots laser based mode locking was brought to the next level by the demonstration of pulse repetition rates in terahertz range by selection of inter frequency spacing of FBG in the terahertz since this spacing determines the repetition rate. A $3 \times 1000$ μm$^2$ InAs/InP Qdot laser with one facet 95% high reflectivity and other 31% reflectivity was utilized with a FBG central wavelengths corresponding to 1.01 THz [10]. It was shown that at low CW bias current below 48 mA, the coupled cavity modes lased with dominant wavelength peaks defined by the three FBG wavelengths. The resulting pulsed train measured with autocorrelator showed pulsed repetition rate of 1.0 THz with pulse duration

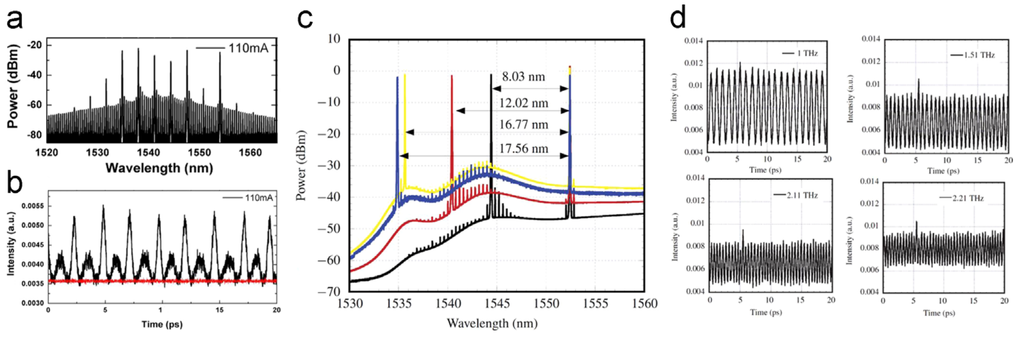


Fig. 23. (a) Measured optical spectrum of the InAs/InP Qdots mode-locked laser with the external cavities of eight FBGs, at the biased current of 110 mA. Optical resolution used is 10 pm. (b) Measured autocorrelations of the pulse train indicating a period of 2.48 ps, which corresponds to a repetition rate of 403 GHz at the biased current of 110 mA. The red line indicates noise level of the autocorrelator. The intensity autocorrelation is measured based on second-harmonic generation with a time resolution of 10 fs. (c) Tunable dual-mode spectra of InAs/InP Qdots laser with external cavities of three FBGs, from 1 to 2.21 THz at the biased current of 120 mA and temperature controlled at 18 °C. The mode separations are indicated in the spectrum. (d) Tunable beating frequencies from 1 to 2.21 THz in the time domain corresponding to the four mode-separations in (c). Taken from [148,149]. (For interpretation of the references to color in this figure legend, the reader is referred to the web version of this article.)

of 500 fs. However, with increasing bias the envelope of 1.01 THz pulse train got modulated at 43.8 GHz equal to the mode spacing of the Qdots laser itself which dominated with further increase in bias current. Modifying the external coupled cavity Qdots laser configuration by employing two FBG configurations with one FBG tunable in wavelength, Jiao et al. demonstrated a tunable 1 to 2.21 THz ultra-high repetition rate mode-locked laser; the highest repetition rate reported on a InAs/InP Qdots material system [149]. This is illustrated in Fig. 23(c) by plotting the mode spectra and in Fig. 23(d) by showing the corresponding pulse widths variation from 158 fs (at 2.11 THz) to 315 fs (at 1.0 THz). These are the record pulse width values ever reported on InAs/InP Qdots material system. Mode locking via external cavity configuration seems to be a promising technique in achieving extremely high repetition rates which is FBG dependent rather than Qdots laser except that the gain and carrier dynamics of the active media should be fast enough to sustain successive pulse emission.

### *3.3. InAs/InP Qdots semiconductor optical amplifiers*

Long wavelength SOA based on InAs/InP Qdots active region has shown remarkable improvement in terms of performance characteristics compared to the Qwell based SOA [150–152], particularly broadband gain profile. This is attributed to the inhomogeneously broadened Qdots gain and the ultra-fast carrier capture process [153]. In the subsequent sub-sections, we review the recent achievements of InAs/InP Qdot based SOA component operating around $\sim 1.55\ \mu m$ and encompassing C–L–U communication bands of the ITU grid.

#### *3.3.1. Broad Gain*

Akiyama et al. [154,155] demonstrated an InAs/InGaAsP on (100) InP MOCVD grown Qdots SOA with more than 25 dB gain over 90 nm bandwidth and noise figure (NF) $<5$ dB which is the degradation of the signal due to amplified-spontaneous emission noise. The saturated output power of this $2.2 \times 6150\ \mu m^2$ long device was measured to be $>19$ dBm within the bandwidth.

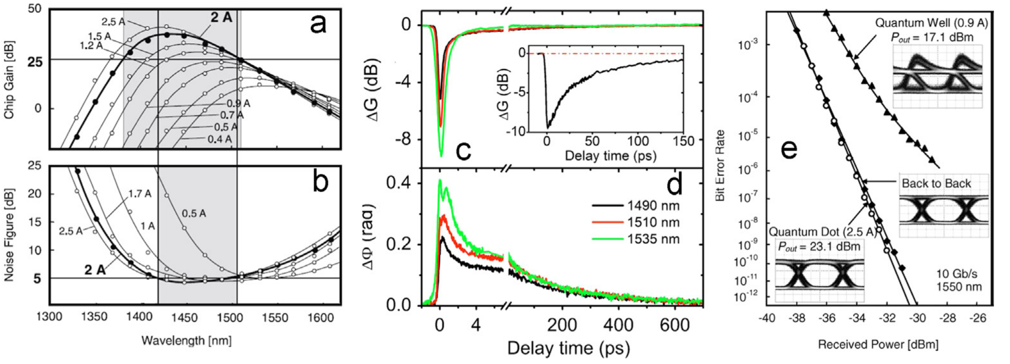

Fig. 24. Wavelength dependence of (a) gain and (b) NF, as a function of wavelength for the InAs/InGaAsP Qdots SOA. Pump and probe measurements of the (c) gain and (d) phase recovery curves at 1.535 μm (GS) and 1.510 and 1.490 μm (ES) under an applied current of 300 mA for the InAs/InP Qdots SOA. Inset shows the gain recovery curve of a commercial SOA composed of a bulk active material. (e) Bit error rate (BER) and eye diagrams of the InAs/InP Qdots SOA. Reproduced from [167,168].

Such an impressive results, which are summarized in Fig. 24(a) and (b), has not been achieved by the Qwell couparts thus making InAs/InP Qdots SOA highly attractive in this domain. The polarization dependence of the gain was eliminated by growing closely stacked columnar Qdots, thus favouring vertical coupling and leading to polarization insesitive SOA gain characteristics [156]. This work was soon followed by various deomstrations of the gain characteritics of InAs/InP Qdots SOA [157,158]. For instance Kim et al. [159] showed a chip gain as high as 37 dB and maximum saturation output power 17.2 dBm at 950 mA from $3 \times 3000\ \mu m^2$ long device after determining the coupling-loss (14.4 dB) and performing the fiber-to-fiber gain (22.5 dB) measurements. The gain peak was found to be at ~1.51 μm with a NF of 7.2–9 dB. Contestabile et al. [160] obtained fiber-to-fiber peak gain of 37 dB at 1.49 μm with 3 dB bandiwdth of 75 nm. A maximum output saturation power measured was around 18.5 dBm. These impressive values are attributed, in general, to the spatially distributed Qdots optical tranistions, ultra-short gain recovery time (discussed later in this section), and small optical confinement factor [69].

### *3.3.2. Ultrafast gain and index dynamics*

Ultrafast gain response, which is in the order ot few picoseconds, is the characteristics property of Qdots, also observed in InAs/GaAs Qdots material system [161,162]. This is a property wherein remaining electrons from the surrounding material are supplied to the Qdots whose electroncs are extracted *via* stimulated emission triggered by the incident singal. Thus, the saturated gain (hole burning) in these Qdots which are resonant with the wavelength of the incident signal and the surrounding material which is unidque to Qdots helps in realizing an ultrafast gain recovery [154,163]. Employing strong 150 fs resolution pump-probe experimentts, Zilkie et al. [164] measured a 15 ps long-lived and 1–2 ps short-lived gain recovery time in InAs/InGaAsP Qdots SOA on (100) InP and attributed, in general, to the phonon-mediated carrier capture into Qdots, and slow 400 ps absorption decay time due probably to the slow spontaneous carrier recombination, or carrier escape from the Qdots. Morevoer, comparison of Qdot, Qdash, and Qwell SOA behavior showed the gain recovery times to be fastest for dots (approximately 4–6 times smaller than Qwell) with the phase response following the same time scale as the gain recovery [165] indicative of small SOA linewidth enhanceent factor, and was confirmed by reporting values around 2–10 [166] with increasing current njection. In another study, Park et al.

[167] performed similar pump-probe experiments to shed light on the contributions of GS and ES to the gain recovery time. It was shown, as depicted in Fig. 24(c) and (d), that for the GS wavelength, an ultrafast gain recovery time ~0.7–2 ps was extracted; however, at higher energy levels corresponding to the ES, the extracted gain recoevery time increased to 30 ps. Due to the peculiar nature, a three-step exponential fit was performed by Contestabile et al. [160] on the cross gain modulation signal obtained with a 0 dB CW signal at 1.55 μm and 3 dBm mean power (13 dBm peak power) for the 10 GHz signal at 1.54 μm, to extract the gain recovery time. It was shown that around 85% of the gain recovery was achieved in only 10 ps and complete gain saturation (100% recovery) in ~30 ps.

### 3.3.3. High speed amplification and signal processing

The ability to achieve fast gain response to spectral hole burning, high output power and low noise, and the broad gain bandwidth of Qdots SOAs offered a variety of promising applications suh as aimplifiers, wavelength convertors, switches and regeneratores, in the optical network [168]. Here we review some of these achievments with regards to the InAs/InP Qdots SOA.

The high speed gain response to 10–40 GHz signal intensity change was discussed in the previous section [154] with achieved gain of >25 dB and <5 dB NF. Similarly, the results of pump-probe experiments in femtosecond resolution with gain recovery ~2–15 ps showed the potential of Qdots SOA for near 100 GHz switching speed at 1.55 μm. The ability to operate with hgih speed input signals (40 Gbps) with minimum signal distortion in the gain sauration regime (pattern effect) was demonstrated upto an output power of 22.8 dBm (zero error free power penalty for upto 23.1 dBm output power) which is 8 dB superior compared to the Qwell SOA counterparts. Fig. 24(e) shows the bit error rate (BER) and eye diagrams of the Qdots SOA and Qwell SOA demonstrating superior preformance of Qdots device. In addition, Sugawara et al. [168] also demonstrated the Q-factor improvement of 40 Gbps PRBS non-return-to-zero (NRZ) signal degraded by adding the amplified spontaneous emsission. The corresponding input and output signal eye diagrams were remarkably similar thus affirming Qdots SOA as a potenetial optical regenerator. The regenerating capability of the InAs/InP Qdots SOA was attributed to '1'–level noise supression by driving the amplifier into gain saturation which could not be realized in Qwell SOA due to pattern effects. Furthermore, Contestabile et al. [169] reported utilization of Qdot SOA for regenerative amplification of 10, 20, and 40 Gbps return-to-zero (RZ) signals by a simple scheme exploiting self phase modulation with a detuned filter and working at low input power and with a large input dynamic range. The effect of high speed amplification of 10 Gbps NRZ signal by Park et al. [170] revealed no singal distortion (pattern effects) at any applied current under GS operation of InAs/InP Qdots SOA, inline with the measured ultrafast gain recovery time. However, the slower gain recoevery componenet of the ES significantly deteorated the amplified output signal with patten effects when operated under ES.

InAs/InP Qdots SOA function as wavelength converstor was also reported recently utilizing two main non linear processes *viz.* FWM [171–173] and cross gain modulation [174]. In the former case, a symmetric FWM efficiency between positive and negative detuning was observed by Lu et al. [171], and the efficiency decreased by <20 dB/decade with frequency detuning increased. A 40 ps pulse train with repetition rate 500 MHz was successufly detuned ut po 6.2 nm from the CW pump. By using low power single pump FWM, Contestabile et al. [172] reported a 30 nm conversion span with $>-10$ dB conversion efficiency and output optical signal-to-noise ratio >20 dB. Transparency to coherent modulations was also demonstrated in a 25 nm conversion of 10 GBaud quadrature phase shift keying (QPSK), 8-phase shift keying

(PSK) and 16-quadrature amplitude modulation (QAM) signals. Very recently, utilizing double pump FWM process, an ultra-broadband spanning 100 nm and efficient wavelength conversion (positive conversion efficiency $>30$ dB output optical signal-to-noise-ratio) was reported in the telecommunication band around 1.55 μm [173]. In the latter case of cross gain modulation, employing InAs/InGaAsP Qdot SOA on (100) InP, an efficient distortion free wavelength conversion on detuning of $\sim 12$ nm was achieved for frequencies upto 40 Gbps [174]. For frequencies 80 and 160 Gbps, a slightly detuned output filter was utilized to obtain pattern-effects free wavelength conversion via cross-phase-modulation. Moreover, with a 80 Gbps signal format conversion of output inverse-RZ to RZ was also demonstrated.

### *3.4. InAs/InP Qdots superluminescent diodes*

Long wavelength SLD working in the C–band are highly attractive in optical measurement and instrumentation, OCT, etc., besides optical communications, as has been discussed in section 1. In the case of InAs/InP Qdots based active region, by exploiting the inhomogeneous broadening via modulated stacking of the self-assembled InAs Qdots on strain reducing InGaAlAs layer on (311)B InP substrate, Akahane et al. [175] reported a room temperature ultra-broadband SLD operating under pulsed operation. By varying the amount of InAs deposition among the Qdots stacks and the thickness of the buffer/spacer layer (chirped design), a 36-stack device structure was grown using MBE with Qdot density $7.1 \times 10^{10}$ cm$^{-2}$. The 50 μm wide device under pulsed operation demonstrated an electrolumenescence bandwidth of 213 nm at 100 mA centered at around 1.53 μm. A maximum bandiwdth of 217 nm was achieved at 3 A, and the measured coherence length using Michelson interferrometer was 6.5 μm which is impressive and probably the best value reported in literature around this wavelength.

## 4. InAs Qdashes grown on InP

The word “quantum dash” was introduced in late 1990's by Utzemier et al. [176] and Guo et al. [177] who reported self-assembled InSb Qdashes on (100) InP and InAs Qdashes on (211) B GaAs substrates, respectively. The Qdashes were elongated along [110] direction in the former case and [1–10] direction in the latter case with typical dimensions $\sim 18$ nm $\times$ 60 nm $\times$ 140 nm. It was until early 2000's that this class of quantum confined nanostructure key features were identified and exploited in the demonstration of various optoelectronic devices. In this section, we reviewed the Qdash growth on (100) InP substrate starting from the self-assembled quantum-wire (Qwire) growth because this work laid the foundation for eventual Qdash growth technology. This nanostructure was also dominated by two material system (i) InAs/InGaAlAs and (ii) InAs/InGaAsP, similar to that of the InAs/InP Qdot case discussed in Sections 2 and 3.

### *4.1. InAs/InGaAlAs Material System*

#### *4.1.1. Qdashes on (100) InP substrate*

Research interest in the MBE growth of self-organized InAs Qwires or wire-like nanostructures on (100) InP substrate started in late 1990's with initial demonstrations by Brault et al. [23] and Li et al. [28] on InAlAs buffer layers. In the latter case, high density wire-like nanostructures, shown in Fig. 25 (a), were observed from the 6-stack InAs/$Al_{0.48}In_{0.52}As$ Qdashes ($\sim$70/μm) and ascribed to the surface anisotropy due to As-dimer reconstruction. Moreover, linearly polarized light based 15 K PL measurements revealed peak PL wavelength at

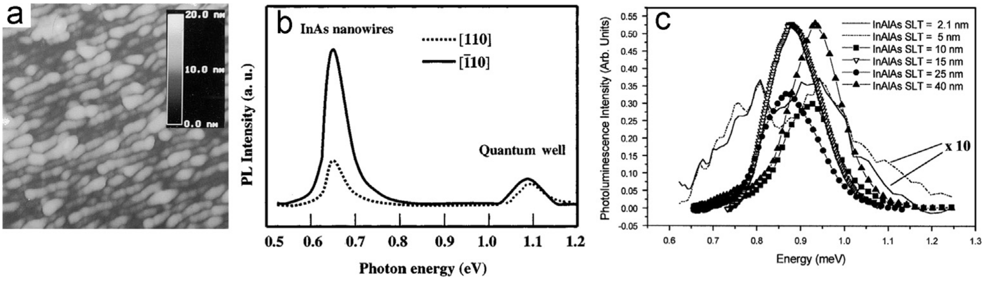


Fig. 25. (a) AFM image of ($1\times1\ \mu m^2$) InAs surface morphology with 7.5 ML deposition thickness on $Al_{0.48}In_{0.52}As$ showing the growth anisotropy. (b) 15 K polarized PL spectra of the multilayer sample with 6 stack InAs ~6.5 ML/ $Al_{0.48}In_{0.52}As$ ~20 nm. The incident laser beam was polarized in the [110] or [−110] direction. (c) Comparison of 300 K PL spectra of 5-stack InAs layer samples with different spacer layer thickness (SLT). Collected from [28,178,179].

~1.9 μm and the wires exhibited large anisotropy for [1–10] and [110] polarization with peak PL intensity ratio of 3, as depicted in Fig. 25(b). Subsequently, Li et al. found via TEM characterization on a single stack $InAs/Al_{0.48}In_{0.52}As$ Qwire structure that increasing the amount of InAs deposition from 1.5–7.5 ML resulted in more inhomogeneous and large size Qwire formation [178]. This work was soon followed by a thorough investigation of the effect of AlInAs spacer/buffer layer thickness in a multi-stack Qwire structure on its optical characteristics by Brault et al. [179]. A fixed 5-stack Qwire sample with 3 ML InAs deposition thickness and 120 s growth interruption was employed in the study, and varying the AlInAs thickness from 5 nm to 40 nm. For < 10 nm spacer layer thickness (SLT), a highly dispersive Qwire formation with no vertical self-organization of the Qwire layers was observed and verified by large room temperature PL linewidth of ~300 meV centered at ~1.77 μm, as illustrated in Fig. 25(c). A strong staggered Qwire vertical arrangement was found for 10–25 nm SLT with increase in the Qwire size and reduction in PL linewidth to ~130 meV, while no correlation was observed between the SLT and Qwire formation beyond 25 nm which suggested no influence of dash layer on each other. These observations were attributed to the complex interdependence between phase separation, surface morphology, and mismatched stresses [179] within the structure.

Next, Wang et al. [3] reported the first dash-in-a-well (DaWELL) laser structure on (100) InP substrate by growing InAs Qdashes within an asymmetric compressively strained InGaAlAs Qwell separated by InGaAlAs tensile strained barrier layers. A Qdash density ~$10^{10}$ $cm^{-2}$ with typical Qdash dimensions of ~5 nm × 25 nm × 300 nm was reported, via AFM study. Room temperature PL peak emission was observed at ~1.57 μm and linewidth ~75 meV (~140 nm). Following this work, Schwertberger et al. [180] performed a systematic study of different MBE growth parameters influencing InAs Qdash formation on InGaAlAs buffer layer on (100) InP substrate. By fixing the substrate temperature and increasing the InAs deposition thickness from 2.5 ML to 7 ML drastically affected the Qdash morphology with decreasing Qdash length and increasing Qdash height. For instance, SEM image of 5 ML InAs deposition thickness Qdashes is shown in Fig. 26(a). On further increase in InAs thickness, single Qdashes coalesce to form larger islands of the material with reduced Qdash like nature. This study was further supported by PL results at 8 K from these samples as depicted in Fig. 26(b). A clear red shift in the PL peak emission from 1.2 μm (0.4 nm) to 2.0 μm (10 ML, 3.1 nm) was observed on increasing the InAs deposition thickness [181]. Furthermore, the effect of substrate temperature on the Qdash growth was examined Schwertberger et al. and suggested an ideal growth temperature around 500 °C which showed maximum PL intensity without any change in the PL peak position. Any

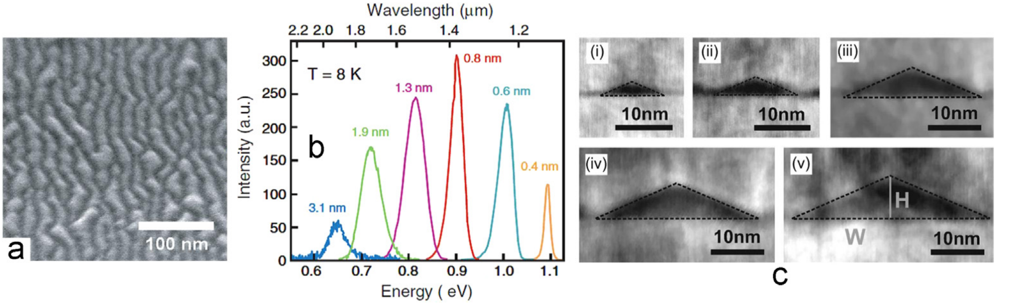


Fig. 26. (a) SEM image of the top view of an uncapped InAs Qdash sample with 5.0 ML InAs grown on InGaAlAs buffer layer on (100) InP substrate. (b) Low temperature PL spectra of Qdash layers with different nominal InAs layer thickness as indicated in the figure, on InGaAlAs buffer layer on (100) InP substrate. (c) Cross-sectional bright-field TEM micrographs of the InAs Qdash samples with InAs nominal thicknesses of 0.8, 1.2, 1.6, 2.4, and 3.1 nm for samples (i), (ii), (iii), (iv), and (v), respectively, on InGaAlAs buffer layer. The parameters '*H*' and '*W*' in (v) correspond to the Qdash height and width. Adapted from [26,183].

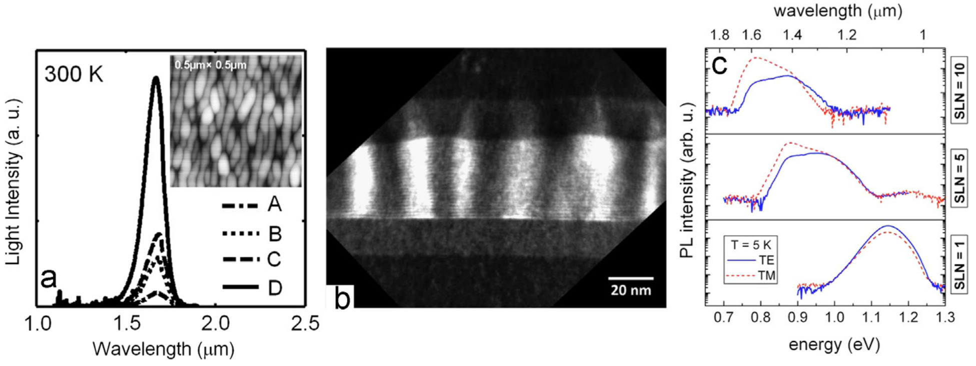


Fig. 27. (a) PL spectra measured at 300 K for four InAs Qdash samples grown at various conditions (A and B with InGaAlAs barrier grown at 505 °C and 535 °C, respectively. C and D are similar to B except an ultra-thin GaAs layer was grown before the growth of InAs layer, and before and after the growth of InAs layer, respectively). Inset shows the ($0.5 \times 0.5\ \mu m^2$) AFM image of an InAs Qdash layer without InAlGaAs cap. (b) Cross-sectional TEM micrograph of InAs/GaAs columnar Qdashes with 24 stacking layers. The intersection was made in [110] direction, *i.e.*, perpendicular to the longer lateral size of the Qdashes. (c) Polarization resolved low temperature PL from the cleaved edge perpendicular to the columnar Qdashes' longer lateral size. Stacking layer number (SLN) is equal 1, 5, and 10, where SLN = 1 corresponds to the structure with standard Qdashes. Courtesy of [186,187].

temperatures higher than 500 °C was not realized due to increased In desorption during Qdash growth. In another study, Stintz et al. [38] also reported similar results on the effect of InAs coverage (8–23 Å) on the Qwire formation on InGaAlAs and InGaAs buffer layers ascribing the asymmetric nanostructure formation to the anisotropy of strain relaxation, difference in surface mobility and diffusion length with direction. However, beyond these InAs coverage the directional dash preference was observed to decrease with almost no evidence of dot-like structures at 23 Å InAs deposition, and the PL measurements suggested large misfit dislocations in these Qdots as no light emission was observed. Furthermore, by room temperature PL measurements on DaWELL samples with Qdashes embedded in InGaAlAs and InGaAs Qwell, surrounded by InGaAlAs barrier layers, Rotter et al. showed a huge red shift with respective PL peak emission at 1.52 μm to 2.04 μm; a notable demonstration of the tunability of Qdash emission by the surrounding Qwell layers and InAs coverage [182].

Next, Sauerwald et al. [183] demonstrated, via chemically sensitive scanning TEM and PL measurements, that by adjusting a single growth parameter *i.e.* InAs deposition thickness, the Qdash emission can be controlled between 1.37 and 1.9 μm without modifying its shape and composition. By MBE growth of single stack InAs/InGaAlAs Qdash samples on (100) InP substrate at various InAs coverage (0.8, 1.2, 1.6, 2.4, and 3.1 nm), they showed that Qdashes maintained a constant height-to-width ratio within the sample and among the samples, as shown in Fig. 26(c). Moreover, the Qdash height and width increased linearly (*i.e.* Qdash size) with increasing nominal InAs layer thickness, thus red shifting the PL peak wavelength and broadening the PL linewidth. No significant intermixing of Qdash and the embedding material was observed, and the PL shift was attributed to the change in Qdash size (smaller dashes with higher energy quantization shifted to higher energies) [184]. In addition to the growth kinetics, surface and strain energies also played an important role in the Qdash formation and hence this observation was also related to the significant reordering of the material during the whole growth of the InAs layer. This work of single stack Qdash was further extended to a multi-stack Qdash structure with the objective of examining the impact of vertical stacking on the size and composition of Qdashes [185]. By growing 4-stack InAs/InGaAlAs DaWELL structure in three samples, each with different InAs layer thickness (1.1 nm, 1.5 nm, and 2.1 nm), it was shown that the Qdash size increased with subsequent stacking of layers. This effect was found to increase with nominal InAs layer thickness and was ascribed to the strain effects that caused the merging of Qdashes in the upper layers and hence increase in size leading to larger inhomogeneity in the DaWELL structure.

In order to improve the inhomogeneous broadening of Qdash multi-stack structure, the concept of growing ultrathin ($\sim$2 ML) GaAs layer on InGaAlAs barrier layer before InAs deposition for the Qdash formation was reported by Mi et al. [186] who demonstrated an improvement in the optical quality ($>$ 3 times increase in the PL intensity) as illustrated in Fig. 27(a) and is coherent with other reports [36]. A dramatic enhancement ($>$ 10 times) in PL intensity with reduced PL linewidth of $\sim$50 meV at room temperature was observed if additional GaAs layers were deposited after the growth of 5 nm InGaAlAs capping layer. This was attributed to the suppressed phase separation and enhanced surface migration in the barrier layer. A PL peak wavelength of $\sim$1.7 μm and Qdash density of $\sim 2\times10^{10}$ cm$^{-2}$ was reported. Furthermore, modulation p-doping the active region (barriers) and tunnel injection schemes were also investigated on the multi-stack Qdash structures without affecting the Qdash quality [188]. Very recently, Podemski et al. [187] reported the growth of highly stacked columnar Qdashes on (100) InP. The nominal thickness of the Qdash layers were $\sim$0.7 nm (just above the critical thickness of Qdash formation) with $\sim$1.0 nm GaAs spacer layer, and hence formation of thin dashes, as shown in TEM image of Fig. 27(b). The Qdash layers were then sandwiched between InGaAlAs layers and finally with InAlAs buffer layers. It was shown that by controlling the number of stacking layers (SLN) from 1 to 24, a transition of the dominant polarization from transverse electric to transverse magnetic could be realized which is highly attractive for polarization independent SOA. Besides, plotted in Fig. 27(c), a red shift in the PL peak emission was observed on increasing the number of Qdash layers (from $\sim$1.1 μm to $\sim$1.6 μm). In general, these findings were attributed to the increase in Qdash vertical dimensions when PL intensity from the cleaved facet edge perpendicular to the columnar dashes longer lateral size was acquired. However, emission from the other edge (parallel to the Qdashes' longer lateral size) did not show any dependence of polarization on the dash height since the polarization was driven by the dashes longer lateral size rather than height [189]. A more detailed and systematic investigation of the Qdash height on the polarization of the surface emission was carried out by Musial et al. [190] who showed through surface PL emission from these dashes was primarily driven by Qdash height due to heavy hole and light hole mixing.

#### 4.1.2. Qdash Optical Properties

Ukhanov et al. observed anisotropy in modal gain which was due to the polarization dependence of the transition matrix element in the Qdash nanostructures [191]. The experimental measurements of gain, differential gain, and LEF showed a strong Qdashes-orientation dependence in the laser cavity. Qdashes parallel to the cavity showed a peak gain blue shift of 10 nm compared to the Qdashes perpendicular to the cavity and peak gain difference of $>5\ cm^{-1}$ below the threshold. This was attributed to the addition of light-hole contributions into the primarily heavy-hole transitions in these Qdashes. This study was further supported by Hein et al. [189] and Podemski et al. [187] via columnar Qdashes growth, stating a strong relationship between the polarization degree of emission and the orientation of the columnar Qdashes. Besides the above findings, Popescu et al. [192] showed that geometrical asymmetry of Qdashes influences the carrier migration (ambipolar carrier migration length), and noticed a 20% reduction in carrier migration along Qdash elongation compared to that across the dash elongation (*i.e.* perpendicular to elongation).

Further detailed investigations on the optical properties of this new class of nanostructures grown on InAs/InGaAlAs/(100)-InP platform were performed. For instance, thermal quenching of the PL was studied by temperature dependent PL on InAs/InGaAlAs Qdash structures with deduced two activation energies which were ascribed to electron escape and heavy hole escape to the conduction and valance band in Qdash barriers, respectively [193]. A similar temperature dependent carrier dynamics was also carried out by Jahan et al. [194] on InAs/InAlAs Qdash heterostructure. Using PL and photo-reflectance (PR) measurements on a single Qdash layer embedded in InGaAlAs buffer layers, Rudno-Rudzinski et al. showed the existence of $\sim$2 ML thick wetting layer [195], observed the presence of ES at an energy of $\sim$150 meV above the GS transition in Qdashes [196], and studied the interband optical transitions in DaWELL structure with InGaAs/InGaAlAs Qwells [197]. In addition, Podemski et al. investigated the efficiency of excitons and free carrier injections in Qdash tunnel-injection structures via PL measurements [198] and measured Qwell-Qdash energy transfer up to 130 K employing PL excitation (PLE) study [199]. Marko et al. [200] showed in the high pressure measurements on Qdash-lasers that Auger recombination in Qdashes was the major contributor to the high threshold current density at room temperature.

### 4.2. InAs/InGaAsP Material System

#### 4.2.1. Qdashes on (100) InP substrate

Early work of Qdash growth on this material system started from the investigations on InP buffer layer on nominal [22] and vicinal [201,202] (100) InP substrates on MBE system. Gonzalez et al. [22] demonstrated that the buffer layer surface morphology played an important role in the formation of InAs nanostructures by growing the InP buffer layer using atomic-layer MBE and MBE. Under identical growth condition, the former growth method resulted in self-assembled Qwire-like nanostructures elongated along [1–10] direction while the latter outcome was Qdot-like formation. Later, via *in-situ* stress measurements, it was elucidated that the associated anisotropic stress relaxation of the heteroepitaxial system involving different group V elements was the key cause for Qwire formation [203]. On the other hand, Walther et al. [201] showed Qwire growth on both exact and vicinal [2° offcut along (−110)] (100) InP substrates employing InP, InGaAs and AlInAs buffer layers, and growth interruption after InAs deposition. This was attributed primarily due to strain and discarded the contribution due to the chemical details of the buffer layer under the given growth parameters. An AFM image of Qwires on AlInAs buffer layer is shown in Fig. 28(a). This work was further supported by Salem et al. [202] who also compared the nanostructure growth on nominal and 2° offcut [along (−110) and (010)] (100) InP substrates and found Qwire-like formation on the former two substrates and Qdot on the latter substrate. A low temperature (8 K) PL peak emission at ~1.46 μm with linewidth ~75 meV was observed from these Qwire nanostructures.

Later, Gendry et al. [204] addressed the size dispersion and wavelength tunability issue of InAs quantum-stick nanostructures. They showed employing a single stack of quantum-sticks in InP matrix layer that optimized epitaxial growth parameters could result in reduced nanostructure height dispersion. First, by increasing the growth temperature which in turn lowers the critical thickness for 2D/3D (three-dimensional) growth mode transition, they observed uniform islands growth, as depicted in Fig. 28(b). The measured room PL linewidth of the sample grown at

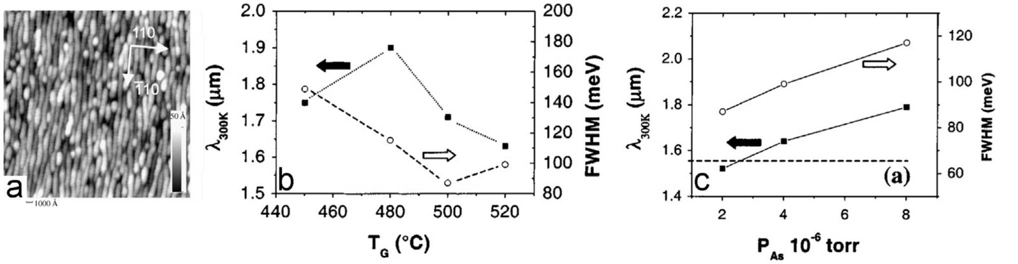


Fig. 28. (a) AFM image of InAs wires (InAs deposition thickness ~1.2 nm) grown on a ternary $Al_{0.52}In_{0.48}As$ buffer layer on (100) InP (b) PL characteristics [peak emission and linewidth] of InAs island PL spectra on InP buffer layer at 300 K as a function of the growth temperature for an InAs deposition thickness just above (~0.5 ML) the critical thickness. (c) PL characteristics of InAs islands on InP at 300 K versus the As overpressure during the InAs growth (growth temperature 520 °C, InAs deposition thickness 0.9 nm). Taken from [201,204].

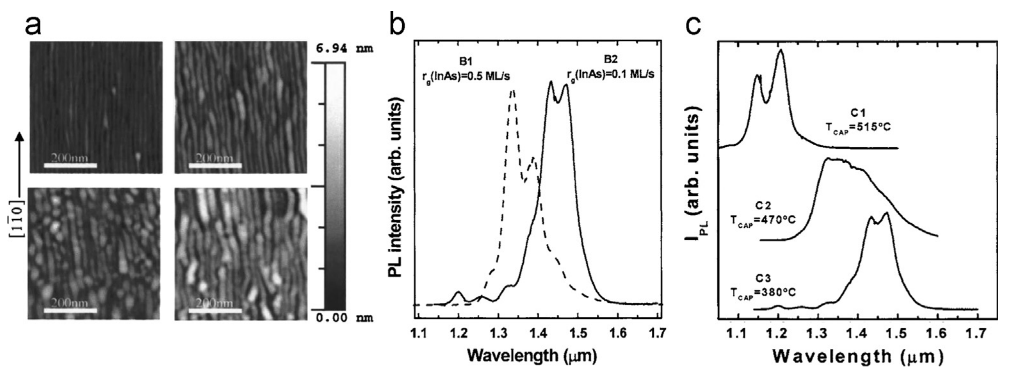


Fig. 29. (a) AFM images ($0.5 \times 0.5\ \mu m^2$) of four uncapped InAs Qwire samples with different InAs deposited thicknesses 2.5 ML, 3.3 ML, 4.3 ML, and 5.3 ML from upper left to bottom right. The four images have the same z-scale bar. (b) 12 K PL spectra of InAs Qwires grown at different InAs growth rates of 0.1 and 0.5 ML/s. (c) 12 K PL spectra of InAs Qwire samples where the InP cap layer has been grown at different substrate temperatures $T_{CAP}$=380, 470, and 515 °C. Collected from [205].

520 °C (InAs deposition 0.5–0.65 nm, just above the critical thickness at this temperature) was ~100 meV compared to ~170 meV for the sample grown at 480 °C (InAs deposition 1.6–1.8 nm, just above the critical thickness at this temperature). In addition, the tuning capability of the islands emission energy via InAs layer thickness variation was also highlighted; with the former sample PL peak wavelength at ~1.64 μm compared to the latter sample at ~1.9 μm. In brief, reducing the As overpressure during InAs deposition (see Fig. 28(c)), increasing the InAs thickness to a much larger values than the critical thickness for the 2D/3D growth mode transition, and higher growth temperature, were shown to be the optimum conditions for low height dispersion grown self-organized quantum-sticks. In fact, a PL linewidth of ~50 meV was reported at 8 K from the optimized single stack structure with island density $6 \times 10^{10}$ cm$^{-2}$. This achievement was accredited to the kinetic and thermodynamic factors such as adatom surface diffusion, strain accumulation, etc., that benefited the island self-organization [204].

In continuation to the growth parameter optimization for quantum islands size and emission control, Fuster et al. [205] studied the effect of InAs layer thickness on the Qwire formation and found that large Qwire formed with increased InAs layer thickness, as depicted in Fig. 29(a), which was consistent with other reports on the InAs/InGaAlAs material system, reviewed in Section 4.1. Next, they explored two additional methods that depends on the As/P exchange process control for Qwire formation; firstly, during InAs growth of Qwires, and secondly, during the InP capping layer deposition to cover the nanostructures. An increase in the InAs deposition rate from 0.1 ML/s to 0.5 ML/s (keeping other growth parameters fixed) resulted in PL emission blue shift of ~100 nm (~1.45 μm to ~1.35 μm) deduced from the 12 K PL experiment, as shown in Fig. 29(b). This was attributed to the exchange between As and P atoms at the InP surface exposed to As flux during InAs growth. In general As/P exchange process produces source of In at the expense of the InP buffer layer quality, resulting in an effective InAs growth rate higher than the deposition rate, and hence larger size wires with higher heights (emitting at longer wavelengths) were grown at slow InAs growth rates. On the other hand, the PL spectrum shifted to shorter wavelengths as the substrate temperature during capping layer growth was increased from 380 °C to 515 °C as illustrated in Fig. 29(c). In this case, P/As exchange at the interface between the InAs wires and InP capping layer when exposed to P flux during InP capping layer growth affected the height of the InAs Qwires [206].

Subsequently, growth and optical characterization of multi-stack Qwire structures were reported by Alen et al. [208] where 10 stacks of InAs/InP Qwires were grown with 5 nm and

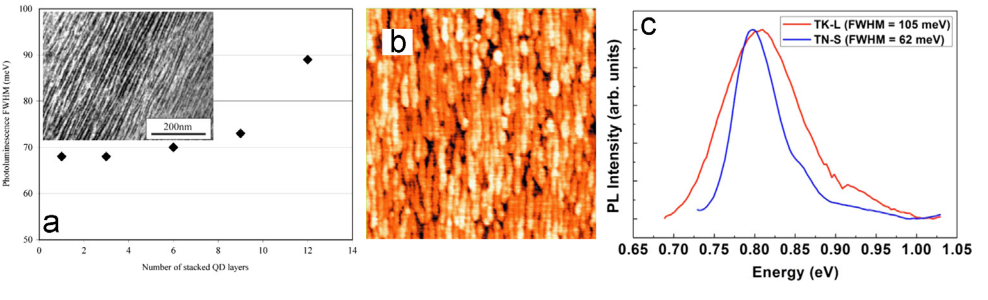


Fig. 30. (a) Room temperature PL linewidth of stacked InAs/InGaAsP Qdashes as a function of the number of stacking layers. Inset shows the plan-view TEM micrograph of a stack of 6 Qdash layers. (b) AFM image ($1 \times 1$ μm$^2$) of an uncapped 3 stacked InAs/InGaAsP Qdash sample, and (c) room temperature PL spectra of a 5 stack Qdash sample with a thicker InGaAsP first capping layer and a longer growth interruption time (TK-L) and a Qdash sample with a thinner InGaAsP first capping layer and a shorter growth interruption time (TN-S) sample. Courtesy of [6,7,207].

10 nm spacer thickness for comparison. It was shown that smaller spacer layer thickness structure resulted in Qwire size homogeneity and uniformity of Qwire stacks attributed to the strain driven vertical filtering of the Qwire sizes along the growth direction. Low temperature PL peak emission around 1.54 μm was observed with ~100 meV PL linewidth. In contrast, the thick InP spacer layer structure was highly inhomogeneous with broad PL linewidth of ~350 meV due to inhibition of strain propagation and hence no size filtering (vertically uncorrelated Qwires). The results of this work is in line with Podemski et al. [187] work on InAs/InGaAlAs material system. Following this work, a detailed analysis on the effect of capping layer thickness on 2-stack and 5-stack Qwire structures inhomogeneity was carried out by Fuster et al. [209] utilizing the *in-situ* and real time stress measurements and reflection high-energy electron diffraction (RHEED) observations besides relating to the P/As switching process. Rather than reducing the barrier layer thickness for achieving homogeneous size Qdashes, Lelarge et al. [207] recently developed a solution to achieve the same with a barrier thickness of 40 nm. They utilized an empirical rule involving the growth conditions, number of Qdash layers, thickness, and the strain of barriers as key parameters to identify the nominal thickness of the subsequent dash layer in order to compensate for the natural thickening of the Qdashes during stacking. With this method MBE grown Qdashes up to 10 stacks were achieved without affecting the room temperature PL linewidth (maintained at ~70 meV), as illustrated in Fig. 30(a). The optimized double capping technique, primarily developed for the InAs/InP Qdots growth (discussed in Section 2.2), was also employed by Zhou et al. [6,7] to obtain homogeneous Qdashes and to tune the emission wavelength of a single and multi-stack InAs/InGaAsP Qdash structures on (100)InP substrate. By selecting a thin 2.2 nm first capping layer and short 30 s growth interruption time, they measured a room temperature PL linewidth of 60 meV from 5 stacked Qdash structure (TN-S) centered at 1.55 μm, shown in Fig. 30(b) and (c).

Very recently, Lenz et al. [210] explored the formation of Qdashes on InGaAsP buffer layers on (100) InP grown by MOCVD system. 2.65 ML thick InAs deposition thickness was utilized for Qdash growth in a single and 7 stack structure, separated by 40 nm InGaAsP barrier layers. A series of samples at different growth temperature (470 °C to 530 °C) and TMI flow rate (13–200 sccm) revealed Qdash formation at low temperature ($\leq$500 °C) and/or high flow rate ($\geq$100 sccm). The PL linewidth of ~60 meV centered at ~1.55 μm was reported at room temperature. Moreover, composition fluctuation of the InGaAsP material towards the InAs rich and GaP rich regions was also noted. Alternatively, Faugeron et al. [211] presented the concept of an asymmetrical cladding in the Qdash active region. An undoped intermediate optical index

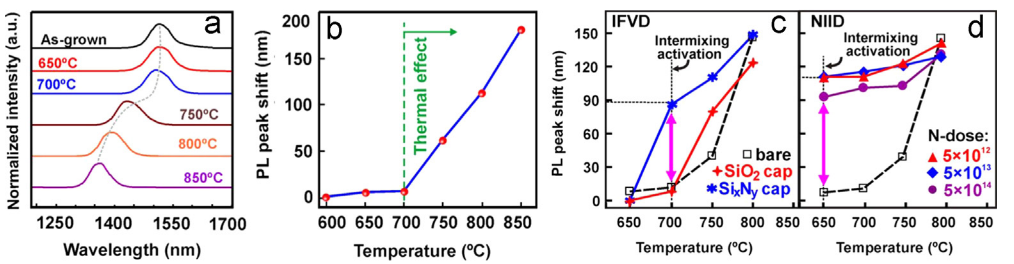


Fig. 31. (a) PL spectrum and (b) PL peak shift at 77 K taken under an excitation density of 3 W/cm$^2$, when the GS PL signal from InAs/InGaAlAs DaWELL samples is not saturated, versus annealing temperature, and capped with 200 nm $SiO_2$. (c) Peak shift of 77 K PL against annealing temperature using the following: (c) IFVD with $SiO_2$ and $Si_xN_y$ cap dielectric cap annealing, and (d) NIID at different doses. The dotted line in (c) and (d) indicates the activation temperature required to initiate the spatially selective intermixing. Taken from [219].

slab layer was inserted between the Qdash active zone and the substrate in the 6-stack Qdash-in-barrier structure with the aim of reducing the overlap of the optical mode with the lossy p-doped cladding layers. The room temperature PL peak wavelength was shown to be independent of the slab layer thickness, at ~1.57 μm with no change in the PL linewidth, thus maintaining the optical quality of the material.

#### *4.2.2. Qdash optical properties*

The radiative optical transitions available in InAs/InP self-assembled Qwire structure was investigated by Alen et al. [212] employing PL and absorption measurements. Several optical transitions were observed at 85 K, consistent with both the measurements, and were attributed to Qwires of different height. In addition, the non-radiative recombination mechanism responsible for the quenching of PL was related to the thermal carrier escape of carriers out of the wires towards the barrier material. In contrast, Salem et al. [213] reported that the multicomponent transitions from the InAs/InP quantum islands structure showed the existence of excited states and substantiated the results with PLE measurements at 8 K. In another study, Heck et al. [214] studied the band structure of the DaWELL and Qdash-in-barrier InAs/InGaAsP structures on (100) InP and found that electron states are not confined in the former structure while weakly confined in the latter one due to small effective mass and conduction band offset [215].

### *4.3. Post-growth tuning of InAs/InP Qdashes*

Our group pioneered in the intermixing study of InAs/InGaAlAs DaWELL nanostructures with the first demonstration of *ex-situ* defect annealing and wavelength tuning using the IFVD process with 200 nm $SiO_2$ capping by Djie et al. [216]. As shown in Fig. 31(a) and (b), a linear increase in the low temperature (77 K) PL peak blue-shift was observed in a 4 stack Qdash structure with increasing annealing temperature, attributed to the strong thermally induced group III intermixing effects and reaching a maximum value of 180 nm at 850 °C. In addition, a strong increase in the radiative efficiency indicated by the improvement in the integrated PL signal (30–40% increase) was reported at 700 °C compared to the as-grown Qdash structure, with minimal PL peak shift (~1.532 μm versus ~1.54 μm at low excitation power). This improvement in the material quality after intermixing was related to the reduced defect density which might be presented near the DaWELL interfaces due to low growth temperature and increased stress field. A subsequent device fabrication and improved performance was also demonstrated which will be discussed in Section 5.1. On the other hand, it was shown that intermixing was enhanced under a $Si_xN_y$ cap at the same temperature of 700 °C with a differential PL peak blue shift of 80 nm (PL peak at ~1.46 μm at low excitation power), as shown in Fig. 31(c), and was attributed to the different group-III intermixing rates [217]. In addition, the material quality was maintained with no significant broadening of the PL linewidth.

A spatial control of group-III intermixing rate by IID technique employing nitrogen ions (NIID) was also reported on four stacks InAs/InGaAlAs DWELL structure separated by 30 nm tensile strained InGaAlAs barrier layer [218], and plotted in Fig. 31(d). At low temperature annealing of 650 °C and 700 °C a large blue shift in the PL peak of the samples implanted with $5 \times 10^{12}$ and $5 \times 10^{13}$ ions/cm$^2$ was observed with a value ~112 nm compared to the bare as-annealed samples. The PL blue shift value reduced to ~108 nm at $5 \times 10^{14}$ ions/cm$^2$ ascribed to the formation of clusters that trapped point defects during annealing treatment and effective reduction in defect concentration. An indirect NIID (implantation to the 300 nm thick $SiO_2$ protected sample) process was also carried out at various ion doses to assess the placement of implantation induced damage into the sample and correlate the defect migration and intermixing efficiency. An integrated PL intensity comparable to the as-grown sample was observed with indirect NIID process for all the above implantation doses while the direct NIID showed weaker PL intensity, thus validating the fact that residual defects generated post-annealing with indirect NIID process was minimum. The optical quality of the active region was retained during the process. The PL peak wavelength and blue shift of the indirect NIID remained at ~112 nm at annealing temperature of 650 °C and 700 °C and the PL linewidth was smaller than the as-grown and as-annealed samples [219]. These demonstrations of annealing effect on practical *p-i-n* structures allowed realization of bandgap tuned lasers and provided insight into the technological capabilities of intermixing in monolithic integration of different devices for photonics integrated circuits.

### 4.4. Chirped Qdash active region design

The large inhomogeneous broadening of self-assembled Qdash nanostructure active region demerits the laser performance since there is always a trade-off between the spectral linewidth and the minimum gain required for driving the device. In contrast, the flexibility offered by Qdash geometry and density has been exploited for realization of broad gain material for SOA and broadband light emitting devices. Various approaches were reported in literature to create additional Qdash inhomogeneity within the active region, usually referred as chirped designs. Deubert et al. [220] introduced this technique on Qdash platform by growing two device-structures; firstly, the 6-stack Qdash with varying InAs nominal thickness (3 to 4.6 ML), and fixed 25 nm barriers graded separate confinement heterostructure structure; and secondly, the 4-stack Qdash with identical 4 ML InAs deposition thickness in conjunction with the reduced barriers of 10 nm for strain coupling, and for modifying the Qdash size from layer to layer, as discussed earlier. Although PL measurement results were not reported, the laser device results below threshold showed a broad electroluminescence from both the structure suggesting an increase in gain-bandwidth by ~45% compared to the conventional 4 stack Qdash laser structure with identical InAs layer thickness with thick barriers. In the same year, Reithmaier et al. [26]

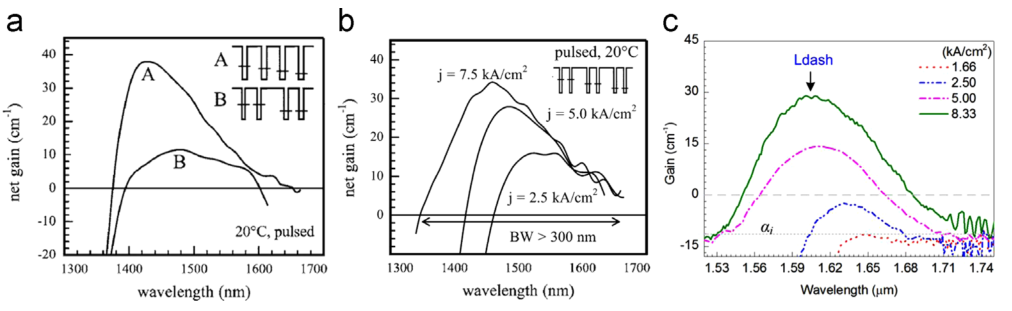


Fig. 32. Pulsed room temperature modal net gain of a InAs/InGaAlAs SCH Qdash laser structure with three broadened gain designs: (a) first (design A) consisting of four Qdash layers with different Qdash sizes (InAs deposition thickness) and the Qdash layers are separated by 10 nm thick barriers; second (design B) consisting of two Qdash layer groups of different nominal Qdash layer thicknesses, and the individual Qdash layers are separated by 10 nm and the groups by 20 nm, respectively; (b) third (design C) is a six layer three Qdash group structure combining designs A and B, as shown in the inset. (c) Gain of a four stack DaWELL laser structure with chirped barrier layer thickness (10, 10, 15, 20 nm). Adapted from [222,225].

demonstrated a wide gain-bandwidth of 270 nm with peak gain 40 $cm^{-1}$ at 5 kA/$cm^2$ from a chirped active region which is a combination of the above two designs *i.e.* 4 dash layers with different InAs thickness separated by fixed thin 10nm barriers (design A) [221]. The measurement was done under pulsed current using segment contact method and shown in Fig. 32(a). In addition, another design named as $2 \times 2$ scheme (design B) wherein two groups of nominally identical Qdash layers, each separated by 10 nm barriers, and the groups separated by 20 nm barriers, was proposed and demonstrated. A gain-bandwidth of 210 nm was reported from this structure with peak gain of 10 $cm^{-1}$ at pulsed current density of 5 kA/$cm^2$ (see Fig. 32(a)).

Because of good tunability properties and control of Qdash emission, Somers et al. [222] was able to further extend the gain-bandwidth of Qdash structure to a value of $>300$ nm with peak gain of 35 $cm^{-1}$ which satisfies the need of broadband SOA covering the entire long wavelength communication band from $\sim$1.33 μm to $\sim$1.67 μm (see Fig. 32(b)). This is achieved by using 6-stack Qdash layers (design C) that was separated into three groups with 20 nm barrier in between, and the two Qdash layer within a group separated by 10 nm barrier. The nominal InAs layer thickness in each group was varied from 0.91 nm to 1.31 nm [5]. Very recently, our group demonstrated a broad PL linewidth from a chirped InGaAlAs barrier 4-stack DaWELL laser structure [223] based on the systematic study on the effect of barrier thickness on the active region inhomogeneity [224]. By employing variable barrier thickness of 10 nm (p-side), 10 nm, 15 nm, and 20 nm (n-side), we demonstrated an ultra-broad 77 K PL linewidth of $\sim$151 nm and found a significant increase in the linewidth when compared to a 4 stack fixed 10 nm barrier similar Qdash laser sample (77 K PL linewidth $\sim$100 nm). We also performed gain measurements on the chirped barrier thickness Qdash structure utilizing the segment contact method, and measured a broad gain-bandwidth of $\sim$140 nm under CW current density of 8.3 kA/$cm^2$ with peak modal gain $\sim$41 $cm^{-1}$ [225], as illustrated in Fig. 32(c).

## 5. InAs/InP Qdash Devices

In this section, we reviewed the accomplishments of Qdash active region in semiconductor devices by discussing the edge-emitting FP lasers, mode-locked lasers, SOA, and the recent new class of broadband lasers. Unlike conventional lasers, which emit narrow linewidth coherent beam, the broadband laser produces stimulated emission with much broader spectral linewidth [226]. On the other hand, mode locking characteristics of the Qdash lasers, which was initially investigated by Renaudier et al. [120], has shown substantial improvement in the performance, as depicted in Fig. 2(b) [207,227], thanks to the inhomogeneous nature of the Qdash active region that resulted in emission of sub-pico second pulses. A detailed review of the mode locking characteriscs of Qdash lasers is presented in Section 5.2. Finally, we summarized utilization of Qdash active medium in SLD demonstrations with bandwidth reaching $\sim$110nm in the C–L–U bands; the research field in which our group pioneered.

### 5.1. InAs/InP Qdash lasers

The first demonstration of semiconductor diode laser employing Qdash active region was reported by Wang et al. [3] at room temperature using InAs/InGaAlAs Qdash material system on (100) InP substrate. This founding work led to the realization of the technological capabilities of this nanostructure, particularly in the field of mode-locking and optical amplification. The natural self-assembled growth of Qdashes on InP substrates without any assisting growth techniques makes it as a favorite contender for realizing long wavelength semiconductor devices.

#### 5.1.1. Lasers on (100) InP substrate

*5.1.1.1. InAs/InGaAlAs Material System.* Fig. 33(a) shows the room temperature lasing from 1–, 3–, and 5–stack InAs/InGaAlAs DaWELL structure, reported first by Wang et al. [3] under pulsed current operation, emitting at 1.60 μm, 1.62μm, and 1.66 μm, respectively. The corresponding threshold current densities were 410 A/cm$^2$, 500 A/cm$^2$ (167 A/cm$^2$ per layer), and 766 A/cm$^2$ (154 A/cm$^2$ per layer), obtained from 100 μm stripe broad-area lasers with cavity lengths 1.5–4.0 mm (the cavity was perpendicular to Qdash elongation). The internal quantum efficiency of $\sim$0.6 and internal loss $\sim$10 cm$^{-1}$ was extracted and high modal gain of $\sim$15 cm$^{-1}$ from the single stack laser diode. These encouraging results motivated the research community to pursue further on this material system. Next report came from Schwertberger et al. [181] who reported wavelength tuning of InAs/InGaAlAs Qdash lasers from 1.54 μm to 1.78 μm by just varying the InAs deposition thickness from 5.0 ML to 7.5 ML. A threshold current density as low as 900 A/cm$^2$ (225 A/cm$^2$ per layer) from 40 × 1000 μm$^2$ device was reported with a total output power > 100 mW and characteristics temperature $T_0$ $\sim$61 K (20–80 °C). The results are summarized in Fig. 33(b). Subsequently, with the improvement in the material quality, indicated by the improved quantum efficiency of $\sim$0.6 and internal loss $\sim$8.5 cm$^{-1}$ [180], a reduced transparency current density of 350 A/cm$^2$ (90 A/cm$^2$ per layer) was reported, which is the among the best value reported in this material system. In addition, a 3 × 2000 μm$^2$ ridge-waveguide lasers at $\sim$1.55 μm was also demonstrated with an output power > 30 mW at room temperature. The flexibility in tuning the emission wavelength of Qdashes was shown by Rotter et al. [182] who demonstrated a lasing emission from a 5-stack InAs Qdashes in InGaAs Qwell laser structure on (100) InP at 2.03 μm, which is the record longest wavelength ever reported on any InAs/InP Qdash or Qdots material system. A pulsed threshold current density of 540 A/cm$^2$ (108 A/cm$^2$ per layer) was reported with $\sim$0.52 internal quantum efficiency, $T_0$=41 K, and a very high internal loss $\sim$55 cm$^{-1}$ which was attributed to Rayleigh scattering of the laser mode due to local undulations of the refractive index near the Qdashes.

Following Rotter et al.'s work, the potential of this nanostructure to cover significantly longer wavelength range was further affirmed by Somers et al. [221] who reported 1.88 μm lasing

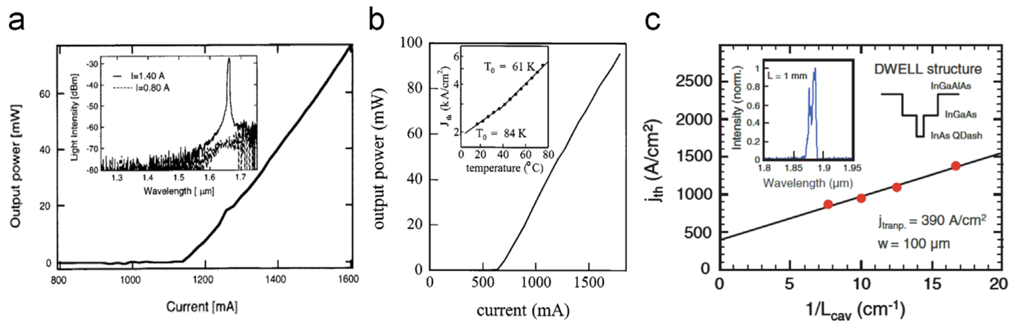


Fig. 33. (a) A two-facet light output versus pulsed injection current measured on a five-stack Qdash laser diode with geometry of 100 × 1500 μm$^2$. The inset in (a) is the electroluminescence spectra under different pump levels for the device. (b) Single facet light output versus pulsed injection current of a 40 × 500 μm$^2$ Qdash laser emitting at 1.54 μm. The inset in (b) shows the temperature dependence of the threshold current density with solid lines representing the linear fits to the data points. (c) Threshold current density of a long wavelength broad area Qdash laser with a DaWELL design versus inverse cavity length. The inset in (c) shows the lasing emission spectrum of a 1000 μm long device at 1.88 μm. Taken from [3,26,181].

emission from InAs/InGaAs DaWELL lasers with good device performance (~0.6 internal quantum efficiency and ~4 $cm^{-1}$ internal loss), as shown in Fig. 33(c). Room temperature CW operation of 4 stack graded SCH InAs/InGaAlAs Qdash lasers was reported by Resneau et al. [228] who developed 1.57 μm ridge-waveguide lasers with total power > 100 mW and a flat low RIN of −162 dB/Hz in 0.1–13 GHz range (lower than the Qwell laser counterpart). The extracted small internal loss of 4 $cm^{-1}$ from cavity length dependence measurements of the external quantum efficiency is among the smallest reported in this material system. In addition, dynamic characteristics measurements revealed a modulation efficiency of 0.36 $GHz/mA^{0.5}$, K-factor of 1.51 ns and maximum intrinsic bandwidth of 5.9 GHz. These values were further improved in their following work [26] ([229]) with 0.64 (0.72) $GHz/mA^{0.5}$ modulation efficiency and 5.2 (7.5) GHz resonance frequency value, which was also based on non-optimized Qdash laser design for high speed measurements. The small signal modulation bandwidth in the former case was 5.6 GHz.

The thrust to improve the high speed performance of Qdash lasers lead to the realization of p-doped [230,231] and tunnel injection schemes [186,188]. Mi et al. [188] reported a high $T_0$ ~ 196 K (up to 40 °C), enhanced small signal modulation bandwidth of 8 GHz at 5 °C, sub-threshold LEF ~1 and < 1.5 frequency chirp, by employing a modulation p-doped 6-stack InAs/InGaAlAs Qdash laser under pulsed current operation, as shown in Fig. 34(a) and (b). This improvement was attributed to the increase in gain and differential gain of the active region. However, the internal loss increased substantially (15.5 $cm^{-1}$) due to p-doping induced increased Auger recombination but a good internal efficiency of ~0.6 was maintained. Later, Hein et al. [230] demonstrated a CW 8 GHz small signal modulation bandwidth with 0.76 GHz/$ma^{0.5}$ modulation efficiency at room temperature from a moderately p-doped 3 × 580 $\mu m^2$ ridge-waveguide 4-stack Qdash laser with exceptionally high slope efficiency 0.4 W/A at 1.55 μm. A systematic and detailed investigation of the effect of p-doping concentration on the Qdash lasers revealed [231] that high p-doping concentrations increased the differential gain by more than 50% but the enhanced gain compression and enlarged thermal heating due to high internal losses overcompensated this benefit. Therefore, a maximum small signal modulation bandwidth of 8 GHz in CW operation at room temperature was obtained for moderate p-doping concentration (~10 holes per Qdash) with internal loss 11 $cm^{-1}$, ~0.76 internal quantum efficiency, and $T_0$ ~83 K (20 to 80 °C). A maximum $T_0$ ~ 96 K (20 to 80 °C) and modal gain ~41 $cm^{-1}$ were reported for 100 holes per Qdash p-doping but with an increased internal loss and transparency current density of 28 $cm^{-1}$ and 1.3 $kA/cm^2$, respectively. By employing tunnel injection scheme in tandem with p-doping, Mi et al. [186] succeeded in pushing the small signal modulation bandwidth up to 12 GHz at 5 °C, which is the best value reported in InAs/InP Qdash system, with an enhanced $T_0$ ~ 204 K (up to 40 °C) and reduced sub-threshold LEF < 0.7. This was attributed to the combined effects of p-doping and tunnel injection which minimized the hot carrier effects and carrier leakage in the active region. On the other hand, Hein et al. [232] reported a room temperature maximum small signal bandwidth of 9.6 GHz utilizing 2.5 × 600 $\mu m^2$ undoped 6-stack InAs/InGaAlAs Qdash laser in CW operation with a modulation efficiency of 0.82 $GHz/mA^{0.5}$, K-factor of 0.78 ns and maximum intrinsic bandwidth of 11.4 GHz, as illustrated in Fig. 34(c). This is the best value reported in Qdash system at room temperature. The corresponding above-threshold LEF of 2.5 was obtained utilizing the amplitude-modulation/frequency-modulation method. In another study, Dziak et al. [233] also measured the above-threshold LEF of Qdash laser using the injection locking scheme. In this case, the measured LEF increased from 1.2 to 8.6 with increasing current injection at the peak lasing wavelength.

The best multi-stack Qdash laser threshold current density value [730 A/cm$^2$ (46 A/cm$^2$ per layer)] on this material system was reported by Hein et al. [189] from 1.3 mm long 16-stack columnar Qdash laser structure emitting at 1.7 μm followed by Rotter et al. [182] [540 A/cm$^2$ (108 A/cm$^2$ per layer)]. In terms of device internal quantum efficiency, our group reported the best value of 0.93 for the 4-stack Qdash laser [216]. In addition, our group successfully showed the improvement in the Qdash laser performance by controlled IFVD intermixing process with ~11% and ~45% reduction in the threshold current and transparency current density, respectively, while maintaining the other laser performance parameter values similar, and lasing at ~1.61 μm. This was attributed to the defect annealing at the Qdash-Qwell interfaces in the 4-stack InAs/InGaAlAs Qdash laser.

Chirped active region based Qdash lasers were also reported in this material system by various groups, and their designs has already been discussed in Section 4.4. In terms of device performance Deubert et al. [220] and Somers et al. [221,222] reported lasing at 1.53 μm with reasonable threshold current density (250–440 A/cm$^2$ per layer), internal quantum efficiency (0.6–0.75) and internal loss (4.6–10 cm$^{-1}$). On the other hand, our chirped Qdash lasers exhibited 550 A/cm$^2$ per layer threshold current density with 0.85 and 11 cm$^{-1}$ internal quantum efficiency and internal loss, respectively [225]. Lastly, the reliability properties of the strained InAs/InGaAlAs Qdash lasers were also reported by Resneau et al. [234] because of their susceptibility to the creation of crystal defects. Lifetime measurements under CW operation on many 0.9 mm [229] and 1.9 mm [26] long Qdash lasers were carried out over 2800 h and 7000 h, respectively, at 60 °C. A stable average output power of 10 mW per facet was observed with slight improvement in power after the first 100–200 h of burn-in time in the longer laser cavity cases.

*5.1.1.2. InAs/InGaAsP Material System.* Qdash lasers based on this material system were embraced relatively late with Moreau et al. [235] reporting the effect of layer stacking and p-doping on the performance of 1.52 μm InAs/InGaAsP Qdash lasers on (100) InP substrate, as depicted in Fig. 35(a). A pulsed threshold current density as low as 1100 A/cm$^2$ (123 A/cm$^2$ per layer) from 50 × 600 μm$^2$ device with 9-stack InAs/InGaAsP DaWELL structure was reported at room temperature. The corresponding transparency current density was 83 A/cm$^2$ per layer and high modal gain of 48 cm$^{-1}$ (5.4 cm$^{-1}$ per layer). These values were found to be superior when compared to the 6-stack and 12-stack Qdash laser performances. In general, the characteristics temperature $T_0$

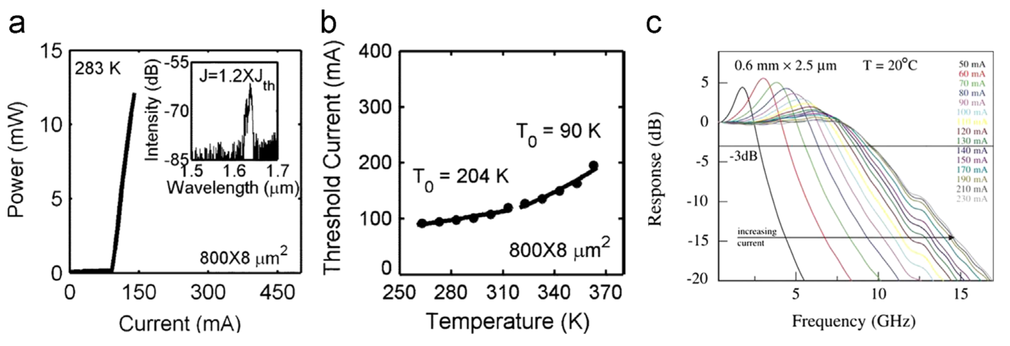


Fig. 34. Characteristics of p-doped InAs tunnel injection InAs/InGaAlAs Qdash lasers under pulsed operation: (a) *L–I* and output spectrum (inset) and (b) variation of threshold current with temperature. (c) Room temperature small-signal modulation response of a ridge-waveguide 2.5 × 600 μm$^2$ undoped InAs/InGaAlAs Qdash laser for various CW drive currents. Reproduced from [186,232].

measured from these different stack lasers were in the range of ~60–70 K (20 to 80 °C) with internal loss ~14 $cm^{-1}$. On the other hand, p-doping at different doping concentration on the 6-stack sample revealed insignificant improvement in characteristics temperature $T_0$~60 K as observed in Ref. [186] with substantially increased internal loss 25–46 $cm^{-1}$. These demonstrations were soon followed by room temperature ridge-waveguide Qdash laser operation report lasing at 1.51 μm with output power >14 mW and slope efficiency 0.4 W/A [235–237]. The above-threshold LEF values which is in the range of 3.6–6.5 was found to increase with current injection, similar to other reports on InAs/InGaAlAs system [233]. This was attributed to the plasma effect and the carrier filling of the non-lasing states (higher transition energy states and the wetting layer), which resulted in reduction of differential gain above threshold. In another study, Lelarge et al. [207] compared the Qdash-in-barrier and DaWELL scheme at room temperature on 50 × 2000 $\mu m^2$ device under CW operation and observed a red shift in the lasing wavelength (1.56 μm in the former scheme while 1.65 μm in the latter scheme). In addition, the transparency current density, plotted in Fig. 35(b), was shown to significantly decrease in the DaWELL scheme with 660 A/$cm^2$ (110 A/$cm^2$ per layer) compared to the Qdash-in-barrier scheme 1140 A/$cm^2$ (190 A/$cm^2$ per layer), due likely to better carrier injection [238]. An internal quantum efficiency of 0.8 with an estimated internal loss of 19 $cm^{-1}$ from the DaWELL structures was reported. In addition, a modal gain as high as 105 $cm^{-1}$ (from short 140 μm cavity) and characteristics temperature $T_0$~60 K (up to 80 °C) were extracted. It was shown that even the p-doping in the active region did not increase $T_0$ which was attributed either to the shape of the nanostructures or to the band structure.

Later, through high quality growth optimization of Qdashes and utilizing buried ridge fabrication process, a high $T_0$~135 K (25 to 85 °C) was reported from p-doped 6-stack Qdash-in-barrier laser with two times higher modal gain compared to the undoped laser [66 $cm^{-1}$ (11 $cm^{-1}$ per layer) versus 34 $cm^{-1}$ (5.6 $cm^{-1}$ per layer)], but with high threshold (~10 kA/$cm^2$) and internal loss (~60 $cm^{-1}$) [239]. Moreover, a significant improvement in the device dynamic characteristics was also reported with a high relaxation frequency value of 13.5 GHz obtained from the RIN measurements (−155 to −160 dB/Hz from 0.5 to 20 GHz); among the best values reported on InAs/InP Qdash material system. However, the p-doped device showed an inferior measured small signal modulation bandwidth value of 7 GHz due mostly to RC parasitic limitation related to the buried ridge process. But, a strong decrease in the above-threshold LEF < 3.5 for current up to 140 mA and a successful large signal modulation capability at 10 Gbps utilizing NRZ PBRS signal affirmed the p-doped Qdash laser compatibility for 10 Gbps CW operation.

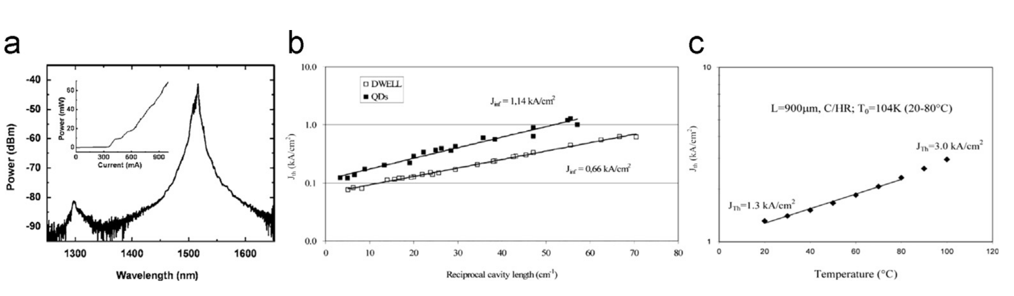


Fig. 35. (a) Room temperature above threshold lasing spectrum under pulsed excitation of InAs/InGaAsP DWELL broad area laser. The inset in (a) shows the *L–I* characteristic of the 40 × 518 $\mu m^2$ device. (b) Threshold current density of 50 μm broad area lasers versus reciprocal cavity length for InAs/InGaAsP dash-in-a-barrier and dash-in-a-well structures. (c) Threshold current density variation with temperature of an optimized 50 × 900 $\mu m^2$ dash-in-well broad area lasers with reduced InGaAsP Qwell thickness of 6 nm. Collected from [207,235].

Alternatively, Lelarge et al. [207] demonstrated an increase in $T_0$ to 100 K (20 to 80 °C), as shown in Fig. 35(c) without employing any p-doping in the active region, and jut by optimized active region design with a thin InGaAsP Qwell layer of 6 nm. This was attributed to an increased energy level of the ES of the DaWELL structure which reduced the carrier escape from Qdash to Qwell. This slight modification in the active region design was further attested by ridge-waveguide (buried ridge stripe) $1.5 \times 600\ \mu m^2$ Qdash laser demonstration under CW operation. A characteristic temperature $T_0 \sim 80$ K (up to 80 °C) with threshold current density as low as 12 mA and lasing wavelength $\sim 1.55\ \mu m$ was reported. This Qdash active region design was further optimized by Dagens et al. [240] by reducing p-side (20 nm) and n-side (70 nm) SCH layers for the 6-stack InAs/InGaAsP Qdash laser in order to reduce the carrier transit time, and to limit the recovery of the optical mode and the absorbing p-doped waveguiding layers. A 600 µm long buried ridge-waveguide laser demonstrated a relaxation frequency of about 8.5 GHz, relatively flat RIN - 155 dB/Hz (0.1–16 GHz), and a small signal modulation bandwidth of 10.5 GHz in CW operation and room temperature (largest value ever reported on any Qdash material system), as shown in Fig. 36(a) and (b). The laser output power was $>25$ mW, $T_0 \sim 72$ K (20–80 °C) and CW threshold current of 32 mA. Furthermore, investigation of the large signal modulation characteristics on 300 µm long device utilizing 10 Gbps NRZ PRBS signal and measuring the BER after passing through 10 Gbps synchronous digital hierarchy (SDH) receiver demonstrated a floor free BER with $10^{-10}$ sensitivity of $-11$ dBm with 7 dB extinction ratio at the laser output. Even at elevated temperatures of 75 °C a successful floor-free back-to-back BER with $10^{-10}$ sensitivity of $-9.6$ dBm at 10 Gbps was reported by Lelarge et al. [207]. P-doping on this optimized active region design was also performed and reported via fabrication of the DFB lasers [241] which is discussed in Section 5.1.4.

Tunneling injection scheme was also investigated by Lelarge et al. [227,242] on the InAs/InGaAsP Qdash laser material system. A threshold current density of 2000 A/cm$^2$ (334 A/cm$^2$ per layer) was obtained from the optimized $50 \times 600\ \mu m^2$ laser device under CW operation and the transparency current density as low as 155 A/cm$^2$ per layer. A buried ridge-waveguide configuration incorporating the tunneling scheme was later utilized to test the dynamic properties. The $1.5 \times 600\ \mu m^2$ optimized laser device exhibited a threshold current of 16 mA with slope efficiency 0.34 W/A, output $>10$ mW and $T_0 \sim 50$ K (20 to 80 °C). The room temperature RIN measurements resulted in a value of - 155 dB/Hz from 0.1–16 GHz range with an extracted resonance frequency $\sim 8.5$ GHz, and measured small signal modulation bandwidth of about 4.5 GHz, which showed strong parasitic-like roll off related to carrier transport

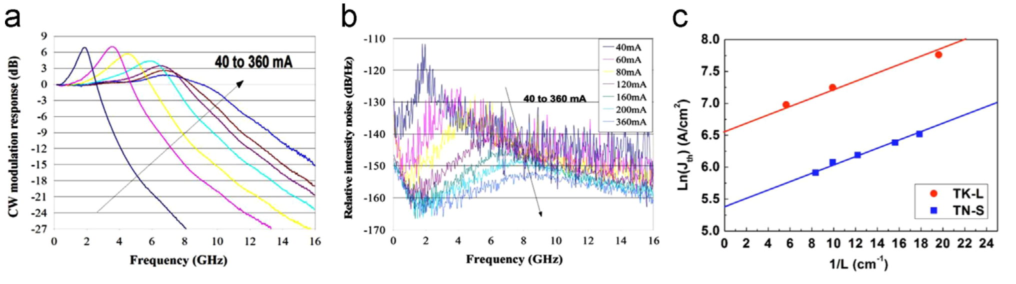


Fig. 36. (a) Small signal modulation response on a 600 µm as-cleaved, reduced SCH layer thickness buried ridge stripe DaWELL laser at 25 °C and (b) the corresponding RIN measurement. (c) Threshold current density versus the reciprocal cavity length for 5-stack Qdash laser samples TN-S (TK-L) with 2.2 nm and 2.5 nm cap, and the corresponding 30 s and 60 s growth interruption. Solid lines in (c) are exponential fits of experimental results. Adapted from [240,243].

limitations [242]. This insignificant effect of tunneling scheme on the laser dynamic characteristics was related mainly to the large escape of carriers from the injector-Qdash ensembles which could be improved via higher energy barriers or moderate p-doping as has been demonstrated by Mi et al. [186] utilizing both p-doping and tunnel injection scheme.

In terms of the laser static performance, Zhou et al. [6,243] demonstrated the lowest threshold current density of 360 A/cm$^2$ (72 A/cm$^2$ per layer) and transparency current density as low as 220 A/cm$^2$ (45 A/cm$^2$ per layer) from 5-stack Qdash-in-barrier SCH laser structure grown by the optimized double-cap technique, and utilizing 2.2 nm cap with 30 s growth interruption (TN-S), as shown in Fig. 36(c). These are the best values reported on InAs/InGaAsP Qdash material system with extracted internal quantum efficiency and internal loss of 0.58 and 7 cm$^{-1}$, respectively, and lasing at ~1.55–1.58 µm. In addition, a detailed study on the effect of stacking layers on the Qdash laser performance was also performed [7,244] with demonstrated modal gain of 8 cm$^{-1}$ and a red shift in the lasing wavelength (from 1.48 to 1.58 µm) on increasing the stacks from 2 to 6. This was ascribed to the carrier re-distribution between multiple layers of inhomogeneous Qdashes. The high modal gain of Qdash lasers, corroborated via lasing from very short cavity lasers, has demonstrated in various reports [5,26,207,245]. In particular, a 120 µm cavity exhibiting lasing with highest exhibited slope efficiency of 0.5 W/A was reported by Merghem et al. [246]. The 2 × 120 µm$^2$ 6-stack SCH Qdash laser device exhibited a threshold current density of 2.5 kA/cm$^2$, lasing at 1.55 µm, output power >5.0 mW, and 34 cm$^{-1}$ modal gain. This was followed by a detailed optimization of the modal gain by employing undoped multi-stack DaWELL structures and also introducing p-doping in the active region. A modal gain as high as 60 cm$^{-1}$ was reported by Merghem et al. from a 15 stack undoped and 6 stack p-doped DaWELL structure [247]. Also, a small above-threshold LEF of <2.4 (up to 150mA) was measured from these devices with extracted resonance frequency of >10 GHz from the RIN measurements, and was ascribed to the increase in the device differential gain. Next, Faugeron et al. [248] demonstrated the lowest internal loss of 2.7 cm$^{-1}$ (on any Qdash material system) with high internal quantum efficiency of 0.81 utilizing an asymmetric-cladding 6-stack Qdash-in-barrier laser. In general, a ridge-waveguide Qdash lasers under the pulsed mode showed a threshold current density of ~4 kA/cm$^2$, slope efficiency 0.32 W/A, and lasing around 1.59 µm. In this material system also ageing test of InAs/InGaAsP Qdash lasers was performed by Resneau et al. [249] at 70 °C and 90 °C with an output power maintained at 10 mW for the 0.9 mm cavity laser. Sudden failure and change in the optical power were not observed from any of the 10 devices tested after 700 h, thus showing the optical quality of these lasers.

### 5.1.2. Multiwavelength Qdash lasers

Exploiting the inherent size dispersion of the self-assembled Qdashes resulting in a broadband gain spectrum is advantageous for comb generation, *i.e.* equally spaced multiwavelength generation with a precise channel separation, attractive for wavelength division multiplexed (WDM) system. Akrout et al. [250] was the first to exploit this feature from a 420 µm long buried ridge-waveguide InAs/InGaAsP FP Qdash laser which provided a flat optical spectrum with ~12 channels and 100 GHz channel spacing, centered at 1.55 µm, as shown in Fig. 37(a), by exploiting the inherent FP mode spacing. The error free (BER $<10^{-9}$) transmission through a single mode fiber over 50 km, utilizing 8 separate on-off keying channels at 10 Gbps, was demonstrated at a power level of ~ −16 dBm (see Fig. 37(b)). A penalty of 1.5 dB was measured compared to a reference single mode external laser source and was attributed to the rise in the RIN level of the filtered modes (~ −110 dB/Hz from 0.1–20 GHz) [251]. This work was further strengthened by M'Sallem et al. [252] demonstrating multiwavelength Qdash laser source

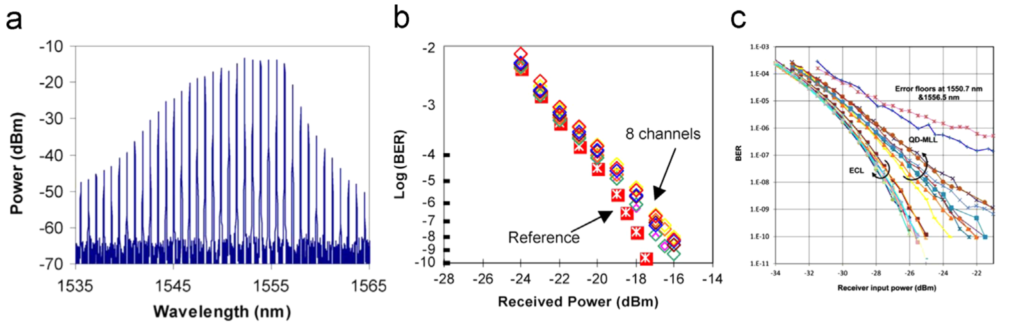


Fig. 37. (a) Optical spectrum of a 100 GHz Qdash mode-locked laser. (b) BER for the Qdash mode-locked laser channels and a reference laser operating at 10 Gbps on-off-keying modulation, and (c) BER versus receiver input power for 11 Qdash mode-locked laser channels, and a reference external cavity laser (ECL) operating at 10 Gbps utilizing the DQPSK modulation scheme. Courtesy of [250,252].

for WDM multicast applications with differential phase-shift keying (DQPSK). An error free transmission of 56 Gbps DQPSK modulation on 9 channels with 100 GHz spacing [corresponding to the International Telecommunication Union (ITU) grid channel spacing] was achieved. An error floor at BER of $10^{-9}$ was obtained with a power penalty from 1.5 to 5 dB, as illustrated in Fig. 37(c). In another study, Nguyen et al. [253] employed Qdash mode-locked laser as a multiwavelength coherent seeding source for colorless WDM-passive optical network (PON) system based on injection locked FP laser diode. An error free transmission at 2.5 Gbps was achieved over 25 km single mode fiber with 16 channels operating in the C-band with 85 GHz spacing. An average BER sensitivity of $10^{-9}$ at receiver input power $-21.9$ dB was reported with a power penalty of $>0.5$ dB. The suitability of Qdash multiwavelength laser for future coherent orthogonal frequency division multiplexing (OFDM) super channel applications was demonstrated by Rosales et al. [254] who assessed the mode coherence between spectral modes of a multiwavelength 890 μm long Qdash laser diode. At 400 mA bias current the group delay and spectral phase of the modes were determined and a group dispersion delay of 1.3 $ps^2$ was calculated. When the modes passed through a 65 m single mode fiber (to compensate the group dispersion delay), mode locking was observed. Next, the single side band OFDM signal, which constituted 74 sub-carriers each encoded with 16-QAM, was modulated into 33 modes of the 48 GHz Qdash laser, with a spectral bandwidth of $\sim$1.5 THz [255]. However, the coherent transmission required an optical linewidth of $<1$ MHz, which require further optimization of the Qdash mode-locked lasers as currently a typical linewidth of about few to tens of MHz is available.

In addition, InAs/InGaAsP Qdash mode-locked lasers were also employed for wavelength tunability applications. For instance, Girault et al. [256] demonstrated a wavelength tunable RZ transmitter by exploiting the flat and wide band lasing emission ($\sim$19 nm $-3$ dB bandwidth) from Qdash lasers centered at 1.55 μm. The wavelength tuning was achieved by selecting a part of the lasing emission using an external optical filter. The potential of the Qdash mode-locked laser technology for the realization of a wavelength tunable transmitter for bit rates of 170 Gbps [257] and $4\times170$ Gbps [258] were reported by Silva et al. In the former report [257], by adjusting the shaping filter frequency, tunability was achieved while in the latter case [258], four channels transmission was tested using the RZ pattern scheme, and an error floor for BER sensitivity of $10^{-8}$ up to 100 km, and a penalty of 1 dB at BER $10^{-9}$ for back-to-back transmission, was demonstrated [259].

### 5.1.3. Broadband Qdash lasers

This new class of semiconductor laser diode source was first demonstrated by our group via exploiting the highly inhomogeneous nature of multi-stack InAs/InGaAlAs Qdash active region. A lasing bandwidth of ~22 nm centered at ~1.64 μm was reported with a lasing emission coverage spanning 76 nm [260], as shown in Fig. 38(a). The 50 × 600 μm$^2$ device exhibited a pulsed threshold current density of 2.6 kA/cm$^2$ (650 A/cm$^2$ per layer), slope efficiency 0.165 W/A, and output power >400 mW. The lasing wavelength of the device was successfully blue-shifted by 100 nm by post-growth bandgap tuning utilizing the IFVD intermixing process. A widened lasing emission coverage of 85 nm with enhanced lasing bandwidth of ~41 nm was reported by Tan et al. [261] from the 50 × 500 μm$^2$ as-cleaved intermixed device which is also shown in Fig. 38(a). Furthermore, improved threshold current density of 2.1 kA/cm$^2$ (525 A/cm$^2$ per layer), slope efficiency 0.423 W/A, and characteristics temperature ($T_0$~57 K from 10 to 60 °C) were achieved. The total output power was ~1 W which could potentially be employed as a highly efficient resonant pumping source for eye-safe Erbium-doped amplifiers and solid state lasers, besides applications in optical telecommunication, sensing and spectroscopy, optical metrology, biomedical imaging, *etc*. [226], as discussed in Section 1. In view of extending the lasing bandwidth, we realized chirped barrier multi-stack Qdash active region (discussed in Section 4.4.) and reported a record ~50 nm lasing bandwidth and lasing emission coverage of ~65 nm from a 2 × 830 μm$^2$ ridge-waveguide laser, illustrated in Fig. 38(b). The device exhibited 3.6 kA/cm$^2$ (900 A/cm$^2$ per layer) threshold current density, slope efficiency 0.36 W/A, and output power >180 mW [8]. Moreover, we also studied the device physics of the chirped Qdash active region and found that the broad emission could be ascribed to the simultaneous emission for dispersive Qdashes [225] at high injection and the non-uniform distribution of carriers in the Qdash active region [262]. Intrinsic dynamics characteristics of these ultra-broadband Qdash lasers were also performed by Chen et al. [263]. A modulation efficiency of ~0.3 to 0.6 GHz/mA$^{0.5}$, and small signal modulation bandwidth of ~3–6 GHz was reported in the temperature range of –40 °C to 40 °C.

To show the viability of this new class of lasers as a single multiwavelength source in WDM system, the broadband lasing spectrum was coupled into a 40-channel array waveguide gratings (AWG), and the lasing emission from each channel was measured [264]. A channel spacing of 100 GHz came from the AWG design rather from the broadband laser cavity length, with each channel exhibiting a −3 dB bandwidth of ~0.4 nm. In addition, by varying the AWG

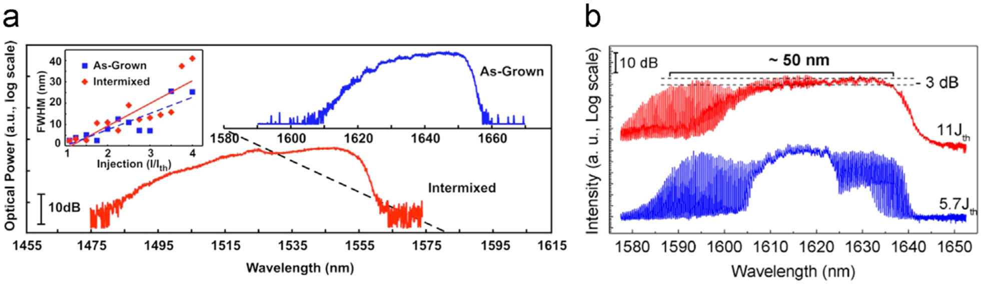


Fig. 38. (a) The wavelength tuned broadband fixed barrier 4 stack InAs/InGaAlAs DaWELL laser from 1.64 μm (as-grown) to 1.54 μm (IFVD intermixed) center wavelength. The lasing coverage increases from 76 to 85 nm after the intermixing process. The inset shows the −3 dB bandwidth of the broadband Qdash laser in accordance to injection. (b) Room temperature lasing spectra of 2 × 830 μm$^2$ chirped barrier thickness 4 stack InAs/InGaAlAs DaWELL laser at different pulsed injection current density. A lasing bandwidth of ~50 nm was measured. Taken from [8,261].

temperature, a red-shift in the optical emission from a single AWG channel with a rate of ~11.1 A°/°C (10 °C to 30 °C) was recorded thus showing the nearly ideal analogous wavelength tuning using a single broadband laser in conjunction with AWG. On the other hand, the discrete longitudinal modes of a FP cavity of the ultra-broadband Qdash lasers [8] wherein the mode spacing is a function of cavity length could also be a potential multi-wavelength source as discussed in Section 5.1.2.

### 5.1.4. Single mode lasers

A thorough investigation on the potential of the Qdash material platform has been carried out by fabricating, and testing single mode lasers and their capabilities. Here we reviewed the reported single mode laser on both the material platform and the achieved dynamic performances.

*5.1.4.1. InAs/InGaAlAs Material System.* Bach et al. [266] initially reported a single mode Qdash laser based on distributed Bragg reflector (DBR) scheme and lasing at 1.54 μm. The 4-stack graded SCH Qdash laser with 300 μm long grating un-pumped section and $2.5 \times 800\ \mu m^2$ gain section showed lasing at 210 mA with output power >30 mW and SMSR >40 dB. From the temperature dependent measurements, a small shift in the lasing wavelength of 0.1 nm/K (20 to 70 °C) was obtained and has been attributed to the temperature dependence of the active region refractive index. This work was soon followed by Kaiser et al. [267] who reported the dynamic properties of laterally coupled DFB gratings based 4 stack InAs/InGaAlAs Qdash laser, as shown in Fig. 39(a). A small signal modulation bandwidth of 7.6 GHz was measured from $3 \times 1000\ \mu m^2$ device under pulsed and CW operations, respectively (see Fig. 39(b)). A slope efficiency of 0.13 W/A, output power >30 mW, 65 mA threshold current under CW operation, and a single peak at 1.51 μm with SMSR of >40 dB was observed. Under pulsed operation, the output power exceeded 110 mW. By employing a deeply etched vertical grating DFB laser using Qdash active medium, Mathwig et al. [268] was able to push the modulation bandwidth up to 5.5 GHz in CW operation. The fabricated 4 stack InAs/InGaAlAs graded SCH devices exhibited a threshold current of 24 mA, SMSR >48 dB, and a wavelength shift of 0.1 nm/K. The tunability of Qdash DFB laser in the wavelength range of 1.5 to 1.9 μm was shown by Kaiser et al. [265]. By employing InGaAs well based DaWELL or graded SCH InAs/InGaAlAs Qdash

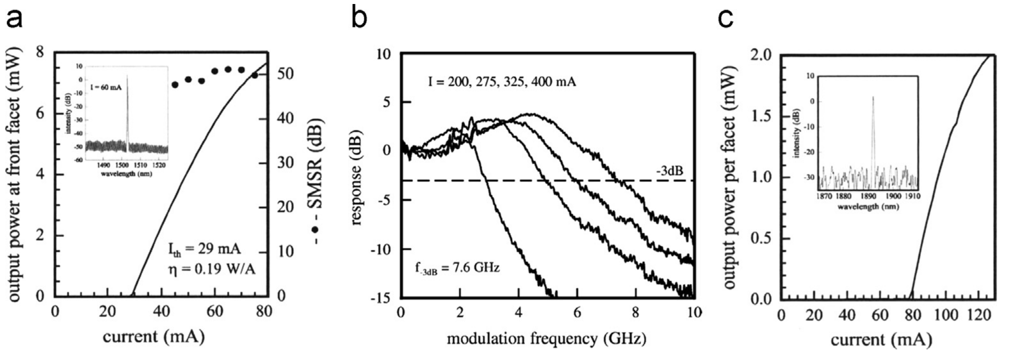


Fig. 39. (a) Output power and SMSR as a function of the drive current of a 600 μm long InAs/InGaAlAs Qdash DFB laser under CW operation at room temperature. (b) Small signal modulation response of a $3 \times 1000\ \mu m^2$ Qdash DFB laser at four different pulsed current values. (c) Light output characteristic and emission spectra of a 1200 μm long InAs DaWELL DFB laser emitting near 1.9 μm at room temperature. Collected from [5,265].

structure, a single mode lasing at 1.9 μm and 1.51 μm, respectively, with corresponding SMSR of $>25$ dB and $>45$ dB were demonstrated, as depicted in Fig. 39(c). In addition, the short wavelength devices showed a slope efficiency of 0.06 W/A, 76 mA threshold current, and output power $>2.0$ mW; while the long wavelength devices showed a slope efficiency of 0.19 W/A, 29 mA threshold current, and output powers $>80$ mW [26]. Subsequently, the comparatively inferior performance of the long wavelength InAs Qdash in InGaAs Qwell DFB lasers was improved by Zeller et al. [269] and Hein et al. [270] who reported single mode lasers at 2.01 μm and 1.89 μm, respectively, at room temperature CW operation. In the former case, a threshold current of 40 mA from $2\times900$ μm$^2$ device showed a high SMSR of $>35$ dB with good reliability properties (maintained CW output power at 60 mA up to 4800 h). The latter case demonstrated a slope efficiency 0.22 W/A with output power $>25$ mW, and SMSR $>35$ dB and temperature coefficient 0.14 nm/K.

*5.1.4.2. InAs/InGaAsP Material System.* A single mode Qdash laser on this material system was demonstrated by Dagens et al. [273], reporting a 10 Gbps direct large signal modulation with a buried ridge-waveguide DFB laser operating at 1.51 μm. The $0.8\times205$ μm$^2$ device was based on 6-stack DaWELL structure grown by MBE–MOCVD techniques, exhibiting 4.8 mA threshold current, 0.3 W/A slope efficiency, and SMSR about 45.5 dB. The small signal modulation bandwidth reached around 6.7 GHz with high modulation efficiency of 1.9 GHz/mA$^{0.5}$ and K-factor 0.43 ns [207]. Furthermore, the device chirp was quantified via above-threshold LEF with measured value of 4.5–6.5. The BER measurements of this direct modulation laser before and after transmission revealed a floor free measurement with $10^{-10}$ sensitivity of $-13$ dBm. In spite of large LEF, after transmission through 2, 8, and 10 km standard fibers (metropolitan distance), floor-free transmission was achieved with 0.8, 4, and 5 dB penalty, respectively. Following this work, utilizing optimized DaWELL active region design and by reducing the Qwell thickness from 8 nm to 6 nm, Dagens et al. [274] reported a $1.0\times240$ μm$^2$ DFB laser with CW threshold current around 4.4 mA, lasing wavelength $\sim1.55$ μm with SMSR 33 dB. The device showed a high modulation efficiency of 1.6 GHz/mA$^{0.5}$ and K-factor 0.3 ns. The large signal modulation of 10 Gbps NRZ PRBS signal on this laser at 35 °C and 85 °C demonstrated floor-free BER at $10^{-10}$ and $-9$ dBm with no penalty both in back-to-back and after 10 km transmission. By reducing the SCH layer thickness in addition to the above optimized DaWELL laser structure, Lelarge et al. [241] further investigated 0.5 mm and 1.0 mm buried ridge-waveguide DFB lasers at 1.54 μm. The SMSR of $\sim40$ dB was obtained with threshold currents around 30 mA and output power $>10$ mW. Direct small signal modulation bandwidth of $\sim10$ GHz was measured with K-factor as low as 0.3 ns and reduced above threshold LEF $<2$. As shown in Fig. 40(a), an error free 10 Gbps transmission was reported up to 65 km with BER sensitivity $10^{-10}$ at $-18$ to $-20$ dBm received power, and 3 dB extinction ratio.

Active region p-doped InAs/InGaAsP Qdash buried ridge-waveguide index coupled DFB laser was also demonstrated in the material system by Zou et al. [271]. The 1 mm long device exhibited a threshold current of 50 mA, slope efficiency 0.26 W/A at 1.54 μm with 40 dB SMSR. A small signal modulation bandwidth of $>10$ GHz was measured from the device at 150 mA CW bias current and is plotted in Fig. 40(b). The corresponding modulation efficiency and above-threshold LEF values were 1.1 GHz/mA$^{0.5}$ and $<2$, respectively [275]. These performance characteristics were further improved very recently by Chimot et al. [272] who reported large signal modulation of 20 Gbps NRZ PRBS error free transmission up to 3 km with BER sensitivity of $10^{-10}$ at $-10$ dBm received power and $>10$ GHz small signal modulation

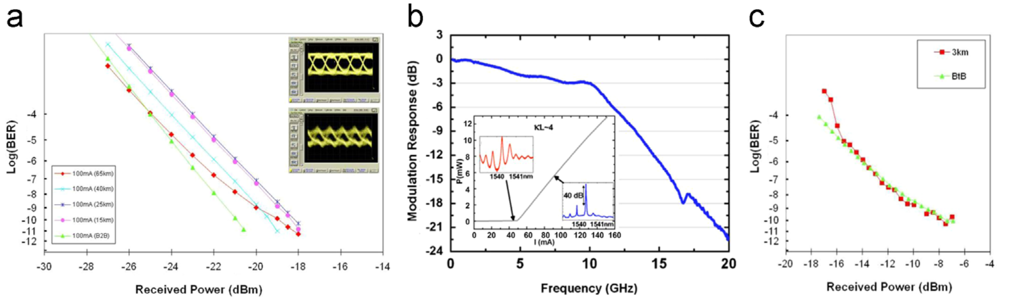

Fig. 40. (a) 10 Gbps BER at 25 °C in back-to-back and after 15, 25, 40 and 65 km single mode fiber transmission. Inset in (a) shows the eye diagrams in back-to-back and after 65 km transmissions. (b) Small signal modulation response of 1000 μm long p-doped buried ridge-waveguide InAs/InGaAsP Qdash DFB laser at 150 mA injection current. Insets in (b) show the corresponding *L–I* characteristic and optical spectrum at 46 mA (left) and 90 mA (right). (c) 20 Gbps BER at 25 °C in back-to-back and after single mode fiber transmission over 3 km, of a 500 μm undoped and optimized active region Qdash DFB laser. Reproduced from [241,271,272].

bandwidth, from the 500 μm buried ridge-waveguide DFB laser at 1.54 μm (see Fig. 40(c)). Besides, the extinction ratio of 3 dB was improved to 6–8 dB by combining the Qdash laser with a commercially available elaton filter.

### 5.1.5. Injection locking/critical feedback of Qdash lasers

The dynamic properties of InAs/InP Qdash lasers were further improved by optical injection under stable locking conditions by Li et al. [276] who showed a three times increase in the small signal modulation bandwidth of the laser. The $4 \times 500\ \mu m^2$ injection locked device exhibited a $-3$ dB bandwidth of 8.7 GHz at $-8.6$ dBm injected power under zero detuning compared to 3.4 GHz for the free-running case. In another study, a value of 11.7 GHz was observed at 3.5 dBm injected power in the master laser by Naderi et al. [277] under stable locking conditions with 30 dB SMSR. This corresponded to a threefold improvement relative to the free-running case. The LEF was also measured above threshold and varied from 1 at threshold to 11 at 90 mA, attributed to the carrier density being unclamped at threshold which is due to the inhomogeneous gain broadening in Qdashes. Recently, an impressive 16.5 GHz $-3$ dB small signal modulation bandwidth was reported by Lester et al. [278] by slightly blue shifted (1.535 μm) injection locked Qdash laser under strong optical injection of 9.3 dB. This was approximately four times bandwidth enhancement compared to the free-running 4.5 GHz at 1.565 μm. In addition, remarkable values of near zero above-threshold LEF and $5.9 \times 10^{-14}\ cm^{-2}$ differential gain were obtained under these conditions. This is highly attractive as packaged RF photonic transmitter in high-frequency optical fiber links [278,279]. A detailed dynamic study of an injection locked Qdash laser was carried out by Pochet et al. [280,281] at zero detuning, and it was found that Qdash laser's large damping rate, gain compression coefficient, and sufficiently small LEF yielded period-one and stable locking operating conditions at bias currents close to threshold. In fact, under period-one state, a tunable photonic oscillator based on optical-injection Qdash laser was demonstrated by varying the injection field ratio from 4.9 GHz to 45.4 GHz [282]. A tunable resonance frequency from 4.9 GHz to 8.3 GHz was reported.

Till now, the beneficial effects of the optical feedback were discussed wherein a very weak or a very strong optical injection was employed to achieve improved performance characteristics of Qdash lasers. However, optical feedback on the other hand results in laser instability causing collapse of the coherence time and hence broadening of the lasing spectrum, in addition to degradation in the LEF as well as the BER. The tolerance to the optical feedback of Qdash lasers was first studied by Azouigui et al. [236] who demonstrated an onset of coherence collapse from $\sim -41$ to $-27$ dB on increasing the current injection of 205 μm long InAs/InGaAsP Qdash DFB laser from 10 to 100 mA, based on optical spectrum and RIN static characteristics. In terms of dynamic characteristics at 10 Gbps PRBS transmission signal operating at 30 mA, a floor-free operation (BER sensitivity $10^{-10}$ at $\sim -13.5$ dBm) was achieved at $-32$ dB (correspond to $-24$ dB return loss and $\sim$4.5 LEF ) and the performance degraded above this value. The onset of coherence collapse was further improved on a 600 μm FP Qdash laser with values ranging from $-29$ to $-21$ dB (as a function of current) and hence $-19$ dB return loss, thus complying with the requirement of IEEE 802.3ae 10 Gbps Ethernet standard [237]. A systematic investigation of the external feedback effect on several Qdash lasers exhibiting different LEF values ($\sim$3.6 to $\sim$10.7) and damping factors ($\sim$9 to $\sim$5.2) were also performed. An onset of coherence collapse as good as $> -18$ dB was achieved with linear dependence on the drive current, and thus highlighted the better performance from high differential gain devices [283]. In addition, the effect of temperature and cavity length was also investigated by Azouigui et al. [284] and it was found that higher optical feedback could be achieved from temperature insensitive differential gain laser and/or longer cavity devices. In general, these features were similar to the bulk or Qwell lasers but with improved critical feedback level, and both InAs/InP Qdots and Qdash lasers with similar differential gain and cavity length exhibited similar onset of coherence collapse. In contrast, Grillot et al. [285] found a decrease in the critical feedback level with increasing current injection from a 500 μm long ridge-waveguide Qdash laser; an unconventional trend compared to the Qwell lasers. This was attributed to the contributions of the ES coupled to the non-linear effects which caused non-linear increase in the GS above-threshold LEF from $\sim$1 to $\sim$14 on increasing current injection, thus emerging as a key parameter for designing feedback-resistant lasers [286].

### *5.2. InAs/InP Qdash mode-locked lasers*

The broad stimulated spectrum width of the InAs/InP Qdash lasers showing sub-picosecond pusle generation capability has also been the centre of attraction since a decade and demonstrated impressive results in terms of pulse width, repetition frequency and particularly RF spectrum bandwidth which was observed to be from $<1$ kHz up to 600 kHz [207,227]. However, in general, reduction of dimenstionality from zero dimensional Qdots to quasi-zero dimentional Qdashes has no significant impact on the mode locking characteritics of InAs/InP nanostructure lasers. This observation has been deduced based on our discussion on InAs/InP Qdots mode-locked lasers (Section 3.2) and comparison with the achievments in InAs/InP Qdash mode-locked lasers summarized in this section and plotted in Fig. 2(b).

#### *5.2.1. Two-section*

Passive mode locking employing classical two-section InAs/InGaAsP Qdash laser with one gain and one absorber section was first demonstrated by Gosset et al. [287] who measured 47 kHz RF linewidth from a 6-stack Qdash laser with 940 μm gain and 180 μm absorber sections. A pulsation frequency of 43.6 GHz was measured at 169 mA CW current and with no significant effect of applied bias on the absorber section. This was attributed to the FWM phenomenon in the gain section to be dominant compared to the effect of the absorber section. Later, Merghem et al. [288] investigated a 2.4 mm Qdash mode-locked laser with absorber/gain length ratio of 4% which corresponds to a repetition frequency of 17 GHz at 1.58 μm. Pulse widths ranging from 3 to 14 ps (after deconvolution), and RF linewidth values from 250 kHz to 3.5 MHz were observed for a wide operating regime (current injection from 60 to 160 mA and reverse bias voltage from −5 to 0 V). It was shown that when the mode-locked laser was subjected to optical feedback at approximately −22 dB, the mode-beating linewidth substantially narrowed to <1.0 kHz to 500 kHz range with slight increase in the pulse duration with a smallest value of ~500 Hz at current values 100 to 130 mA compared to 370 kHz without the optical feedback. Later, Dontabactouny et al. [289] studied the phase noise and timing jitter on a 10 GHz two section 3.95 mm (0.13 mm absorber section) long 5 stacks InAs/InGaAsP Qdash laser emitting at 1.59 μm. Highly chirped pulses ranging from 8 to 14 ps were observed at a fixed bias current and reverse bias voltage and by changing the position of a 1 nm bandwidth filter centered at 1.6 μm. By employing 545 m single mode optical fiber for dispersion compensation, pulses in picosecond range were reported with the smallest value 975 fs after deconvolution. Phase noise measurements revealed values −80 dBc/Hz at 100 kHz, which reduced down to −140 dBc/Hz at 100 MHz, while an average timing jitter as low as 800 fs was reported. Similar mode locking characteristics on 1.0 mm device (4% absorber length) corresponding to 41 GHz pulse repetition rate was also investigated which again exhibited strongly chirped pulses. Pulse duration of ~18 ps (raw pulses) with ~1 MHz RF linewidth was observed and when passed through a 60 m single mode fiber decreased to ~7 ps with ~100 kHz mode-beating linewidth.

A systematic passive mode locking investigation at repetition rates of 20, 48 and 95 GHz from 1200 μm (long), 890 μm (medium) and 450 μm (short) length (10% absorber section) InAs/InGaAsP Qdash lasers were reported by Rosales et al. [251,290,291] with 95 GHz repetition value being the highest value ever reported on a monolithic two-section device in any InAs/InP Qdash material system. The results are summarized in Fig. 41(a)–(c). Stable mode locking regime in all three lasers were discussed in detail with minimum achievable pulse durations ~1.4, ~2.5 and ~1.6 ps without deconvolution, and time bandwidth product of 1.7, 1.5 and 1.4, for the long, medium, and short cavity lasers, respectively. These values were obtained for low drive currents at a reasonably high reverse bias value. Noise trends were also assessed by RF linewidth measurement showing small values of ~100 kHz from the medium cavity laser and ~20 kHz from the long and short cavity lasers. Measurements of group delay (GD) and group delay dispersion (GDD) were also performed by Rosales et al. [292] on a 48 GHz, 890 μm long optimized Qdash laser with 60 μm absorber section. Deconvolved pulses down to 1.2 ps were observed after compensation of the GDD and 1.7 time bandwidth product. Similar results were also achieved from two-section InAs/InGaAlAs Qdash laser by Lin et al. [293] who

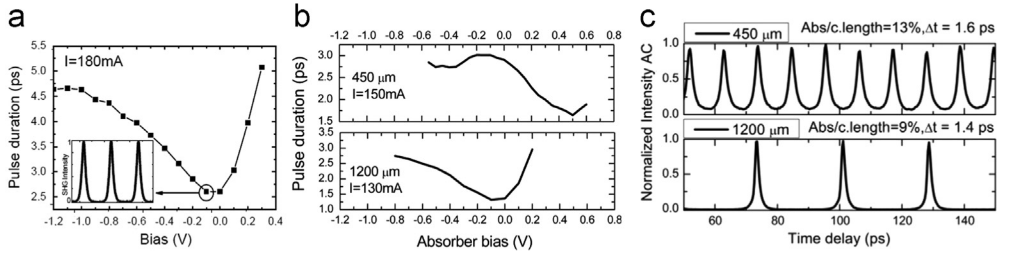


Fig. 41. (a) Pulse duration as a function of reverse bias at a fixed drive current of 180 mA for $1.5 \times 890\ \mu m^2$ InAs/InGaAsP Qdash mode-locked laser with 90 μm absorber section and yielding a repetition rate of 48 GHz (shown in the inset). (b) The effect of reverse bias on the pulse width for the 450 μm and 1200 μm long high gain InAs/InGaAsP Qdash mode-locked laser and (c) the corresponding autocorrelation pulse train. Taken from [290,291].

demonstrated 12.3 and 18.4 GHz repetition rates from 3.4 and 2.3 mm long devices, respectively, emitting at 1.59 μm. In general, lower average output powers due to low drive current besides the inability to attain wider spectral bandwidth render the two-section mode-locked laser applications compared to the single section device

*5.2.2. Self-pulsation*

Single section passive mode locking is highly attractive compared to the two-section mode locking in terms of attainable output power and pulse width, and has been actively researched since a decade with superior performances. As discussed in Section 3.2.2, a 45 GHz CW mode locking from monosection InAs/InP Qdot/Qdash laser was first demonstrated by Renaudier et al. [120]. Following this report was the detailed investigation by Gosset et al. [287] who demonstrated 134 GHz pulse generation from 340 μm long 6-stack InAs/InGaAsP DaWELL laser under CW operation. The 1.56 μm device exhibited deconvolved sub-picosecond pulse width of 800 fs without any pulse compression scheme and 0.46 time bandwidth product. RF spectral linewidth of 50 kHz was measured from the 990 μm device exhibiting 42.2 GHz pulse repetition rate and 2 ps auto-correlated pulses. The ability to reduce the mode beating linewidth to 2 kHz by an inclusion of an optical filter was demonstrated by Shen et al. [294] on a 2.5 mm long, 17 GHz Qdash mode-locked laser, and further showed that reduction in the optical confinement factor also decreased the mode beating linewidth [295]. In general, these high performance characteristics were attributed to the reduction in the active region dimensionality resulting in reduced interaction of the optical mode with the amplified spontaneous emission, and large population inversion, which reduces the phase noise, apart from FWM process [251,296]. On the other hand, Akrout et al. [297] exploited the external cavity length based high quality factor for initial phase noise reduction in a 30.3 GHz InAs/InGaAsP/InP Qdash self-pulsating mode-locked laser. The auto-optical feedback loop resulted in the reduction of the mode-beating linewidth (phase noise) from 30 kHz (−75 dBc/Hz) to mere 200 Hz (−105 dBc/Hz).

A systematic investigation of timing jitter on 9-stack InAs/InGaAsP Qdash-in-barrier laser was performed by Tourrenc et al. [298] on a 40 GHz mode-locked laser exhibiting ~20 dB extinction ratio, 3.71 ps deconvolved pulse width and 240 kHz RF linewidth. A value of 860 fs was reported in the 1 MHz to 20 MHz range and an optimized RF linewidth of 30 kHz was also achieved at 242 mA with an estimated reduction in the timing jitter to 280 fs. These performance parameters were further improved by Latkowski et al. [299] who successfully measured 720 fs pulse width from a 39.8 GHz Qdash mode-locked laser by passing through a 450 m single mode dispersion compensated fiber. Furthermore, as depicted in Fig. 42(a), mode beating linewidth of 10 to 25 kHz was measured regardless of the bias current value and the timing jitter varied from 350 fs to 150 fs with peak power varying from 40 mW to 140 mW [300,301]. The influence of the bias current and the filter bandwidth on the pulses were also performed which revealed decrease in the pulse width either by increasing filter bandwidth or the bias current. This was related to locking of larger number of longitudinal modes and a better respective phase locking at higher injection [302,303]. Further improvement of the 40 GHz mode-locked laser characteristics was achieved by Maldonado-Basilio et al. [304] who reported best ever 8 Hz RF linewidth and 64 fs timing jitter by subjecting the laser to an optical injection by its fourth harmonic *i.e.* 10 GHz pulses at ~1.55 μm, as shown in Fig. 42(b). In terms of highest repetition rate, Merghem et al. [246] reported a record 346 GHz pulse generation (see Fig. 42(c)) using a passively mode-locked 120 μm long Qdash laser emitting ~560 fs deconvolved pulses with 20 mW peak power and 9 dB extinction ratio. On the other hand, a 170 μm 6 stacks Qdash

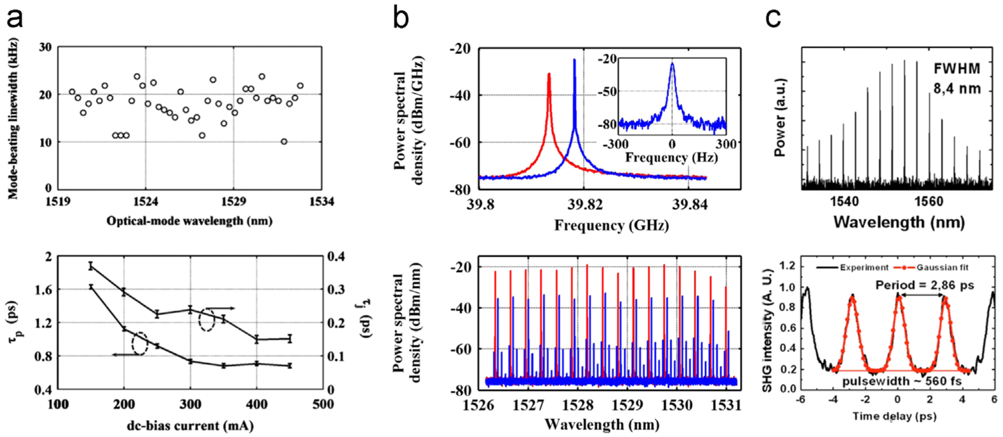


Fig. 42. (a) Typical mode-beating associated with each pair of optical modes as a function of the filter central wavelength (top) of the 1000 μm long 40 GHz InAs/InGaAsP Qdash mode-locked laser at 350 mA. The corresponding device pulse width and timing jitter associated with the optically generated pulses as a function of CW current (bottom). (b) Beat-tones (top) and optical spectrum (bottom) for the 1000 μm long 40 GHz InAs/InGaAsP Qdash mode-locked laser under free-running (red trace) and under the injection of 10 GHz optical pulses (blue trace), at bias current of 100 mA. Inset illustrates the beat-tone under optical injection recorded with a 10 Hz resolution showing 8 Hz linewidth. (c) Optical spectrum (top) and autocorrelation trace (bottom) of 120 μm long, 345 GHz, InAs/InGaAsP Qdash mode-locked laser at 217 mA. Courtesy of [246,301,304] (For interpretation of the references to color in this figure legend, the reader is referred to the web version of this article.)

mode-locked laser exhibited 870 fs pulses at 245 GHz with 100 mW peak power and 7 dB extinction ratio.

Instead of the typical stepped-heterodyne technique for pulse characterization, Calo et al. [305] employed the second-harmonic generation frequency resolved optical gating (SHG-FROG) technique for the investigation of high gain $\sim 50\ \mathrm{cm}^{-1}$, 1.56 μm, 9-stack InAs/InGaAsP dash-in-barrier laser. The 890 μm long device exhibited a repetition frequency of ~48 GHz under CW operation. Highly chirped pulses broadened by positive GDD were compressed by a single mode fiber to achieve 423 fs pulses with ~100 mW peak power at 300 mA bias [306]. The value was found to reduce at 400 mA injection reaching a 374 fs which is the best value reported on an InAs/InP Qdash material system, and is shown in Fig. 43(a). By developing an asymmetrical cladding Qdash laser with extremely small loss, Faugeron et al. [248] reported small RF linewidth of 300 Hz from 4.4 GHz 10 mm long single section passive Qdash mode-locked laser. Furthermore, a record high peak power of 18 W was demonstrated from 4.3 mm long 10 GHz mode-locked laser generating 750 fs deconvolved pulses after pulse compression via 570 m single mode fiber (compensating 9.3 ps/nm linear GD). An improved phase noise below −100 dB/Hz at an offset frequency of 1 kHz and RF harmonics up to 120 GHz was also demonstrated by active mode locking the 4.3 mm long Qdash laser via electrical ~10 GHz RF signal injection [211]. Very recently, an integration of 6 stacks InAs/InGaAsP Qdash mode-locked laser in DBR configuration and with an integrated SOA was demonstrated by Joshi et al. [307]. By careful control of the DBR gratings an RF linewidth down to 30 kHz was reported from the 40 GHz $1.5 \times 1000\ \mu\mathrm{m}^2$ device at a CW injection of 310 mA. It was shown that the linewidth was maintained with and without biasing the SOA, except the regions of mode locking were changed. This is ascribed to the interaction of the laser emission with the amplified spontaneous emission of the SOA. A pulse width of 1.4 ps was obtained after chirp

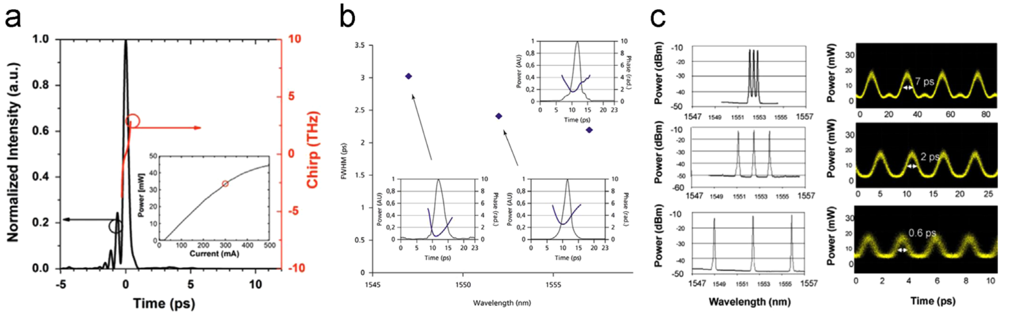


Fig. 43. (a) Intensity and chirp profile of pulse generated by a 890 μm long single-section Qdash mode-locked laser for an injection current of 300 mA, after dispersion compensation using 66 m of single mode fiber. The inset shows the *L–I* characteristic of the laser. (b) Pulse width as a function of the tunable optical filter center wavelength for an actively mode-locked Qdash laser. Pulse shape and chirp are shown in the inset. (c) Tunable pulse generation at three different frequencies: 42.7 GHz; 170.8 GHz, and 427 GHz, from a single 42.7 Qdash actively mode-locked laser and a tunable spectral filter. Adapted from [227,259,306].

compensation with 120 m single mode fiber [308]. Besides, the capability of using SOA as modulator was also demonstrated by reporting a floor free BER sensitivity of $10^{-10}$ at $-34$ dBm via on-off keying modulation at 5 Gbps [309].

The phase correlation of the adjacent longitudinal modes in a passively mode-locked Qdash laser was investigated by Duan et al. [227,310] by measuring the RF linewidth of couples of modes at three different wavelength regime selected by an optical filter. A fixed linewidth of 15 kHz was obtained for all the three groups and was same as the spectral linewidth of the entire optical spectra, thus affirming that the relative phases of the adjacent modes have the same phase noise characteristics [207]. Alternatively, Rosales et al. [292,311] and others [312–314] shed light on the spectral phase profile of the InAs/InGaAsP Qdash mode-locked lasers which determine the pulse shape. In the former report, employing a ~48 GHz (~890 μm) and 23 GHz (1820 μm) InAs/InGaAsP Qdash mode-locked laser exhibiting corresponding minimum values of 20 kHz and 100 kHz RF linewidth, GD and spectral phase of the electric field were determined and GDD values were calculated to be 1.3 and 3.0 ps$^2$, respectively. No pulse generation was observed without the dispersion compensation by single mode fibers. The shorter cavity yielded 600 fs pulses with 40 mW average power (~1 W peak power) emitting at ~1.55 μm while the longer cavity locked at 700 fs pulses.

Tunable pulse generation utilizing Qdash active mode-locked laser via actively mode-locking through the electrical modulation at 42.7 GHz was demonstrated by employing a tunable optical filter up to 16 nm over the laser emission spectrum with relatively fixed pulse width of $2.4 \pm 0.4$ ps and time bandwidth product $0.48 \pm 0.09$ at 42.7 GHz [295,310], as shown in Fig. 43(b). In addition, by inclusion of pulse compression approach via single mode fiber, a pulse width reduction down to 1.1 ps was obtained by Akrout et al. [315]. On the other hand, Costa-e-Silva et al. [257,259] showed that a tunable pulse generation at 42.7 GHz, 170.8 GHz, and 427 GHz with pulse widths 7, 2, 0.6 ps, respectively, as shown in Fig. 43(c), could be achieved by actively mode-locked 42.7 GHz Qdash laser by an external RZ 42.7 GHz optical clock signal and a tunable spectral filter.

As noted in this section, optical injection could also be utilized to reduce the phase noise, and hence achieve narrow RF linewidth and low timing jitter in Qdash mode-locked lasers. In continuation, Maldonado-Basilio et al. [316] further investigated the optical locking dynamics on the single section Qdash laser. Alternatively, Sooudi et al. [317] demonstrated a higher intensity ~15 dB and ~160 kHz linewidth RF spectrum under CW injection locking (at negative detuning) compared to the free-running ~20 GHz Qdash InAs/InGaAsP self-mode-locked laser. This was attributed to the supermode noise reduction of the laser which led to amplification of mode-locked peak. In another study, tunable harmonic mode locking via optical injection in Qdash laser to generate microwave pulses with twice the self-mode-locked frequency was demonstrated [318]. Double locking with simultaneous optical injection and optical feedback was investigated by Sooudi et al. and showed two time reduction in the time bandwidth product, and two orders of magnitude reduction in the RF linewidth [319].

#### 5.2.3. *Selected system-level applications*

Because of the small timing jitter, thanks to the low phase noise, InAs/InP Qdash mode-locked laser have found profound interest in many applications requiring narrow mode-beating linewidth like optical-signal processing, optoelectronic oscillators [282,297,320], frequency comb generation, WDM system, *etc*. Here, we briefly review some of these applications, and direct the readers to existing review papers for further information [227,251].

Truly all optical clock recovery at 40 GHz employing Qdash mode-locked laser was first demonstrated by Renaudier et al. [321,322] with jitter characteristics in compliant with the ITU recommendations. This was followed by a series of experimental demonstrations of the wavelength tunability [323], all optical frequency down conversion [259], and retiming, reshaping, and re-amplifying (3 R) generators at 40 Gbps [324]. Clock recovery utilizing different modulation formats such as RZ-OOK [325], NRZ- and RZ-DPSK [325], burst operation [326], as well as subharmonic 40 GHz clock recovery from 40, 80 [327–329], 160 [330,331], and 320 Gbps [332,333] has also been demonstrated.

The potential of Qdash mode-locked lasers for millimeter tone generation stems from the self-mode locking capability without any external oscillator and reduced signal linewidth. In addition, a direct modulation of the laser should be possible without assistance from an external modulator [334,335]. This radio-over-fiber technique was demonstrated on the 60 GHz system for broadband wireless services using 1.5 Gbps OOK and 3.03 Gbps OFDM QPSK modulation schemes by Lecoche et al. [336] with floor free BER measurements and error vector magnitude (EVM) 19% for a signal-to-noise ratio of 21.5 dB which is less than the criterion for successful detection (23%) [251]. The advantages of 60 GHz Qdash mode-locked laser were further assessed by in-door and out-door 5 Gbps operation experiments and shown an error floor of $10^{-7}$ [337] and further improvement of the EVM to ~11% with high single-to-noise-ratio of 25 dB [338].

Frequency comb generation is another viable application exploiting the unique features of InAs/InP Qdash mode-locked laser. This has been demonstrated in various reports [255,339,340]. Moreover, improvements to noise reduction [341] and stability tests [342] were also recently performed. Besides, the broad lasing multi-longitudinal modes profile of the Qdash laser was itself exploited for multi-channel WDM system demonstration, as discussed in Section 5.1.2.

### 5.3. *InAs/InP Qdash semiconductor optical amplifiers*

InAs/InP Qdash material which exhibits broad gain profile has been employed as SOA. As seen in InAs/InP Qdot SOA, Qdash SOA also showed fast index and gain dynamics, and the capability of amplifying multiple wavelengths without any crosstalk. A systematic review on the advancements of Qdash SOA has been discussed below.

### 5.3.1. Broad gain

Depolyment of multi-stack self-assembled Qdash layers as an active region for SOA was first studied by Bilenca et al. [343] on the InAs/InGaAlAs material system. The anti-relection coated $4.5 \times 2100\ \mu m^2$ device exhibited a broad gain $-3$ dB bandwidth of $>50$ nm centered at $\sim 1.53\ \mu m$. A linear increase in the chip gain with 1.5 dB uncertainty was observed on increasing the injection current and reaching a maximum 12 dB at 150 mA. Later, Reithmaier et al. demonstrated a 120 nm SOA wavelength band exhibiting $>10$ dB chip gain with peak value reaching 25 dB at CW current of 300 mA, from a $3.5 \times 2500\ \mu m^2$ 4-stack Qdash active region. A large flat amplification characteritics over large input range was observed with a saturation output power of 18 dBm at 0 dBm input power and extracted 3 dB saturation output power range froms 16 dBm at 1.537 μm to 18 dBm at 1.585 μm [26,344], as shown in Fig. 44(a). On the InAs/InGaAsP material system, Lelarge et al. [207,245] reported a $-3$ dB gain bandwidth of 50 nm and a total amplification bandwidth (gain $>0$ dB) of 210 nm from a 1500 μm long Qdash SOA with 7° tilted waveguide and anti-reflection coated. Analysis of the chip gain and noise figure against the injection current for the transverse electric polarization showed an increasing chip gain and reaching a maximum 20 dB at 300 mA while the noise figure decreased to 6 dB which is the lowest value reported on Qdash SOA platform. The performance was further improved with gain up to 30 dB at 350 mA CW current by utilization of an optimized DaWELL strucuture [345]. Looking at the recent encouraging demonstrations of large bandiwdth and peak gain from the chirped Qdash active region structures discussed in Section 4.4, we believe that there is still room of Qdash SOA performance improvement.

### 5.3.2. Ultrafast gain and index dynamics

Gain and phase changes of a weak probe pulse following a strong pump pulse in the InAs/InGaAlAs Qdash SOA was reported by van der Poel et al. [346]. By employing the degenerate heterodyne pump-probe setup (with 150 fs pulse width), the dynamics of the SOA were measured at 1.523 μm (gain maximum) probe pulse. As shown in Fig. 44(b), at 150 mA bias, the SOA reacted very fast with $<1$ ps rise time followed by a recovery with two time components due to bi-exponential fit; first being a fast component of 1.6 ps and second a slower component of 130 ps. While the former time component was ascribed to the combination of carrier relaxation (high lying dash carrier relaxes into the active states) and carrier capture from barrier to the dash, the latter was attributed to the recovery of the total carrier density of the device, *i.e.* the effective carrier lifetime. Similar results were also reported by Lunnemann et al. [347] and

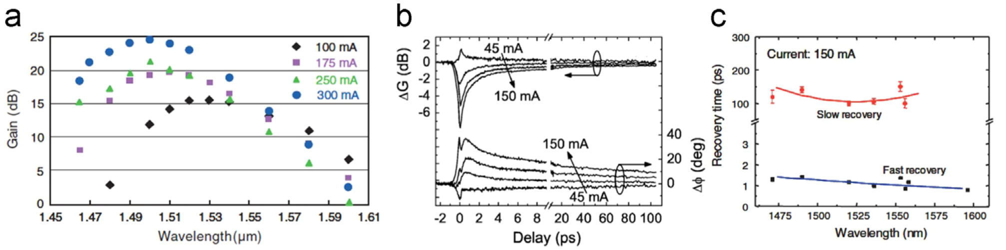


Fig. 44. (a) Optical gain spectra of a $3.5 \times 2500\ \mu m^2$ long and Qdash SOA at different drive currents. A maximum chip gain of 25 dB was obtained at a drive current of 300 mA. (b) Time resolved gain and phase recovery of Qdash SOA for the bias currents of 45, 75, 100, and 150 mA at a fixed operating wavelength of 1523 nm. (c) Characteristic gain recovery times of Qdash SOA as function of wavelength at a fixed bias of 150 mA. The lines are guides to the eyes. Collected from [26,346].

analogous to the InAs/InP Qdots system discussed in Section. 3.3.2. A weak dependence of the gain recovery time on the bias current and the wavelength was observed (see Fig. 44(c)), attributed to the dominating phonon scattering and inhomogeneous broadening of the Qdashes. The phase dynamics, on the other hand, showed complex and different characteristics but along the same time scale as the gain recovery except that the fast component of the recovery was smaller relative to the slow component. This was related to the strong effect on the refractive index by changes in the carrier population in Qdash states, wetting layers, and/or barrier region where as only the population of the active states affects the gain [26,348]. However, the phase response compared to the Qdots counterpart was much larger which suggested larger LEF in the present case. In fact, Zilkie et al. [166] measured this value to be 5–12 with increasing bias current, on the InAs/InGaAlAs Qdash SOA. Moreover, ultrafast dynamics of 0.1–0.5 ps and 1.2–2.0 ps was found in the case of Qdash SOA on fitting the short lived dynamics with double exponential, and was attributed to the spectral hole burning and carrier heating, respectively [165]. In general, the gain and phase dynamics recovery were in between Qdots and Qwell SOA counterpart, but with a potential of reaching ultra-broad gain profile.

A further investigation on the Qdash SOA dynamics by Capua et al. [349] revealed a nearly instantaneous gain response at energies far above and below the pulse energy on a multi-wavelength pump-probe setup with 150 fs resolution. This was shown by the transmission of probe at 1.57 μm and 1.53 μm which was 20 nm away from the gain maximum and was attributed to combination of complex non-linear processes such as two-photon absorption, inhomogeneity and the Qwire-like density of states. The condition to achieve this response was also investigated subsequently [350] and found that only under high optical and electrical excitations this was possible. Moreover, the cross gain saturation response at 1.52 μm and 1.6 μm, with excitation at 1.55 μm under low optical and electrical excitation, showed that the recovery at the short wavelength followed the bi-exponential fit with time constants 0.5 ps and 33 ps while the long wavelength followed single exponential fit of 1.54 ps [351]. This was attributed to the larger role played by the fast interband carrier relaxation, similar to the observation by van der Poel et al. [346]. The noise properties based on coherent spectral hole measurement (since it is caused by the FWM like non linear interration between the signal and the noise) of InAs/InP Qdash nanostructure based SOA was also investigated by Hadaas et al. [344] who predicted a wide coherent spectral hole of about 0.5–1 THz, broader by one order of magnitude compared to the Qwell SOA counterpart [5], and later experimentally demonstrated by Capua et al. [352] with value around 500–600 GHz.

### *5.3.3. High speed amplification and signal processing*

The unique characteristics of the Qdash SOA which are dictated by the inhomogeneously broadened gain profile and the fast gain and phase recovery dynamics with impressive demonstrations of single and multiple channel amplification and procesing makes them potential cahdidates in future high speed optical communicatio. In addition, the low noise properties of these nanostructures stands out which are crucial in a SOA perofrmance. Here we reviewed some of these achievements.

Single signal processing *via* wavelength conversion based on FWM on Qdash SOA was investigated by Bilenca et al. [343] who utilized a pump signal fixed at 1.542 μm and tunable frequency ($\pm$1000 GHz) probe signal. The conversion efficiency of the conjugate FWM product for both the positive and negative detuning was measured and found to be same in shape and was attributed to the reduction in the LEF [353,354]. A 40 ps probe signal at a repetition rate of 500 MHz and an average input power of $-7$ dBm was detuned from the CW pump by 6.2 nm with large signal-to-noise ratio. On the other hand, cross gain modulation was demonstrated by 2.5 Gbps NRZ data at a large detuning of 50 nm (7.5 THz) within the inhomogeneously broadened gain spectrum of ~1.52 μm InAs/InGaAlAs Qdash SOA [355]. The converted pulses possessed high signal-to-noise ratio and the measured BER at the Qdash SOA output of the signals at the original and converted wavelength were identical (sensitivy $10^{-9}$ at −26 dBm) indicative of efficient conversion process. The results are shown in Fig. 45(a) and (b). However, wide cross gain modulation bandwidth could be achieved with the expense of speed due to slow gain recovery (slower carrier escape time at shorter wavelengths due to raised energy levels of wetting layers or barriers at shorter wavelength side) [356] and intradash coupling. In other words, the carrier transport time between the spatially separated Qdashes would be too long to follow the faster singals [5].

The cross talk between different wavelengths due to coupling among the Qdash ensembles outside the homogeneous linewidth via wetting layers was readily exploited in the ultra-broadband Qdash SOA by simultaneous signal processing and amplification of multiple wavelength channels. For instance, simultaneous amplification of 8 different wavelengths at the same time was performed by Alizon et al. [357] utilizing a single Qdash SOA. Each of the channels were coupled into a fiber, modulated by 10 Gbps PRBS data stream,and then into the SOA. All the input signal powers were at −20 dBm and after amplification to a maximum of ~0 dBm. BER measurements of all the 8 channels, as shown in Fig. 45(c), behaved very similar with no cross talk and penalty after amplification and resembled that of the receiver with sensitivity $10^{-9}$ at −19 dB [26]. In addition, high speed transmission experiment by time domain multiplexing four 10 Gbps singals (one 40 Gbps bit stream) was also performed. A clear open eye diagram of the amplified signal with significantly improved quality factor was observed from the low amplification power to deep sturation at 0.5 dBm input power, indicative of the capability of Qdash SOA for signal recovery at high speeds [5,352].

A systematic study on the cross saturation dynamics in the InAs/InGaAlAs Qdash SOA was studied by Alizon et al. [359] by amplifying two wavelength data streams at 10 Gbps (signal and inteference) utilizing the optical amplifier and measuring the BER. It was found that for small

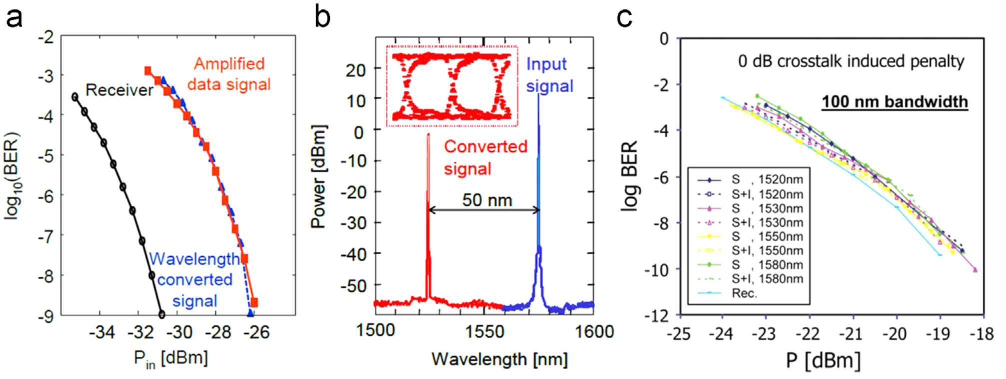


Fig. 45. (a) Cross gain modulation experiments based BER measurements of 2.5 Gbps PRBS data at a 50 nm detuning. (b) The corresponding spectrum of modulated input signal (right side in blue) and wavelength converted output signal (left side in red). The eye-diagram of a 2.5 Gbps wavelength converted PRBS signal is shown in the inset. (c) BER as a function of the input power for 8 channels simultaneously amplified by Qdash SOA. No cross talk is observed at a data rate of 10 Gbps for each channel. Taken from [5,358] (For interpretation of the references to color in this figure legend, the reader is referred to the web version of this article.)

(large) detuning of 4 nm (40 nm), the cross saturation was determined by the dynamics of homogeneously (inhomogeneously) broadened gain region. The large detuning imposed a 2 dB penalty at a BER $10^{-9}$ for singal wavelength < inteference wavelenth and no penalty in the vice versa case was observed, ascribed to the large cross-saturation effects on the short wavelength side of the gain peak. Additional investigation at low bit rates (2 Gbps) revealed that the cross-saturaton between the channels depends on the detuning, bit rate, and spectral placement. Recently, the versatility of highly inhomogneous Qdash SOA was re-affirmed by Capua et al. [360] who demonstrated simulataneous wavelength conversion with no cross-talk on two independent, spectrally separated by 30 nm, 10 Gbps channel via FWM process and each accompanied by a CW pump. Moreover, the effect of FWM and cross talk were examined by observation of the converted 10 Gbps signal at one channel and measurements of its BER performance in the presence of second channel. A BER of $6\times10^{-9}$ at $-4$ dBm received power was measured on both the channels indicative of increased optical power requirement for detection.

The potential of InAs/InP Qdash SOA for fast light with varible opitcal delays utilizing the FWM process was also demonstrated by Martinez et al. [361] on a microwave frequency modulated signal which underwent group index variation leading to a maximum optical tunable delay up to ~136 ps (~55) at 250 MHz (2 GHz) on changing the bias current. This was attributed to the enhanced degenerate FWM efficieny process.

### 5.4. InAs/InP Qdash superluminescent diodes

Interest in C–L–U band SLDs has been growing owing to their broader applications in cross-disciplinary fields besides optical communications, as discussed in Sections 1 and 3.4. Currently, this wavelength window is dominated by the InAsGaAsP/InP Qwell active region platform based diodes which are already commercialized. The drive to attain comparatively flat-top emission and highly efficient devices was rather limited in Qwell active region, and hence paved the way for exploring self-assembled InAs Qdots/Qdashes on InP platform [362]. In this regard, our group was the first to demonstrate room temperature broad emission from InAs/InGaAlAs/InP Qdash SLD spanning ~110 nm bandwidth with output power ~1.5 mW, as shown in Fig. 46(a). The device configuration was based on $50\times1000\ \mu m^2$ gain section with 1000 μm integrated photon absorber. The corresponding emission spectra exhibited < 0.3 dB spectral ripple, and measured 12.3 μm coherence length in air [363]. The latter measurement setup was based on optical fiber coupled Michelson interferometer system. Recently, we investigated the SLD characteristics on the chirped barrier thickness Qdash active region structure under both pulsed and CW operations. High performance SLD characteristics were obtained from both broad area ($20\times1000\ \mu m^2$) and ridge-waveguide ($4\times2500\ \mu m^2$) devices with 1000 μm integrated photon absorber, in pulsed operation [362]. An output power more than ~20 mW (Fig. 46(b)) was measured at an emission bandwidth ~82 nm (Fig. 46(c)) from the former device and corresponding power bandwidth product (PBP) of 1800 mW-nm. The latter ridge-waveguide device exhibited ~12 mW output power and a maximum bandwidth ~72 nm (PBP ~905 mW-nm). This investigation showed a significant improvement in the PBP values while maintaining the spectral ripple below 0.3 dB. In the CW operation, Khan et al. [9] provided a quantitative evidence of simultaneous amplified spontaneous emission from InGaAlAs Qwell and InAs Qdashes from multi-stack DaWELL structure by demonstrating a record emission bandwidth of >700 nm at room temperature from a broad area $50\times1000\ \mu m^2$ SLD device with output power >0.3 mW and capability of reaching beyond 1.3 mW. As shown in Fig. 46(d), the emission wavelength spanned from ~1.3–~1.9 μm covering the entire O–E–S–C–L–U

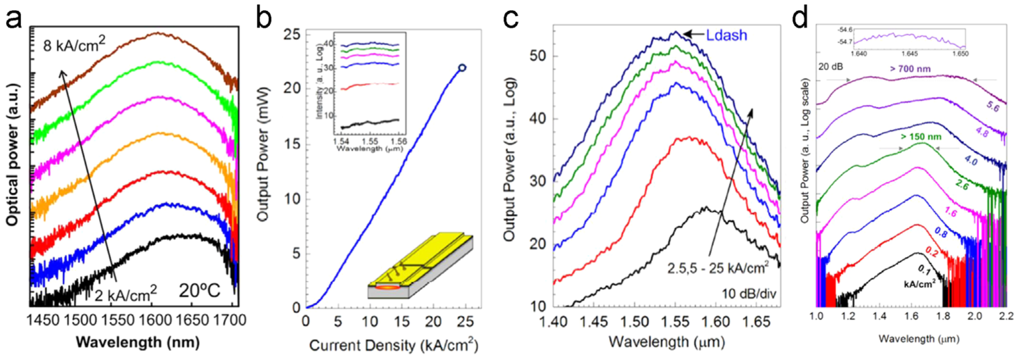


Fig. 46. (a) Broadband spectra from InAs/InGaAlAs DaWELL SLD (1000 μm long gain section with 1000 μm photon absorber section) at different current injections from 2–8 kA/cm measured at 20 °C. (b) Room temperature *L–I* characteristics of 20 × 1000 μm$^2$ chirped Qdash broad area SLD in pulsed operation, and with an integrated 1000 μm photon absorber section. (c) The corresponding wideband emission spectra at different injection current density at 2.5 kA/cm$^2$ and 5–25 kA/cm$^2$ in steps of 5 kA/cm$^2$. (d) The ultra-broadband emission spectra at room temperature of the fabricated 50 × 1000 μm$^2$ chirped Qdash SLD device at different injection current density under CW operation. The insets in (b) and (d) shows the spectra ripple within 10 nm from the central wavelength. The emission spectra in (a), (c) and (d) are vertically offset for clarity. Courtesy of [9,362,363].

communication bands. This achievement was attributed to all the possible optical transitions of the Qdash layers and asymmetric Qwells covering the long and short wavelength emission regions, respectively, in addition to junction heating.

## 6. Conclusion

In this paper, we reviewed the current advances of InAs/InP based Qdots and Qdash structures from the growth as well as device implementation view point. These 0D and quasi-0D nanostructures show promise in satisfying the exponentially growing internet and mobile connectivity in terms of the bandwidth, power consumption, and cost requirements. The unique properties of Qdot laser exhibiting low threshold, fast modulation, and sub-pico second pulse generation, and Qdash lasers capable of producing broadband stimulated emission and potential to replace multiple discrete laser components in the WDM system by a single device, are capable of meeting the stringint demand of implementing optical interconnects system with energy per bit of ~100 fJ/bit and eventually ~50 fJ/bit in near future [364,365], besides broadband SOAs capability of simultaneously amplifying multiple wavelengths. Furthermore, the current bandwidth hungry scenario at 1.55 μm telecommunication wavelength also calls for extending the transmission system window towards 2 μm wavelength. In this respect, the excellent long wavelength tuning properties of InAs Qdot/Qdash laser and related components with their ability to reach this wavelength regime, when implemented according to their strength, pose to realize a green ICT in the near future.

## Acknowledgment

The author gratefully acknowledges the support of King Abdullah University of Science and Technology's (KAUST) baseline funding and competitive research grant CRG-1-2012-OOI-010.

## References

[1] D. Bimberg, M. Grundmann, N.N. Ledentsov, Quantum Dot Heterostructures, John Wiley and Sons, Chichester, England, 1999.
[2] A. Zhukov, M. Maksimov, A. Kovsh, Semiconductors 46 (2012) 1225–1250.
[3] R. Wang, A. Stintz, P. Varangis, T. Newell, H. Li, K. Malloy, et al., IEEE Photon. Technol. Lett 13 (2001) 767–769.
[4] V. Sichkovskyi, M. Waniczek, J. Reithmaier, Appl. Phys. Lett. 102 (2013) 221117.
[5] J.P. Reithmaier, G. Eisenstein, A. Forchel, Proc. IEEE 95 (2007) 1779–1790.
[6] D. Zhou, R. Piron, M. Dontabactouny, O. Dehaese, F. Grillot, T. Batte, et al., Appl. Phys. Lett. 94 (2009) 081107.
[7] D. Zhou, R. Piron, F. Grillot, O. Dehaese, E. Homeyer, M. Dontabactouny, et al., Appl. Phys. Lett. 93 (2008) 161104–161104-3.
[8] M.Z.M. Khan, T.K. Ng, C.-S. Lee, P. Bhattacharya, B.S. Ooi, Appl. Phys. Lett. 102 (2013) 091102.
[9] M.Z.M. Khan, M.A. Majid, T.K. Ng, D. Cha, B.S. Ooi, Opt. Lett. 38 (2013) 3720–3723.
[10] J. Liu, Z. Lu, P. Poole, P. Barrios, D. Poitras, Z. Jiao, et al., Opt. Commun. 285 (2012) 1323–1325.
[11] Z. Lu, J. Liu, P. Poole, Z. Jiao, P. Barrios, D. Poitras, et al., Opt. Commun. 284 (2011) 2323–2326.
[12] Y.-S. Hsieh, Y.-C. Ho, S.-Y. Lee, C.-C. Chuang, J.-C. Tsai, K.-F. Lin, et al., Sensors 13 (2013) 8928–8949.
[13] S. Ishida, N. Nishizawa, Biomed. Opt. Express 3 (2012) 282–294.
[14] V. Kodach, J. Kalkman, D. Faber, T. van Leeuwen, Quantitative comparison of the OCT imaging depth at 1300 nm and 1600 nm, Biomed. Opt. Express 1 (2010) 176–185.
[15] U. Sharma, E.W. Chang, S.H. Yun, Opt. Express 16 (2008) 19712–19723.
[16] K. Scholle, S. Lamrini, P. Koopmann, and P. Fuhrberg, 2 μm laser sources and their possible applications, in: Intech (ed.) Proceedings of the Frontiers in Guided Wave Optics and Optoelectronics, 2010.
[17] D. Stifter, K. Wiesauer, M. Wurm, E. Schlotthauer, J. Kastner, M. Pircher, et al., Meas. Sci. Technol. 19 (2008) 074011.
[18] H. Tanoto, S. Yoon, T. Ng, C. Ngo, C. Dohrman, E. Fitzgerald, et al., Appl. Phys. Lett. 95 (2009) 2111.
[19] H. Liu, T. Wang, Q. Jiang, R. Hogg, F. Tutu, F. Pozzi, et al., Nat. Photon. 5 (2011) 416–419.
[20] J.-X. Fu, S.R. Bank, M.A. Wistey, H.B. Yuen, J.S. Harris, J. Vac. Sci. Technol. B: Microelectron. Nanometer Struct. 22 (2004) 1463–1467.
[21] I.N. Stranski, L. Krastanov, Akad. Wiss. Lit. Mainz Abh. Math. Naturwiss. Kl., Abt. 2B 146 (1938) 797.
[22] L. González, J.M. García, R. García, F. Briones, J. Martínez-Pastor, C. Ballesteros, Appl. Phys. Lett. 76 (2000) 1104–1106.
[23] J. Brault, M. Gendry, G. Grenet, G. Hollinger, Y. Desieres, T. Benyattou, Appl. Phys. Lett. 73 (1998) 2932–2934.
[24] S. Fafard, J.P. McCaffrey, Y. Feng, C. Allen, H. Marchand, L. Isnard, et al, Toward quantum dot laser diodes emitting at 1.5 μm, in: Proceedings of the International Conference on Applications of Photonic Technology, 1998, pp. 2710276.
[25] J.S. Kim, J.H. Lee, S.U. Hong, H.-S. Kwack, B.S. Choi, D.K. Oh, Appl. Phys. Lett. 87 (2005) 053102–053102-3.
[26] J. Reithmaier, A. Somers, S. Deubert, R. Schwertberger, W. Kaiser, A. Forchel, et al., J. Phys. D: Appl. Phys. 38 (2005) 2088.
[27] H. Saito, K. Nishi, S. Sugou, Appl. Phys. Lett. 78 (2001) 267–269.
[28] H. Li, J. Wu, Z. Wang, T. Daniels-Race, Appl. Phys. Lett. 75 (1999) 1173–1175.
[29] R. Nötzel, J. Temmyo, A. Kozen, T. Tamamura, T. Fukui, H. Hasegawa, Appl. Phys. Lett. 66 (1995) 2525–2527.
[30] I. Alghoraibi, T. Rohel, N. Bertru, A. Le Corre, A. Letoublon, P. Caroff, et al., J. Cryst. Growth 293 (2006) 263–268.
[31] P. Caroff, N. Bertru, A. le Corre, O. Dehaese, T. Rohel, I. Alghoraibi, et al., Jpn. J. Appl. Phys. 44 (2005) L1069.
[32] K. Akahane, N. Ohtani, Y. Okada, M. Kawabe, J. Cryst. Growth 245 (2002) 31–36.
[33] K. Akahane, N. Yamamoto, N. Ohtani, Y. Okada, M. Kawabe, J. Cryst. Growth 256 (2003) 7–11.
[34] K. Akahane, N. Yamamoto, T. Kawanishi, Phys. Status Solidi (a) 208 (2011) 425–428.
[35] K. Akahane, N. Yamamoto, M. Tsuchiya, Appl. Phys. Lett. 93 (2008) 041121.
[36] J.S. Kim, J.H. Lee, S.U. Hong, W.S. Han, H.-S. Kwack, C.W. Lee, et al., J. Cryst. Growth 259 (2003) 252–256.
[37] A. Ponchet, A. le Corre, H. L'haridon, B. Lambert, S. Salaün, Appl. Phys. Lett. 67 (1995) 1850–1852.
[38] A. Stintz, T. Rotter, K. Malloy, J. Cryst. Growth 255 (2003) 266–272.
[39] M. Borgstrom, M. Pires, T. Bryllert, S. Landi, W. Seifert, P. Souza, J. Cryst. Growth 252 (2003) 481–485.
[40] Y. Li, X. Ye, B. Xu, F. Liu, D. Ding, W. Jiang, et al., J. Cryst. Growth 218 (2000) 451–454.
[41] J.S. Kim, J.H. Lee, S.U. Hong, W.S. Han, H.-S. Kwack, D.K. Oh, Appl. Phys. Lett. 83 (2003) 3785–3787.
[42] J.S. Kim, C.-R. Lee, B.S. Choi, H.-S. Kwack, C.W. Lee, E.D. Sim, et al., Appl. Phys. Lett. 90 (2007) 153111–153111-3.
[43] Y. Yang, B. Jo, J. Kim, C.-R. Lee, J.S. Kim, D.K. Oh, et al., J. Appl. Phys. 105 (2009) 053510.

[44] Y. Yang, B. Jo, J. Kim, K.J. Lee, M. Ko, C.-R. Lee, et al., Thin Solid Films 517 (2009) 3979–3982.
[45] C. Gilfert, E.-M. Pavelescu, J. Reithmaier, Appl. Phys. Lett. 96 (2010) 191903.
[46] S. Fafard, Z. Wasilewski, J. McCaffrey, S. Raymond, S. Charbonneau, Appl. Phys. Lett. 68 (1996) 991–993.
[47] S. Yoon, Y. Moon, T.-W. Lee, E. Yoon, Y.D. Kim, Appl. Phys. Lett. 74 (1999) 2029–2031.
[48] A. Michon, G. Saint-Girons, G. Beaudoin, I. Sagnes, L. Largeau, G. Patriarche, Appl. Phys. Lett. 87 (2005) 253114.
[49] A. Michon, G. Patriarche, G. Beaudoin, G. Saint-Girons, N. Gogneau, I. Sagnes, Appl. Phys. Lett. 91 (2007) 102107–102107-3.
[50] R. Nötzel, S. Anantathanasarn, R.P. van Veldhoven, F.W. van Otten, T.J. Eijkemans, A. Trampert, et al., Jpn. J. Appl. Phys. 45 (2006) 6544.
[51] S. Anantathanasarn, R. Nötzel, P. van Veldhoven, T. Eijkemans, J. Wolter, J. Appl. Phys. 98 (2005) 013503.
[52] R. Notzel, S. Anantathanasarn, P. van Veldhoven, F. van Otten, T. Eijkemans, A. Trampert, et al., J. Vac. Sci. Technol. B 24 (2006) 2075–2079.
[53] S. Anantathanasarn, R. Nötzel, P. van Veldhoven, F. van Otten, T. Eijkemans, J. Wolter, Appl. Phys. Lett. 88 (2006) 063105.
[54] S. Anantathanasarn, R. Nötzel, P. van Veldhoven, F. van Otten, Y. Barbarin, G. Servanton, et al., Microelectron. J. 37 (2006) 1461–1467.
[55] J. Jang, S. Pyun, S. Lee, I. Lee, W.G. Jeong, R. Stevenson, et al., Appl. Phys. Lett. 85 (2004) 3675–3677.
[56] S. Pyun, S. Lee, I. Lee, H. Kim, W.G. Jeong, J. Jang, et al., J. Appl. Phys. 96 (2004) 5766–5770.
[57] A. Michon, R. Hostein, G. Patriarche, N. Gogneau, G. Beaudoin, A. Beveratos, et al., J. Appl. Phys. 104 (2008) 043504.
[58] P. Poole, J. McCaffrey, R. Williams, J. Lefebvre, D. Chithrani, J. Vac. Sci. Technol. B 19 (2001) 1467–1470.
[59] S. Fréchengues, N. Bertru, V. Drouot, B. Lambert, S. Robinet, S. Loualiche, et al., Appl. Phys. Lett. 74 (1999) 3356–3358.
[60] P. Poole, R. Williams, J. Lefebvre, J. McCaffrey, and N. Rowell, Trimming the size of InAs/InP quantum dots grown by CBE, in: Proceedings of the International Conference on Indium Phosphide and Related Materials, 2000, pp. 396–399.
[61] N.N. Ledentsov, V.A. Shchukin, M. Grundmann, N. Kirstaedter, J. Böhrer, O. Schmidt, et al., Phys. Rev. B 54 (09/15/ 1996) 8743–8750.
[62] H.R. Gutiérrez, M.A. Cotta, J.R.R. Bortoleto, M.M.G. de Carvalho, J. Appl. Phys. 92 (2002) 7523–7526.
[63] Q. Gong, R. Nötzel, P. van Veldhoven, J. Wolter, J. Cryst. Growth 278 (2005) 67–71.
[64] Q. Gong, R. Nötzel, P. van Veldhoven, T. Eijkemans, J. Wolter, Appl. Phys. Lett. 84 (2004) 275–277.
[65] Q. Gong, R. Notzel, P. van Veldhoven, T. Eijkemans, J. Wolter, Appl. Phys. Lett. 85 (2004) 1404–1406.
[66] E. Homeyer, R. Piron, F. Grillot, O. Dehaese, K. Tavernier, E. Macé, et al., Semicond. Sci. Technol. 22 (2007) 827.
[67] Z.R. Wasilewski, S. Fafard, J.P. McCaffrey, J. Cryst. Growth 201–202 (1999) 1131–1135 (5//).
[68] P. Poole, K. Kaminska, P. Barrios, Z. Lu, J. Liu, J. Cryst. Growth 311 (2009) 1482–1486.
[69] P. Poole, InP-Based Quantum Dot Lasers, in: Advances in Semiconductor Lasers, vol. 86 (ed.), 2012, p. 419.
[70] P. Poole, R. Williams, J. Lefebvre, S. Moisa, J. Cryst. Growth 257 (2003) 89–96.
[71] S. Li, Q. Gong, Y. Lao, K. He, J. Li, Y. Zhang, et al., Appl. Phys. Lett. 93 (2008) 111109–111109-3.
[72] G. Elias, A. Létoublon, R. Piron, I. Alghoraibi, A. Nakkar, N. Chevalier, et al., Jpn. J. Appl. Phys. 48 (2009) 070204.
[73] S. Li, Q. Gong, C. Cao, X. Wang, L. Yue, Q. Liu, et al., Infrared Phys. Technol. 55 (2012) 205–209.
[74] B. Jo, C.-R. Lee, J.S. Kim, W.S. Han, J.H. Song, J.-Y. Leem, et al., J. Cryst. Growth 393 (2014) 59–63.
[75] G. Elias, A. Letoublon, R. Piron, I. Alghraibi, K. Tavernier, N. Chevalier, et al., Improvement of 1.55 μm InAs QD laser using vicinal (001) InP substrate, in: Proceedings of the IEEE International Conference on Indium Phosphide and Related Materials (IPRM), 2009, pp. 41–44.
[76] C. Paranthoen, N. Bertru, O. Dehaese, A. le Corre, S. Loualiche, B. Lambert, et al., Appl. Phys. Lett. 78 (2001) 1751–1753.
[77] C. Paranthoen, C. Platz, G. Moreau, N. Bertru, O. Dehaese, A. Le Corre, et al., J. Cryst. Growth 251 (2003) 230–235.
[78] P. Caroff, N. Bertru, C. Platz, O. Dehaese, A. le Corre, S. Loualiche, J. Cryst. Growth 273 (2005) 357–362.
[79] J. Ulloa, P. Koenraad, E. Gapihan, A. Letoublon, N. Bertru, Appl. Phys. Lett. 91 (2007) 073106–073106-3.
[80] S. Fréchengues, V. Drouot, N. Bertru, B. Lambert, S. Loualiche, A. Le Corre, J. Cryst. Growth 201 (1999) 1180–1185.
[81] A. Nakkar, H. Folliot, A. le Corre, F. Doré, I. Alghoraibi, C. Labbé, et al., Appl. Phys. Lett. 92 (2008) 231911–231911-3.

[82] N. Bertru, C. Paranthoen, O. Dehaese, H. Folliot, A. le Corre, R. Piron, et al., QD laser on InP substrate for 1.55 μm emission and beyond, in: Proceedings of the of SPIE, 2010, pp. 76081B-1–76081B-14.
[83] J.F. Girard, C. Dion, P. Desjardins, C.N. Allen, P.J. Poole, S. Raymond, Appl. Phys. Lett. 84 (2004) 3382–3384.
[84] C.K. Chia, S.J. Chua, S. Tripathy, J.R. Dong, Appl. Phys. Lett. 86 (2005).
[85] Y. Wang, H.S. Djie, B.S. Ooi, Appl. Phys. Lett. 88 (-, 2006).
[86] C. Dion, P.J. Poole, S. Raymond, P. Desjardins, F. Schiettekatte, Appl. Phys. Lett. 89 (2006).
[87] S. Barik, H.H. Tan, C. Jagadish, Appl. Phys. Lett. 88 (2006).
[88] C. Dion, P. Desjardins, M. Chicoine, F. Schiettekatte, P. Poole, S. Raymond, Nanotechnology 18 (2007) 015404.
[89] S. Barik, H.H. Tan, C. Jagadish, Appl. Phys. Lett. 90 (2007).
[90] W. Lei, C. Jagadish, J. Appl. Phys. 104 (2008).
[91] A. Zhukov, V. Ustinov, A. Kovsh, A.Y. Egorov, N. Maleev, N. Ledentsov, et al., Semicond. Sci. Technol. 14 (1999) 575.
[92] Z. Yin, X. Tang, Solid-State Electron. vol. 51 (1// 2007) 6–15.
[93] Y. Qiu, D. Uhl, Appl. Phys. Lett. 84 (2004) 1510–1512.
[94] F. Doré, C. Cornet, P. Caroff, A. Ballestar, J. Even, N. Bertru, et al., Phys. Status Solidi (c) 3 (2006) 3920–3923.
[95] J. Kotani, P.J. van Veldhoven, R. Nötzel, J. Appl. Phys. 106 (2009) 093112.
[96] Y. Qiu, D. Uhl, R. Chacon, R.Q. Yang, Appl. Phys. Lett. 83 (2003) 1704–1706.
[97] Y. Qiu, D. Uhl, S. Keo, Appl. Phys. Lett. 84 (2004) 263–265.
[98] V. Ustinov, A. Zhukov, A.Y. Egorov, A. Kovsh, S. Zaitsev, N.Y. Gordeev, et al., Electron. Lett. 34 (1998) 670–672.
[99] V.M. Ustinov, A.R. Kovsh, A.E. Zhukov, A.Y. Egorov, N.N. Ledentsov, A.V. Lunev, et al., Tech. Phys. Lett. 24 (1998) 22–23.
[100] K. Nishi, M. Yamada, T. Anan, A. Gomyo, and S. Sugou, Long-wavelength lasing from InAs self-assembled quantum dots on (311) B InP by gas-source molecular beam epitaxy, in: Proceedings of the IEEE International Conference on Indium Phosphide and Related Materials, 1998, pp. 163–166.
[101] P. Caroff, C. Paranthoen, C. Platz, O. Dehaese, H. Folliot, N. Bertru, et al., Appl. Phys. Lett. 87 (2005) 243107–243107-3.
[102] A. Martinez, K. Merghem, S. Bouchoule, G. Moreau, A. Ramdane, J.-G. Provost, et al., Appl. Phys. Lett. 93 (2008) 021101–021101-3.
[103] K. Nishi, M. Yamada, T. Anan, A. Gomyo, S. Sugou, Appl. Phys. Lett. 73 (1998) 526–528.
[104] C. Paranthoen, N. Bertru, B. Lambert, O. Dehaese, A. le Corre, J. Even, et al., Semicond. Sci. Technol. 17 (2002) L5.
[105] E. Homeyer, R. Piron, F. Grillot, O. Dehaese, K. Tavernier, E. Macé, et al., Jpn. J. Appl. Phys. 46 (2007) 6903.
[106] K. Klaime, C. Calò, R. Piron, C. Paranthoen, D. Thiam, T. Batte, et al., Opt. Express 21 (2013) 29000–29005.
[107] K. Akahane, N. Yamamoto, and T. Kawanishi, Wavelength tunability of highly stacked quantum dot laser fabricated by a strain compensation technique, in: Proceedings of the 22nd IEEE International Semiconductor Laser Conference (ISLC), 2010, pp. 37–38.
[108] K. Akahane, N. Yamamoto, and T. Kawanishi, The dependence of the characteristic temperature of highly stacked InAs quantum dot laser diodes fabricated using a strain-compensation technique on stacking layer number, in: Proceedings of the 23rd IEEE International Semiconductor Laser Conference (ISLC), 2012, pp. 82–83.
[109] I. Alghoraibi, T. Rohel, R. Piron, N. Bertru, C. Paranthoen, G. Elias, et al., Appl. Phys. Lett. 91 (2007) 261105–261105-3.
[110] K. Akahane, N. Yamamoto, H. Sotobayashi, and M. Tsuchiya, 1.7 μm laser emission at room temperature using highly-stacked InAs quantum dots, in: Proceedings of the 20th International Conference on Indium Phosphide and Related Materials (IPRM), 2008, pp. 1–3.
[111] J.S. Kim, J.H. Lee, S.U. Hong, W.S. Han, H.-S. Kwack, C.W. Lee, et al., Appl. Phys. Lett. 85 (2004) 1033–1035.
[112] J.S. Kim, J.H. Lee, S.U. Hong, W.S. Han, H.-S. Kwack, C.W. Lee, et al., IEEE Photon. Technol. Lett. 16 (2004) 1607–1609.
[113] B. Jo, Y. Yang, J. Kim, M. Ko, K.J. Lee, C.-R. Lee, et al., Thin Solid Films 517 (2009) 3983–3986.
[114] C. Gilfert, V. Ivanov, N. Oehl, M. Yacob, J. Reithmaier, Appl. Phys. Lett. 98 (2011) 201102-1–201102-3.
[115] S. Bhowmick, M.Z. Baten, T. Frost, B.S. Ooi, P. Bhattacharya, IEEE J. Quant. Electron. 50 (2013) 7–14.
[116] D. Gready, G. Eisenstein, C. Gilfert, V. Ivanov, J.P. Reithmaier, IEEE Photon. Technol. Lett. vol. 24 (2012) 809–811.
[117] D. Gready, G. Eisenstein, V. Ivanov, C. Gilfert, F. Schnabel, A. Rippien, et al., IEEE Photon. Technol. Lett. 26 (2014) 11–13.
[118] C.N. Allen, P. Poole, P. Marshall, J. Fraser, S. Raymond, S. Fafard, Appl. Phys. Lett. 80 (2002) 3629–3631.
[119] C.N. Allen, P. Poole, P. Barrios, P. Marshall, G. Pakulski, S. Raymond, et al., Physica E 26 (2005) 372–376.
[120] J. Renaudier, R. Brenot, B. Dagens, F. Lelarge, B. Rousseau, F. Poingt, et al., Electron. Lett. 41 (2005) 1007–1008.

[121] F. le large, B. Rousseau, B. Dagens, F. Poingt, F. Pommereau, A. Accard, IEEE Photon. Technol. Lett. 17 (2005) 1369–1371.
[122] S. Anantathanasarn, R. Notzel, P. van Veldhoven, F. van Otten, Y. Barbarin, G. Servanton, et al., Appl. Phys. Lett. 89 (2006) 073115–073115-3.
[123] S.G. Li, Q. Gong, C.F. Cao, X.Z. Wang, L. Yue, J.Y. Yan, et al., Physica E 44 (2012) 1983–1987.
[124] S. Li, Q. Gong, Y. Lao, Y. Zhang, S. Feng, H. Wang, Electron. Lett. 46 (2010) 158–159.
[125] Z. Jiao, Z. Lu, J. Liu, P. Poole, P. Barrios, D. Poitras, et al., Opt. Commun. 285 (2012) 4372–4375.
[126] H. Kim, W. Jeong, J. Lee, J. Yim, D. Lee, R. Stevenson, et al., Appl. Phys. Lett. 87 (2005) 083110–083110-3.
[127] J. Kotani, P. van Veldhoven, T. de Vries, B. Smalbrugge, E. Bente, M. Smit, et al., Electron. Lett. 45 (2009) 1317–1318.
[128] J. Kotani, P.J. van Veldhoven, R. Nötzel, Appl. Phys. Lett. 3 (2010) 072101.
[129] R. Notzel, IEEE Photon. J. 2 (2010) 67–80.
[130] C.N. Allen, G. Ortner, C. Dion, P. Poole, P. Barrios, J. Lapointe, et al., Appl. Phys. Lett. 88 (2006) 113109–113109-3.
[131] S. Li, Q. Gong, C. Cao, X. Wang, J. Yan, Y. Wang, et al., Opt. Quant. Electron. 46 (2014) 623–640.
[132] G. Ortner, C.N. Allen, C. Dion, P. Barrios, D. Poitras, D. Dalacu, et al., Appl. Phys. Lett. 88 (2006) 121119-1–121119-3.
[133] P. Chen, Q. Gong, C. Cao, S. Li, Y. Wang, Q. Liu, et al., Appl. Phys. Lett. 98 (2011) 121102.
[134] J. Liu, Z. Lu, S. Raymond, P. Poole, P. Barrios, G. Pakulski, et al., Electron Lett. 43 (2007) 458–460.
[135] J. Liu, Z. Lu, S. Raymond, P. Poole, P. Barrios, D. Poitras, IEEE Photon. Technol. Lett. 20 (2008) 81–83.
[136] Z. Lu, J. Liu, P. Poole, S. Raymond, P. Barrios, D. Poitras, et al., Low noise InAs/InP quantum dot C-band monolithic multiwavelength lasers for WDM-PONs, in: Proceedings of the Optical Fiber Communication Conference, 2009, p. JWA27.
[137] J.S. Kim, J.H. Lee, S.U. Hong, H.-S. Kwack, B.S. Choi, D.K. Oh, IEEE Photon. Technol. Lett. 18 (2006) 595–597.
[138] Z. Lu, P. Poole, J. Liu, P. Barrios, Z. Jiao, G. Pakulski, et al., Electron. Lett. 47 (2011) 818–819.
[139] J.P. Reithmaier, V. Ivanov, V. Sichkovskyi, C. Gilfert, A. Rippien, N. Felgen, et al., InP-based 1.5 μm quantum dot lasers: Static and dynamic properties, in: Proceedings of the IEEE Photonics Conference (IPC), 2013, pp. 1–2.
[140] M.J. Heck, E.A. Bente, B. Smalbrugge, Y.-S. Oei, M.K. Smit, S. Anantathanasarn, Opt. Express 15 (2007) 16292–16301.
[141] M.J. Heck, A. Renault, E.A. Bente, Y.-S. Oei, M.K. Smit, K.S. Eikema, et al., IEEE J. Sel. Top. Quant. Electron. 15 (2009) 634–643.
[142] M. Tahvili, L. Du, M. Heck, R. Nötzel, M. Smit, E. Bente, Opt. Express 20 (2012) 8117–8135.
[143] M.J. Heck, E.J. Salumbides, A. Renault, E.A. Bente, Y.-S. Oei, M.K. Smit, et al., Opt. Express 17 (2009) 18063–18075.
[144] Z. Lu, J. Liu, P. Poole, P. Barrios, D. Poitras, S. Raymond, et al., A passive mode-locked InAs/InP quantum dot laser with pulse duration of less than 300 fs, in: Proceedings of the SPIE OPTO: Integrated Optoelectronic Devices, 2009, pp. 722413-1–722413-7.
[145] Z. Lu, J. Liu, S. Raymond, P. Poole, P. Barrios, D. Poitras, Opt. Express 16 (2008) 10835–10840.
[146] J. Liu, Z. Lu, S. Raymond, P. Poole, P. Barrios, D. Poitras, Opt. Lett. 33 (2008) 1702–1704.
[147] Z. Lu, J. Liu, P. Poole, S. Raymond, P. Barrios, D. Poitras, et al., Opt. Express 17 (2009) 13609–13614.
[148] Z. Jiao, J. Liu, Z. Lu, X. Zhang, P.J. Poole, P.J. Barrios, et al., IEEE Photon. Technol. Lett. 23 (2011) 543–545.
[149] Z. Jiao, J. Liu, Z. Lu, X. Zhang, P.J. Poole, P.J. Barrios, et al., IEEE Photon. Technol. Lett. 24 (2012) 518–520.
[150] S. Weiss, J.M. Wiesenfeld, D.S. Chemla, G. Raybon, G. Sucha, M. Wegener, et al., Appl. Phys. Lett. 60 (1992) 9–11.
[151] P.J.A. Thijs, L.F. Tiemeijer, P.I. Kuindersma, J.J.M. Binsma, T. van Dongen, IEEE J. Quant. Electron. 27 (1991) 1426–1439.
[152] G. Eisenstein, J.M. Wiesenfeld, M. Wegener, G. Sucha, D.S. Chemla, S. Weiss, et al., Appl. Phys. Lett. 58 (1991) 158–160.
[153] E. Bogaart, R. Notzel, Q. Gong, J. Haverkort, J. Wolter, Appl. Phys. Lett. 86 (2005) 173109-1–173109-3.
[154] T. Akiyama, M. Ekawa, M. Sugawara, K. Kawaguchi, H. Sudo, A. Kuramata, et al., IEEE Photon. Technol. Lett. 17 (2005) 1614–1616.
[155] T. Akiyama, M. Ekawa, M. Sugawara, H. Sudo, K. Kawaguchi, A. Kuramata, et al., An ultrawide-band (120 nm) semiconductor optical amplifier having an extremely-high penalty-free output power of 23 dBm realized with quantum-dot active layers, in: Proceedings of the Optical Fiber Communication Conference, 2004, PD12.
[156] T. Akiyama, M. Sugawara, Y. Arakawa, Proc. IEEE 95 (2007) 1757–1766.
[157] K. Akahane, N. Yamamoto, T. Umezawa, A. Kanno, T. Kawanishi, Jpn. J. Appl. Phys. 53 (2014) 04EG02.
[158] A. Matsumoto, Y. Takei, A. Matsushita, K. Akahane, Y. Matsushima, and K. Utaka, Fundamental characteristics of 1550 nm-band 20-layer-stacked QD-SOA grown on InP(311)B substrate for all-optical logic gate device, in: Proceedings of the 18th Microoptics Conference (MOC), 2013, pp. 1–2.

[159] N. Kim, J. Oh, M. Kim, D. Lee, S. Pyun, W. Jeong, et al., Appl. Phys. Lett. 90 (2007) 241108-1–241108-3.
[160] G. Contestabile, A. Maruta, K. Kitayama, IEEE Photon. Technol. Lett. 22 (2010) 987–989.
[161] P. Borri, W. Langbein, J.M. Hvam, F. Heinrichsdorff, M.H. Mao, D. Bimberg, IEEE Photon. Technol. Lett. 12 (2000) 594–596.
[162] T. Vallaitis, C. Koos, R. Bonk, W. Freude, M. Laemmlin, C. Meuer, et al., Opt. Express 16 (2008) 170–178 (2008/01/07).
[163] K. Solis-Trapala, Y. An, R. Notzel, H.J. Dorren, and R.J. Manning, Gain and phase dynamics of an InAs/InGaAsP/InP quantum-dot semiconductor optical amplifier at 1.55 m, in: Proceedingsw of the Advanced Photonics and Renewable Energy, Karlsruhe, 2010, NMB2.
[164] A.J. Zilkie, J. Meier, P.W. Smith, M. Mojahedi, J.S. Aitchison, P.J. Poole, et al., Opt. Express 14 (2006) 11453–11459.
[165] A.J. Zilkie, J. Meier, M. Mojahedi, P.J. Poole, P. Barrios, D. Poitras, et al., IEEE J. Quant. Electron. 43 (2007) 982–991.
[166] A.J. Zilkie, J. Meier, M. Mojahedi, A.S. Helmy, P.J. Poole, P. Barrios, et al., J. Lightwave Technol. 26 (2008) 1498–1509.
[167] J. Park, N. Kim, Y. Jang, E. Lee, J. Lee, J. Baek, et al., Appl. Phys. Lett. 98 (2011) 011107.
[168] M. Sugawara, N. Hatori, M. Ishida, H. Ebe, Y. Arakawa, T. Akiyama, et al., J. Phys. D: Appl. Phys. 38 (2005) 2126.
[169] G. Contestabile, A. Maruta, S. Sekiguchi, K. Morito, M. Sugawara, K. Kitayama, IEEE Photon. Technol. Lett. 22 (2010) 492–494.
[170] J. Park, Y. Jang, J. Baek, N. Kim, K. Yee, H. Lee, et al., Opt. Express 20 (2012) 6215–6224.
[171] Z. Lu, J. Liu, S. Raymond, P. Poole, P. Barrios, D. Poitras, et al., Electron. Lett. 42 (2006) 1112–1114.
[172] G. Contestabile, Y. Yoshida, A. Maruta, K. Kitayama, IEEE Photon. Technol. Lett. 25 (2013) 791–794.
[173] G. Contestabile, A. Maruta, K.I. Kitayama, IEEE J. Quant. Electron. 50 (2014) 379–389.
[174] G. Contestabile, A. Maruta, S. Sekiguchi, K. Morito, M. Sugawara, K.-i. Kitayama, IEEE J. Quant. Electron. 46 (2010) 1696–1703.
[175] K. Akahane, N. Yamamoto, T. Kawanishi, Adv. Mater. Res. 871 (2014) 269–273.
[176] T. Utzmeier, P.A. Postigo, J. Tamayo, R. Garcia, F. Briones, Appl. Phys. Lett. 69 (1996) 2674–2676.
[177] S. Guo, H. Ohno, A. Shen, F. Matsukura, Y. Ohno, Appl. Phys. Lett. 70 (1997) 2738–2740.
[178] H. Li, Q. Zhuang, X. Kong, Z. Wang, T. Daniels-Race, J. Cryst. Growth 205 (1999) 613–617.
[179] J. Brault, M. Gendry, O. Marty, M. Pitaval, J. Olivares, G. Grenet, et al., Appl. Surf. Sci. 162–163 (2000) 584–589.
[180] R. Schwertberger, D. Gold, J. Reithmaier, A. Forchel, J. Cryst. Growth 251 (2003) 248–252.
[181] R. Schwertberger, D. Gold, J. Reithmaier, A. Forchel, IEEE Photon. Technol. Lett. 14 (2002) 735–737.
[182] T. Rotter, A. Stintz, and K. Malloy, InP based quantum dash lasers with 2 μm wavelength, in: Proceedings of IEEE Optoelectronics, 2003, pp. 318–321.
[183] A. Sauerwald, T. Kummell, G. Bacher, A. Somers, R. Schwertberger, J. Reithmaier, et al., Appl. Phys. Lett. 86 (2005) 253112–253112-3.
[184] T. Kümmell, A. Sauerwald, A. Somers, A. Löffler, J. Reithmaier, A. Forchel, et al., Phys E: Low-dimens. Syst. Nanostruct. 32 (2006) 108–110.
[185] A. Sauerwald, T. Kümmell, A. Löffler, A. Somers, J. Reithmaier, A. Forchel, et al., Phys. Status Solidi (c) 3 (2006) 3947–3950.
[186] Z. Mi, J. Yang, P. Bhattacharya, IEEE Photon. Technol. Lett. 18 (2006) 1377–1379.
[187] P. Podemski, G. Sęk, K. Ryczko, J. Misiewicz, S. Hein, S. Höfling, et al., Appl. Phys. Lett. 93 (2008) (-,).
[188] Z. Mi, P. Bhattacharya, IEEE J. Quant. Electron. 42 (2006) 1224–1232.
[189] S. Hein, P. Podemski, G. Sęk, J. Misiewicz, P. Ridha, A. Fiore, et al., Appl. Phys. Lett. 94 (2009) 241113.
[190] A. Musiał, P. Podemski, G. Sęk, P. Kaczmarkiewicz, J. Andrzejewski, P. Machnikowski, et al., Semicond. Sci. Technol. 27 (2012) 105022.
[191] A. Ukhanov, R. Wang, T. Rotter, A. Stintz, L. Lester, P. Eliseev, et al., Appl. Phys. Lett. 81 (2002) 981–983.
[192] D.P. Popescu, K.J. Malloy, IEEE Photon. Technol. Lett. 18 (2006) 2401–2403.
[193] P. Podemski, R. Kudrawiec, J. Misiewicz, A. Somers, R. Schwertberger, J. Reithmaier, et al., Appl. Phys. Lett. 89 (2006) 151902.
[194] N.A. Jahan, C. Hermannstädter, J.-H. Huh, H. Sasakura, T.J. Rotter, P. Ahirwar, et al., J. Appl. Phys. 113 (2013) 033506.
[195] W. Rudno-Rudziński, G. Sęk, K. Ryczko, R. Kudrawiec, J. Misiewicz, A. Somers, et al., Appl. Phys. Lett. 86 (2005) 101904.

[196] W. Rudno-Rudziński, R. Kudrawiec, P. Podemski, G. Sęk, J. Misiewicz, A. Somers, et al., Appl. Phys. Lett. 89 (2006) 031908.
[197] W. Rudno-Rudziński, R. Kudrawiec, G. Sęk, J. Misiewicz, A. Somers, R. Schwertberger, et al., Appl. Phys. Lett. 88 (2006) (-,).
[198] P. Podemski, R. Kudrawiec, J. Misiewicz, A. Somers, J. Reithmaier, A. Forchel, Appl. Phys. Lett. 89 (2006) 061902.
[199] G. Sęk, P. Poloczek, P. Podemski, R. Kudrawiec, J. Misiewicz, A. Somers, et al., Appl. Phys. Lett. 90 (2007) 081915.
[200] I. Marko, S. Sweeney, A. Adams, S. Jin, B. Murdin, R. Schwertberger, et al., Phys. Status Solidi (b) 241 (2004) 3427–3431.
[201] C. Walther, W. Hoerstel, H. Niehus, J. Erxmeyer, W. Masselink, J. Cryst. Growth 209 (2000) 572–580.
[202] B. Salem, J. Olivares, G. Guillot, G. Bremond, J. Brault, C. Monat, et al., Appl. Phys. Lett. 79 (2001) 4435–4437.
[203] J. Garcıa, L. González, M.U. González, J.P. Silveira, Y. González, F. Briones, J. Cryst. Growth 227 (2001) 975–979.
[204] M. Gendry, C. Monat, J. Brault, P. Regreny, G. Hollinger, B. Salem, et al., J. Appl. Phys. 95 (2004) 4761–4766.
[205] D. Fuster, L. González, Y. González, M.U. González, J. Martínez-Pastor, J. Appl. Phys. 98 (2005) 033502.
[206] D. Fuster, M.U. González, L. González, Y. González, T. Ben, A. Ponce, et al., Appl. Phys. Lett. 85 (2004) 1424–1426.
[207] F. Lelarge, B. Dagens, J. Renaudier, R. Brenot, A. Accard, F. van Dijk, et al., IEEE J. Sel. Top. Quant. Electron. 13 (2007) 111–124.
[208] B. Alén, J. Martínez-Pastor, L. González, J.M. García, S.I. Molina, A. Ponce, et al., Phys. Rev. B 65 (2002) 241301.
[209] D. Fuster, M.U. González, L. González, Y. González, T. Ben, A. Ponce, et al., Appl. Phys. Lett. 84 (2004) 4723–4725.
[210] A. Lenz, F. Genz, H. Eisele, L. Ivanova, R. Timm, D. Franke, et al., Appl. Phys. Lett. 95 (2009) 203105–203105-3.
[211] M. Faugeron, M. Tran, F. Lelarge, M. Chtioui, Y. Robert, E. Vinet, et al., High power mode locked quantum dash 1.5 μm laser with asymmetrical cladding, in: Proceedings of the CLEO: Science and Innovations, 2012, JW2A, p. 85.
[212] B. Alén, J. Martınez-Pastor, A. Garcıa-Cristobal, L. González, J.M. Garcıa, Appl. Phys. Lett. 78 (2001) 4025–4027.
[213] B. Salem, T. Benyattou, G. Guillot, C. Bru-Chevallier, G. Bremond, C. Monat, et al., Phys. Rev. B 66 (2002) 193305.
[214] S.C. Heck, S. Osborne, S.B. Healy, E.P. O'Reilly, F. Lelarge, F. Poingt, et al., IEEE J. Quant. Electron. 45 (2009) 1508–1516.
[215] S. Heck, S. Healy, S. Osborne, E. O'Reilly, F. Lelarge, F. Poingt, et al., Appl. Phys. Lett. 92 (2008) 251105-1–251105-3.
[216] H.S. Djie, Y. Wang, B.S. Ooi, D.-N. Wang, J. Hwang, G.T. Dang, et al., IEEE Photon. Technol. Lett. 18 (2006) 2329–2331.
[217] H. Djie, Y. Wang, B. Ooi, D.-N. Wang, J. Hwang, X.-M. Fang, et al., Electron. Lett. 43 (2007) 33–35.
[218] H. Djie, Y. Wang, D. Negro, B. Ooi, Appl. Phys. Lett. 90 (2007) 031101.
[219] H.S. Djie, Y. Wang, Y.-H. Ding, D.-N. Wang, J. Hwang, X.-M. Fang, et al., IEEE J. Sel. Top. Quant. Electron. 14 (2008) 1239–1249.
[220] S. Deubert, A. Somers, W. Kaiser, R. Schwertberger, J. Reithmaier, A. Forchel, J. Cryst. Growth 278 (2005) 346–350.
[221] A. Somers, W. Kaiser, J. Reithmaier, and A. Forchel, InP-based quantum dash lasers for broadband optical amplification and gas sensing applications, in: Proceedings of the International Conference on Indium Phosphide and Related Materials, 2005, pp. 56–59.
[222] A. Somers, W. Kaiser, J. Reithmaier, A. Forchel, M. Gioaninni, I. Montrosset, Appl. Phys. Lett. 89 (2006) 061107-1–061107-3.
[223] M.Z.M. Khan, T. Ng, C.-S. Lee, D. Anjum, D. Cha, P. Bhattacharya, et al., IEEE Photon. J. 5 (2013) 1501308.
[224] C. Tan, H. Djie, C. Tan, V. Hongpinyo, Y. Ding, and B. Ooi, The effect of multi active junctions on broadband emission from InAs/InGaAlAs quantum-dash structure, in: Proceedings of the IEEE LEOS Annual Meeting Conference (LEOS), 2009, pp. 147–148.
[225] M.Z.M. Khan, T.K. Ng, C.-S. Lee, P. Bhattacharya, B.S. Ooi, IEEE J. Quant. Electron. 50 (2014) 51–61.
[226] B.S. Ooi, H.S. Djie, Y. Wang, C.-L. Tan, J. Hwang, X.-M. Fang, et al., IEEE J. Sel. Top. Quant. Electron. 14 (2008) 1230–1238.
[227] G.H. Duan, A. Shen, A. Akrout, F.V. Dijk, F. Lelarge, F. Pommereau, et al., Bell Labs Tech. J.l 14 (2009) 63–84.

[228] P. Resneau, M. Calligaro, S. Bansropun, O. Parillaud, M. Krakowski, R. Schwertberger, et al., High-power and low-noise 1.55 μm InP-based quantum dash lasers, in: Proceedings of the SPIE Photonics Europe, 2004, pp. 22–32.
[229] P. Resneau, M. Calligaro, M. Krakowski, H. Liu, M. Hopkinson, A. Somers, et al., High power and very low noise operation at 1.3 and 1.5 μm with quantum dot and quantum dash Fabry–Perot lasers for microwave links, in: Proceedings of the Optics/Photonics in Security and Defence, 2006, pp. 63990K-1–63990K-12.
[230] S. Hein, V. von Hinten, W. Kaiser, S. Höfling, A. Forchel, Electron. Lett. 43 (2007) 1093–1095.
[231] S. Hein, V. von Hinten, S. Höfling, A. Forchel, Appl. Phys. Lett. 92 (2008) 011120.
[232] S. Hein, S. Hofling, A. Forchel, IEEE Photon. Technol. Lett. 21 (2009) 528–530.
[233] C. Dziak, A. Moscho, Y. Li, M. Fanto, V. Kovanis, J. Malowicki, et al., Measurement of the linewidth enhancement factor of a 1550 nm injection-locked quantum dash laser, in: Proceedings of the the 20th Annual Meeting of the IEEE Lasers and Electro-Optics Society (LEOS), 2007, pp. 433–434.
[234] P. Resneau, M. Calligaro, S. Bansropun, O. Parillaud, M. Krakowski, R. Schwertberger, et al., Long term ageing of 1.55 μm InP-based Fabry-Perot quantum dash lasers, in: Proceedings of the Conference on Lasers and Electro-Optics Europe (CLEO), 2005, p. 95.
[235] G. Moreau, S. Azouigui, D.-Y. Cong, K. Merghem, A. Martinez, G. Patriarche, et al., Appl. Phys. Lett. 89 (2006) 241123-1–241123-3.
[236] S. Azouigui, B. Dagens, F. Lelarge, J. Provost, A. Accard, F. Grillot, et al., IEEE Photon. Technol. Lett. 19 (2007) 1181–1183.
[237] S. Azouigui, B. Kelleher, S. Hegarty, G. Huyet, B. Dagens, F. Lelarge, et al., Opt. Express 15 (2007) 14155–14162.
[238] G. Moreau, A. Martinez, K. Merghem, S. Guilet, S. Bouchoule, G. Patriarche, et al., InAs/InP quantum dash based electro optic modulator with over 70 nm bandwidth at 1.55 μM, in: Proceedings of the 19th IEEE International Conference on Indium Phosphide and Related Materials (IPRM), 2007, pp. 271–273.
[239] F.B. le Large, R. Rousseau, B. Martin, F. Poingt, F. le Gouezigou, and O.P.L le Gouezigou, Effect of P-doping on temperature and dynamic performances of 1550 nm InAs/InP quantum dash based lasers, IEEE Indium Phosphide and Related Materials, 2009, pp. 383–386.
[240] B. Dagens, D. Make, F. Lelarge, B. Rousseau, M. Calligaro, M. Carbonnelle, et al., IEEE Photon. Technol. Lett. 20 (2008) 903–905.
[241] F. le Large, N. Chimot, B. Rousseau, F. Martin, R. Brenot, and A. Accard, Chirp optimization of 1550 nm InAs/InP Quantum Dash based directly modulated lasers for 10 Gb/s SMF transmission up to 65 km, in: Proceedings of the International Conference on Indium Phosphide and Related Materials (IPRM), 2010, pp. 1–3.
[242] F. le Large, B. Rousseau, F. Martin, F. Poingt, L. le Gouezigou, O. le Gouezigou, et al., Optimization of tunneling-injection InAs/InP (100) quantum dashes lasers for high-speed optoelectronic devices, in: Proceedings of the 19th IEEE International Conference on Indium Phosphide and Related Materials (IPRM), 2007, pp. 274–277.
[243] D. Zhou, R. Piron, M. Dontabactouny, O. Dehaese, F. Grillot, T. Batte, et al., Electron. Lett. 45 (2009) 50–51.
[244] D. Zhou, R. Piron, M. Dontabactouny, E. Homeyer, O. Dehaese, T. Batte, et al., Phys. Status Solidi (c) 6 (2009) 2217–2221.
[245] F. Lelarge, R. Brenot, B. Rousseau, F. Martin, G. Patriarche, F. Poingt, et al., Recent developments of InP-based quantum dashes for directly modulated lasers and semiconductor optical amplifiers, in: Proceedings of the Integrated Optoelectronic Devices 2008, pp. 68890L-1–68890L-20.
[246] K. Merghem, A. Akrout, A. Martinez, G. Aubin, A. Ramdane, F. Lelarge, et al., Appl. Phys. Lett. 94 (2009).
[247] K. Merghem, R. Rosales, A. Martinez, G. Patriarche, A. Ramdane, N. Chimot, et al., Improvement of modal gain of InAs/InP quantum-dash lasers, in: Proceedings of the 23rd International Conference on Indium Phosphide and Related Materials and Compound Semiconductor Week (CSW/IPRM), 2011, pp. 1–4.
[248] M. Faugeron, F. Lelarge, M. Tran, Y. Robert, E. Vinet, A. Enard, et al., IEEE J. Sel. Top. Quant. Electron. 19 (2013).
[249] P. Resneau, M. Calligaro, B. Rousseau, F. Lelarge, and M. Krakowski, Low threshold, very low noise, high temperature operation of 1.55 μm InP-based Fabry–Perot quantum dashes-in-a-well (DWELL) lasers, in: Proceedings of the European Conference on Lasers and Electro-Optics and the International Quantum Electronics Conference (CLEOE–IQEC), 2007, p. 1.
[250] A. Akrout, A. Shen, R. Brenot, F. van Dijk, O. Legouezigou, F. Pommereau, et al., IEEE Photon. Technol. Lett. 21 (2009) 1746–1748.
[251] R. Rosales, K. Merghem, A. Martinez, A. Akrout, J.-P. Tourrenc, A. Accard, et al., IEEE J. Sel. Top. Quant. Electron. 17 (2011) 1292–1301.
[252] Y.B. M'Sallem, Q.T. Le, L. Bramerie, Q.T. Nguyen, E. Borgne, P. Besnard, et al., IEEE Photon. Technol. Lett. 23 (2011) 453–455.

[253] Q.T. Nguyen, L. Bramerie, G. Girault, O. Vaudel, P. Besnard, J.-C. Simon, et al., 16 × 2.5 Gbit/s downstream transmission in colorless WDM-PON Based on injection-locked Fabry–Perot laser diode using a single quantum dash mode-locked Fabry–Perot laser as multi-wavelength seeding source," in: Proceedings of the Optical Fiber Communication Conference and National Fiber Optic Engineers Conference, San Diego, California, 2009, p. OThA3.
[254] R. Rosales, R. Watts, K. Merghem, C. Calò, A. Martinez, A. Accard, et al., Quantum Dash Mode Locked Lasers as optical comb sources for OFDM superchannels, in: Proceedings of the European Conference and Exhibition on Optical Communication, 2012, p. Mo. 1.–E. 5.
[255] A. Martinez, C. Calò, R. Rosales, R. Watts, K. Merghem, A. Accard, et al., Quantum dot mode locked lasers for coherent frequency comb generation, in: Proceedings of the SPIE OPTO, 2013, pp. 89930A-1–89930A-9.
[256] G. Girault, M. Gay, S. Lobo, L. Bramerie, M. Joindot, J.-C. Simon, et al., Electron. Lett. 44 (2008) 873–875.
[257] M. Costa e Silva, H. Ramanitra, M. Gay, L. Bramerie, S. Lobo, M. Joindot, et al., ECOC (2009) 2009.
[258] M. Costa e Silva, L. Bramerie, M. Gay, S. Lobo, M. Joindot, and J. C. Simon, 4 × 170 Gbit/s DWDM/OTDM transmission using only one quantum dash Fabry Perot mode-locked laser, in: Proceedings of the 36th European Conference and Exhibition on Optical Communication (ECOC), 2010, pp. 1–3.
[259] M. Costa e Silva, A. Lagrost, L. Bramerie, M. Gay, P. Besnard, M. Joindot, et al., Up to 427 GHz all optical frequency down-conversion clock recovery based on quantum-dash Fabry–Perot mode-locked laser, J. Lightwave Technol. 29 (2011) 609–615.
[260] H.S. Djie, C.L. Tan, B.S. Ooi, J. Hwang, X.-M. Fang, Y. Wu, et al., Appl. Phys. Lett. 91 (2007) 111116-1–111116-3.
[261] C. Tan, H.S. Djie, Y. Wang, C.E. Dimas, V. Hongpinyo, Y.H. Ding, et al., IEEE J. Sel. Top. Quant. Electron. 93 (2008) 111101.
[262] C. Tan, H. Djie, Y. Wang, C. Dimas, V. Hongpinyo, Y. Ding, et al., IEEE Photon. Technol. Lett. 21 (2009) 30.
[263] C. Chen, Y. Wang, H.S. Djie, B.S. Ooi, L.F. Lester, T.L. Koch, et al., IEEE J. Sel. Top. Quant. Electron. 17 (2011) 1167–1174.
[264] C.-L. Tan, H.S. Djie, and B. S. Ooi, Novel multiwavelength emitter for WDM transmission utilizing broadband quantum-dash laser diode, in: Proceedings of the Conference on Lasers and Electro-Optics, 2009, p. CTuY6.
[265] W. Kaiser, M. Legge, A. Somers, S. Deubert, J. Reithmaier, and A. Forchel, Single mode CW operating InP based quantum dash distributed feedback lasers at 1.5–1.9 μm, in: Proceedings of the Conference on Lasers and Electro-Optics Europe (CLEO), 20052005, p. 96.
[266] L. Bach, W. Kaiser, R. Schwertberger, J. Reithmaier, A. Forchel, Electron. Lett. 39 (2003) 985–987.
[267] W. Kaiser, K. Mathwig, S. Deubert, J. Reithmaier, A. Forchel, O. Parillaud, et al., Electron. Lett. 41 (2005) 808–810.
[268] K. Mathwig, W. Kaiser, A. Somers, J.P. Reithmaier, A. Forchel, K. Ohira, et al., IEEE Photon. Technol. Lett. 19 (2007) 264.
[269] W. Zeller, M. Legge, A. Somers, W. Kaiser, J. Koeth, A. Forchel, Electron. Lett. 44 (2008) 354–356.
[270] S. Hein, A. Somers, W. Kaiser, S. Höfling, J. Reithmaier, A. Forchel, Electron. Lett. 44 (2008) 527–528.
[271] Q. Zou, K. Merghem, S. Azouigui, A. Martinez, A. Accard, N. Chimot, et al., Appl. Phys. Lett. 97 (2010) 231115.
[272] N. Chimot, S. Joshi, G. Aubin, K. Merghem, S. Barbet, A. Accard, et al., 1550 nm InAs/InP Quantum Dash based directly modulated lasers for next generation passive optical network, in: Proceedings of the International Conference on Indium Phosphide and Related Materials (IPRM), 2012, pp. 177–180.
[273] B. Dagens, D. Make, O. le Gouezigou, J. Provost, F. Lelarge, A. Accard, et al., First Demonstration of 10 Gb/s direct modulation with a buried ridge distributed feedback laser based on quantum dash InAs/InP Material at 1.55 μm, in: Proceedings of the European Conference on Optical Communications (ECOC), 2006, pp. 1–2.
[274] B. Dagens, D. Make, O.L. Gouezigou, F. Lelarge, B. Rousseau, A. Accard, et al., ECOC (2007) 2007.
[275] K. Merghem, S. Azouigui, Q. Zou, A. Martinez, N. Chimot, A. Accard, et al., 1.54 μm InAs/InP p-type doped quantum dash based DFB lasers for isolator free operation, in: Proceedings of the 22nd IEEE International Semiconductor Laser Conference (ISLC), 2010, pp. 178–179.
[276] Y.N. Li, N. Kovanis, and L.V Lester, Modulation response of an injection-locked 1550 nm quantum dash semiconductor laser, 20th Annual meeting of the IEEE Lasers and Electro-Optics Society. LEOS, 2007, pp. 498–499.
[277] N.A. Naderi, M. Pochet, F. Grillot, N.B. Terry, V. Kovanis, L.F. Lester, IEEE J. Sel. Top. Quant. Electron. 15 (2009) 563–571.
[278] L.F. Lester, N.A. Naderi, F. Grillot, R. Raghunathan, V. Kovanis, Opt. Express 22 (2014) 7222–7228.
[279] L. Lester, N. Terry, A. Moscho, M. Fanto, N. Naderi, Y. Li, et al., Giant nonlinear gain coefficient of an InAs/AlGaInAs quantum dot laser, in: Proceedings of the Integrated Optoelectronic Devices, 2008, pp. 68890M-1–68890M-8.

[280] M. Pochet, N. Naderi, N. Terry, V. Kovanis, L. Lester, Opt. Express 17 (2009) 20623–20630.
[281] M.C. Pochet, N.A. Naderi, V. Kovanis, L.F. Lester, IEEE J. Quant. Electron. 47 (2011) 827–833.
[282] M. Pochet, N.A. Naderi, Y. Li, V. Kovanis, L.F. Lester, IEEE Photon Technol. Lett. 22 (2010) 763–765.
[283] S. Azouigui, B. Dagens, F. Lelarge, A. Accard, D. Make, O. Le Gouezigou, et al., Appl. Phys. Lett. 92 (2008) 201106-1–201106-3.
[284] S. Azouigui, B. Dagens, F. Lelarge, J. Provost, D. Make, O. Le Gouezigou, et al., IEEE J. Sel. Top. Quant. Electron. 15 (2009) 764–773.
[285] F. Grillot, N.A. Naderi, M. Pochet, C.-Y. Lin, L.F. Lester, Appl. Phys. Lett. 93 (2008) 191108–191108-3.
[286] F. Grillot, N.A. Naderi, M. Pochet, C.-Y. Lin, P. Besnard, L.F. Lester, IET Optoelectron. 3 (2009) 242–247.
[287] C. Gosset, K. Merghem, A. Martinez, G. Moreau, G. Patriarche, G. Aubin, et al., Appl. Phys. Lett. 88 (2006) 241105–241105-3.
[288] K. Merghem, R. Rosales, S. Azouigui, A. Akrout, A. Martinez, F. Lelarge, et al., Appl. Phys. Lett. 95 (2009) 131111.
[289] M. Dontabactouny, C. Rosenberg, E. Semenova, D. Larsson, K. Yvind, R. Piron, et al., 10 GHz 1.59 μm quantum dash passively mode-locked two-section lasers, in: Proceedings of the SPIE Photonics Europe, 2010, pp. 77201A-1–77201A-10.
[290] R. Rosales, K. Merghem, A. Martinez, A. Accard, F. Lelarge, and A. Ramdane, High repetition rate two-section InAs/InP quantum-dash passively mode locked lasers, in: Proceedings of the IPRM 2011.
[291] R. Rosales, K. Merghem, A. Martinez, A. Accard, F. Lelarge, and A. Ramdane, Two-section InAs/InP quantum-dash passively mode locked lasers, in: Proceedings of CLEO: Science and Innovations, 2011, p. CThG2.
[292] R. Rosales, S. Murdoch, R. Watts, K. Merghem, A. Martinez, F. Lelarge, et al., Opt. Express 20 (2012) 8649–8657.
[293] C.-Y. Lin, Y.-C. Xin, Y. Li, F. Chiragh, L. Lester, Opt. Express 17 (2009) 19739–19748.
[294] A. Shen, C. Gosset, J. Renaudier, G. Duan, J. Oudar, F. Lelarge, et al., Ultra-narrow mode-beating spectral linewidth of a passively mode-locked quantum dot Fabry–Perot laser diode, in: Proceedings of the European Conference on Optical Communications (ECOC), 2006, pp. 1–2.
[295] A. Shen, J.-G. Provost, A. Akrout, B. Rousseau, F. Lelarge, O. Legouezigou, et al., Low confinement factor quantum dash (QD) mode-locked Fabry–Perot (FP) laser diode for tunable pulse generation, in: Proceedings of the Optical Fiber Communication Conference, 2008, p. OThK1.
[296] C. Gosset, K. Merghem, A. Martinez, G. Moreau, G. Patriarche, G. Aubin, et al., Electron. Lett. 42 (2006) 91–92.
[297] A. Akrout, A. Shen, A. Enard, G.-H. Duan, F. Lelarge, A. Ramdane, Electron. Lett. 46 (2010) 73–74.
[298] J. Tourrenc, A. Akrout, K. Merghem, A. Martinez, F. Lelarge, A. Shen, et al., Opt. Express 16 (2008) 17706–17713.
[299] S. Latkowski, R.N. Maldonado-Basilio, P. Landais, Opt. Express 17 (2009) 19166–19172.
[300] R. Maldonado-Basilio, S. Latkowski, and P. Landais, 720 fs pulse generation with 40 GHz passively-mode locked quantum-dash Fabry–Perot laser, in: Proceedings of the 35th European Conference on Optical Communication (ECOC), 2009, pp. 1–2.
[301] R. Maldonado-Basilio, J. Parra-Cetina, S. Latkowski, P. Landais, Opt. Lett. 35 (2010) 1184–1186.
[302] R. Maldonado-Basilio, S. Latkowski, F. Surre, P. Landais, Opt. Commun. 283 (2010) 299–303.
[303] S. Latkowski, R. Maldonado-Basilio, and P. Landais, Short pulse generation with 40 GHz passively-mode locked Q-dashed Fabry–Perot laser, in: Proceedings of the 11th International Conference on Transparent Optical Networks (ICTON), 2009, pp. 1–4.
[304] R. Maldonado-Basilio, S. Latkowski, S. Philippe, P. Landais, Opt. Lett. 36 (2011) 3142–3144.
[305] C. Calò, H. Schmeckebier, K. Merghem, R. Rosales, F. Lelarge, A. Martinez, et al., Opt. Express 22 (2014) 1742–1748.
[306] C. Calo, H. Schmeckebier, K. Merghem, R. Rosales, F. Lelarge, A. Martinez, et al., Frequency-resolved optical gating measurements of sub-ps pulses from InAs/InP quantum dash based mode-locked lasers, in: Proceedings of the International Conference on Indium Phosphide and Related Materials (IPRM), 2013, pp. 1–2.
[307] S. Joshi, C. Calò, N. Chimot, M. Radziunas, R. Arkhipov, S. Barbet, et al., Opt. Express 22 (2014) 11254–11266.
[308] S. Joshi, N. Chimot, S. Barbet, A. Accard, and F. Lelarge, Mode-locked InAs/InP quantum-dash-based DBR laser with monolithically-integrated SOA, in: Proceedings of SPIE OPTO, 2014, pp. 90020C-1–90020C-8.
[309] S. Joshi, N. Chimot, R. Rosales, S. Barbet, A. Accard, A. Ramdane, et al., Mode locked InAs/InP Quantum dash based DBR Laser monolithically integrated with a semiconductor optical amplifier, in: Proceedings of the International Conference on Indium Phosphide and Related Materials (IPRM), 2013, pp. 1–2.
[310] G.-H. Duan, F. Lelarge, B. Dagens, R. Brenot, A. Accard, A. Shen, et al., InAs/InP based quantum dot mode-locked semiconductor lasers at 1.5 μm, Proceedings of the SPIE, Vol. 6782, 2007, pp. 67821V-1–67821V-6 (Article id. 67821V).

[311] R. Rosales, K. Merghem, A. Martinez, F. Lelarge, A. Accard, A. Ramdane, Opt. Express 20 (2012) 9151–9160.
[312] S. Murdoch, R. Watts, Y. Xu, R. Maldonado-Basilio, J. Parra-Cetina, S. Latkowski, et al., Opt. Express 19 (2011) 13628–13635.
[313] E. Martin, R. Watts, L. Bramerie, A. Shen, H. Gariah, F. Blache, et al., Opt. Lett. 37 (2012) 4967–4969.
[314] C. Gosset, K. Merghem, G. Moreau, A. Martinez, G. Aubin, J.L. Oudar, et al., Opt. Lett. 31 (2006) 1848–1850.
[315] A. Akrout, A. Shen, F. Lelarge, F. Pommereau, H. Gariah, F. Blache, et al., Spectrum filtering and pulse compression of Quantum-Dash mode-locked lasers emitting at 1.55 μm, in: Proceedings of the 34th European Conference on Optical Communication (ECOC), 2008, pp. 1–2.
[316] R. Maldonado-Basilio, J. Parra-Cetina, S. Latkowski, N. Calabretta, P. Landais, J. Lightwave Technol. 31 (2013) 860–865.
[317] E. Sooudi, G. Huyet, J.G. McInerney, F. le Large, K. Merghem, R. Rosales, et al., IEEE Photon. Technol. Lett. 23 (2011) 1544–1546.
[318] E. Sooudi, G. Huyet, J.G. McInerney, F. le Large, K. Merghem, A. Martinez, et al., IEEE Photon. Technol. Lett. 23 (2011) 549–551.
[319] E. Sooudi, C. de Dios, J.G. McInerney, H. Huyet, L. Lelarge, K. Merghem, et al., IEEE J. Sel. Top. Quant. Electron. 19 (2013) 1101208.
[320] F. Van Dijk, A. Enard, X. Buet, F. Lelarge, G.-H. Duan, J. Lightwave Technol. 26 (2008) 2789–2794.
[321] J. Renaudier, B. Lavigne, P. Gallion, G.-H. Duan, J. Lightwave Technol. 24 (2006) 3734–3742.
[322] J. Renaudier, B. Lavigne, F. le Large, M. Jourdran, B. Dagens, O. le Gouezigou, et al., IEEE Photon. Technol. Lett. 18 (2006) 1249–1251.
[323] J. Parra-Cetina, S. Latkowski, R. Maldonado-Basilio, P. Landais, IEEE Photon. Technol. Lett. 23 (2011) 531–533.
[324] X. Tang, S.H. Chung, J.C. Cartledge, A. Shen, A. Akrout, G.-H. Duan, Opt. Express 18 (2010) 9378–9383.
[325] X. Tang, J.C. Cartledge, A. Shen, F. van Dijk, A. Akrout, G.-H. Duan, J. Lightwave Technol. 27 (2009) 4603–4609.
[326] J. Luo, J. Parra-Cetina, P. Landais, H.J. Dorren, N. Calabretta, IEEE Photon. Technol. Lett. 25 (2013) 2221–2224.
[327] J. Parra-Cetina, J. Luo, N. Calabretta, S. Latkowski, H.J. Dorren, P. Landais, J. Lightwave Technol. 31 (2013) 3127–3134.
[328] R. Maldonado-Basilio, S. Latkowski, S. Philippe, P. Landais, Opt. Lett. 36 (2011) 1569–1571.
[329] V. Roncin, A. O'Hare, S. Lobo, E. Jacquette, L. Bramerie, P. Rochard, et al., IEEE Photon. Technol. Lett. 19 (2007) 1409–1411.
[330] M. Yañez, J.C. Cartledge, J. Lightwave Technol. 29 (2011) 1437–1444.
[331] J. Luo, J. Parra-Cetina, S. Latkowski, R. Maldonado-Basilio, P. Landais, H. Dorren, et al., Quantum Dash Mode-Locked Laser based Open-Loop optical clock recovery for 160 Gb/s transmission system, in: Proceedings of the Optical Fiber Communication Conference/National Fiber Optic Engineers Conference, Anaheim, California, 2013, p. OTh4D.6.
[332] N. Calabretta, J. Luo, J. Parra-Cetina, S. Latkowski, R. Maldonado-Basilio, P. Landais, et al., 320 Gb/s all-optical clock recovery and time demultiplexing enabled by a single Quantum Dash Mode-Locked Laser Fabry–Perot optical clock pulse generator, in: Proceedings of the Optical Fiber Communication Conference/National Fiber Optic Engineers Conference, Anaheim, California, 2013, p. OTh4D.5.
[333] J. Luo, N. Calabretta, J. Parra-Cetina, S. Latkowski, R. Maldonado-Basilio, P. Landais, et al., Opt. Lett. 38 (2013) 4805–4808.
[334] A. Stöhr, A. Akrout, R. Buß, B. Charbonnier, F. van Dijk, A. Enard, et al., J. Opt. Netw. 8 (2009) 471–487.
[335] A. Stohr, S. Babiel, P.J. Cannard, B. Charbonnier, F. van Dijk, S. Fedderwitz, et al., IEEE Trans. Microw. Theory Tech. 58 (2010) 3071–3082.
[336] F. Lecoche, E. Tanguy, B. Charbonnier, H. Li, F. Van Dijk, A. Enard, et al., J. Lightwave Technol. 27 (2009) 5469–5474.
[337] F. van Dijk, B. Charbonnier, S. Constant, A. Enard, S. Fedderwitz, S. Formont, et al., Quantum dash mode-locked lasers for millimeter wave signal generation and transmission, in: Proceedings of the 23rd Annual Meeting of the IEEE Photonics Society, 2010, pp. 187–188.
[338] R. Rosales, B. Charbonnier, K. Merghem, F. van Dijk, F. Lelarge, A. Martinez, et al., InAs/InP quantum dash based mode locked lasers for 60 GHz radio over fiber applications, in: Proceedings of the International Conference on Indium Phosphide and Related Materials (IPRM), 2012, pp. 185–187.
[339] F. Van Dijk, M. Faugeron, F. le large, M. Tran, M. Chtioui, Y. Robert, et al., Asymmetrical cladding quantum dash mode-locked laser for terahertz wide frequency comb, in: Proceedings of the International Topical Meeting on Microwave Photonics (MWP), 2012, pp. 282–285.

[340] R. Watts, R. Rosales, S. Murdoch, F. Lelarge, A. Ramdane, and L. Barry, QDash semiconductor mode-locked lasers as compact subchannel comb for optical OFDM superchannel systems, in: Proceedings of CLEO: Science and Innovations, 2012, p. CM1I–5.
[341] E. Sooudi, S. Sygletos, A.D. Ellis, G. Huyet, J.G. McInerney, F. le large, et al., IEEE J. Quant. Electron. 48 (2012) 1327–1338.
[342] K. Merghem, C. Calo, R. Rosales, X. Lafosse, G. Aubin, A. Martinez, et al., IEEE J. Quant. Electron. 50 (2014) 275–280.
[343] A. Bilenca, R. Alizon, V. Mikhelashvili, G. Eisenstein, R. Schwertberger, D. Gold, et al., Electron. Lett. 38 (2002) 1350–1351.
[344] D. Hadass, A. Bilenca, R. Alizon, H. Dery, V. Mikhelashvili, G. Eisenstein, et al., IEEE J. Sel. Top. Quant. Electron. 11 (2005) 1015–1026.
[345] F. Pommereau, R. Brenot, B. Rousseau, F. Martin, F. Poingt, L. LeGouezigou, et al., Optimization of 1550 nm InAs/InP quantum dash and quantum dot based semiconductor optical amplifier, in: Proceedings of the IEEE International Conference on Indium Phosphide and Related Materials (IPRM), 2009, pp. 339–342.
[346] M. Van der Poel, J. Mørk, A. Somers, A. Forchel, J. Reithmaier, G. Eisenstein, Appl. Phys. Lett. 89 (2006) 081102.
[347] P. Lunnemann, S. Ek, K. Yvind, R. Piron, J. Mørk, New J. Phys. 14 (2012) 013042.
[348] M. van der Poel, T.W. Berg, J. Mørk, D. Birkedal, V. Mikhelashvili, G. Eisenstein, et al., Measurements of gain and index dynamics in quantum dash semiconductor optical amplifiers, in: Proceedings of the Optical Amplifiers and Their Applications/Integrated Photonics Research, San Francisco, California, 2004, p. OTuD4.
[349] A. Capua, G. Eisenstein, J. Reithmaier, Appl. Phys. Lett. 97 (2010) 131108.
[350] A. Capua, G. Eisenstein, J. Reithmaier, Appl. Phys. Lett. 98 (2011) 101108.
[351] A. Capua, A. Saal, O. Karni, G. Eisenstein, J.P. Reithmaier, K. Yvind, Opt. Express 20 (2012) 347–353.
[352] A. Capua, V. Mikhelashvili, G. Eisenstein, J. Reithmaier, A. Somers, A. Forchel, et al., Opt. Express 16 (2008) 2141–2146.
[353] D. Hadass, V. Mikhelashvili, G. Eisenstein, A. Somers, S. Deubert, W. Kaiser, et al., Appl. Phys. Lett. 87 (2005) 021104-1–021104-3.
[354] R. Brenot, M. Manzanedo, J.-G. Provost, O. Legouezigou, F. Pommereau, F. Poingt, et al., ECOC (2007) 2007.
[355] A. Bilenca, R. Alizon, V. Mikhelashhvili, D. Dahan, G. Eisenstein, R. Schwertberger, et al., IEEE Photon. Technol. Lett. 15 (2003) 563–565.
[356] R. Alizon, A. Bilenca, H. Dery, V. Mikhelashvili, G. Eisenstein, R. Schwertberger, et al., Appl. Phys. Lett. 82 (2003) 4660–4662.
[357] R. Alizon, D. Hadass, V. Mikhelashvili, G. Eisenstein, R. Schwertberger, A. Somers, et al., Electron. Lett. 40 (2004) 760–761.
[358] G. Eisenstein, Do quantum dots or quantum wire based devices offer a practical advantage in producing semiconductor optical amplifiers over conventional 2-D active media, in: Proceedings of the Conference on Optical Fiber Communication and the National Fiber Optic Engineers Conference (OFC/NFOEC), 2007 pp. 1–2.
[359] R. Alizon, D. Hadass, V. Mikhelashvili, G. Eisenstein, R. Schwertberger, A. Somers, et al., Electron. Lett. 41 (2005) 266–268.
[360] A. Capua, S. O'duill, V. Mikhelashvili, G. Eisenstein, J. Reithmaier, A. Somers, et al., Opt. Express 16 (2008) 19072–19077.
[361] A. Martinez, G. Aubin, F. Lelarge, R. Brenot, J. Landreau, A. Ramdane, Appl. Phys. Lett. 93 (2008) 091116-1–091116-3.
[362] M.Z.M. Khan, T.K. Ng, B.S. Ooi, IEEE Photon. J. 6 (2014) 1600108.
[363] C.E. Dimas, C.-L. Tan, H.S. Djie, A.D. McAulay, B.-S. Ooi, IEEE Photon. Technol. Lett. 21 (2009) 694–696.
[364] D.A. Miller, Proc. IEEE 97 (2009) 1166–1185.
[365] E. Timurdogan, C.M. Sorace-Agaskar, J. Sun, E. Shah Hosseini, A. Biberman, M.R. Watts, Nat. Commun. 5 (2014) 4008-1–4008-11.